

INFORMATION TO USERS

This manuscript has been reproduced from the microfilm master. UMI films the text directly from the original or copy submitted. Thus, some thesis and dissertation copies are in typewriter face, while others may be from any type of computer printer.

The quality of this reproduction is dependent upon the quality of the copy submitted. Broken or indistinct print, colored or poor quality illustrations and photographs, print bleedthrough, substandard margins, and improper alignment can adversely affect reproduction.

In the unlikely event that the author did not send UMI a complete manuscript and there are missing pages, these will be noted. Also, if unauthorized copyright material had to be removed, a note will indicate the deletion.

Oversize materials (e.g., maps, drawings, charts) are reproduced by sectioning the original, beginning at the upper left-hand corner and continuing from left to right in equal sections with small overlaps. Each original is also photographed in one exposure and is included in reduced form at the back of the book.

Photographs included in the original manuscript have been reproduced xerographically in this copy. Higher quality 6" x 9" black and white photographic prints are available for any photographs or illustrations appearing in this copy for an additional charge. Contact UMI directly to order.

UMI

A Bell & Howell Information Company
300 North Zeeb Road, Ann Arbor MI 48106-1346 USA
313/761-4700 800/521-0600

FLEXIBLE STRUCTURE ESTIMATION AND CONTROL USING THE GLOBAL POSITIONING SYSTEM

A DISSERTATION

SUBMITTED TO THE DEPARTMENT OF AERONAUTICS AND ASTRONAUTICS

AND THE COMMITTEE ON GRADUATE STUDIES

OF STANFORD UNIVERSITY

IN PARTIAL FULFILLMENT OF THE REQUIREMENTS

FOR THE DEGREE OF

DOCTOR OF PHILOSOPHY

By

Edward Harrison Teague

May 1997

UMI Number: 9802127

**Copyright 1997 by
Teague, Edward Harrison**

All rights reserved.

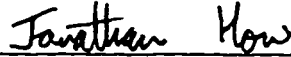
**UMI Microform 9802127
Copyright 1997, by UMI Company. All rights reserved.**

**This microform edition is protected against unauthorized
copying under Title 17, United States Code.**

UMI
300 North Zeeb Road
Ann Arbor, MI 48103

© Copyright 1997
by
Edward Harrison Teague

I certify that I have read this thesis and that in my opinion it is fully adequate, in scope and in quality, as a dissertation for the degree of Doctor of Philosophy.



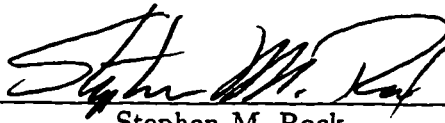
Jonathan P. How
(Principal Adviser)

I certify that I have read this thesis and that in my opinion it is fully adequate, in scope and in quality, as a dissertation for the degree of Doctor of Philosophy.



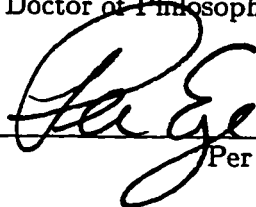
Bradford W. Parkinson

I certify that I have read this thesis and that in my opinion it is fully adequate, in scope and in quality, as a dissertation for the degree of Doctor of Philosophy.



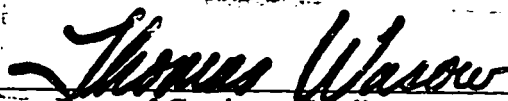
Stephen M. Rock

I certify that I have read this thesis and that in my opinion it is fully adequate, in scope and in quality, as a dissertation for the degree of Doctor of Philosophy.



Per Enge

Approved for the University Committee on Graduate Studies:



Dean of Graduate Studies

Abstract

This dissertation describes the development of a new sensing system for real-time measurement and control of flexible structure motions using the Global Positioning System (GPS). The sensor uses measurements of the carrier phase of the GPS signal at several antennas to estimate the deformation and orientation of a structure on which the antennas are mounted. Its distributed nature, plus its superior DC performance, make the GPS based sensor a powerful source of information for large structure vibration control. Also, the GPS sensor is unique in that it provides information for vibration estimation *and* bias-less structure orientation estimation simultaneously.

Realization of this GPS sensor has brought to light some new challenges. Previous work has demonstrated the applicability of GPS carrier sensing for vehicle attitude determination, and a principle challenge of this work has been resolution of the *cycle ambiguities*¹ inherent in the phase measurements. The most successful techniques have used attitude motion of the vehicle (the *structure*) over time, plus the assumption that the structure is nearly rigid, to provide observability of the unknown cycle parameters. But, as this thesis will show, the previous techniques do not work for structures with significant structural flexibility, and a central focus of this research has been to develop algorithms that can take flexibility into account. A new solution to the cycle ambiguity problem is presented that combines measurements taken during structural motion with a model of the platform dynamics to initialize the unknown cycle ambiguities.

¹Because carrier waves are identical cycle to cycle, the number of full cycles in the measurement is ambiguous at the time of initial signal lock.

Real-time signal processing algorithms were developed, implemented, and tested on an experimental large flexible structure in the laboratory that was designed to exhibit flexible motions detectable by current GPS receivers (approximately 1 cm sensitivity in a 0–10 Hz bandwidth). The 8 meter long, 180 kg test structure is suspended from above and emulates the motions of a large, flexible, orbiting platform, moving with low frequencies and large structural deflections. This test structure is outfitted with an array of GPS antennas for motion sensing, and an array of compressed air thrusters for control actuation. The GPS sensor provides better than 0.5° rotational accuracy, determined by comparing with on-board gyroscopes. Several automatic control experiments were performed by closing feedback loops from the GPS measurements to the thruster commands. Automatic vibration damping tests showed the ability to reduce free structure vibrations to sub-centimeter/sub-degrees levels (as measured by GPS) with approximately 5 second settling times. Also, tests of the closed loop system response to impulsive disturbances showed rejection of such disturbances with negligible overshoot. Finally, a 35° rigid-body slew maneuver was performed showing simultaneous rigid-body orientation and elastic vibration control. Vibration motion was maintained within sub-centimeter/sub-degree levels throughout the 30 second slew.

This work represents an exciting advancement in the field of GPS sensing. It is significant because it shows the potential for GPS as a high precision large-array real-time sensor. It also marks the first demonstration of real-time flexible platform vibration control using GPS as the only source of motion information.

Acknowledgments

This thesis has greatly benefited from the efforts and support of many people and organizations whom I would like to thank. First, I would like to thank my advisor Jonathan How for his enormous contribution to the success of this work. Professor How's insights during our many discussions about the project were invaluable, and I appreciate his attention to detail and clarity in our writings. I would also like to acknowledge the help and support of my advisor Bradford Parkinson. Professor Parkinson helped launch this research project, and he arranged the funding from beginning to end. Also, his achievements as a scientist and as a manager have been a great inspiration to me. I would also like to gratefully acknowledge the rest of my defense and reading committee members, Stephen Rock, David Powell, Stephen Boyd, Per Enge, and Jean Heegaard.

Many of my fellow students have contributed both help and camaraderie during this work. In particular, I would like to thank Kurt Zimmerman, Stewart Cobb, Konstantin Gromov and Clark Cohen for their direct contributions to the hardware and software systems used. Thanks also to Goutam Chatterjee, Michael Boerjes, and London Lawson for their contributions while interning on the project. I also thank the many other colleagues and friends in the GPS laboratory for their comments and suggestions.

This work was funded by NASA through a spin-off contract from the Gravity Probe-B satellite project at Stanford for research on novel GPS applications. I am grateful for NASA's support. I would also like to acknowledge Trimble Navigation, Ltd. for providing GPS hardware for this research, and for some interesting part-time employment during my graduate career.

Finally, I owe an immeasurable amount of gratitude to my parents James and Betty for their love and support over the years. The environment that they created during my early years was ideal for my academic and personal growth, and their support during my long education has been magnanimous. With much love and anticipation for many more years of good times and friendship, I dedicate this dissertation to them.

To my parents,
James L. Teague and Betty H. Teague

Table of Contents

Abstract	iv
Acknowledgments	vi
Table of Contents	xii
List of Tables	xiii
List of Figures	xvi
1 Introduction	1
1.1 Background	2
1.1.1 A First Introduction to the GPS Signal	2
1.1.2 GPS Carrier Sensing History	5
1.2 Flexible Structure Project Overview	9
1.3 Contributions	11
2 The GPS Carrier Phase Measurement	13
2.1 Differential Carrier Phase (DCP) Measurement	13
2.1.1 DCP Equations	14
2.1.2 Linearized DCP Equation	18
2.1.3 Error Sources	20
2.2 Comparison with Traditional Sensors	25

3	Bias Ambiguity Resolution	27
3.1	Characteristics of β	27
3.2	Solution Methods	28
3.2.1	Integer Search	28
3.2.2	Gradient Search	29
3.3	Kinematic Bias Estimation	31
3.3.1	A Batch Algorithm	32
3.3.2	Requirements for Observability	33
3.3.3	A Simple Physical Example	35
3.3.4	Effect of Platform Flexibility	39
3.4	Dynamic Bias Estimation	42
3.4.1	A Second Batch Algorithm	42
3.4.2	The Simple Example, Revisited	44
3.4.3	Observability and Model Accuracy	47
3.5	Summary	48
4	The Experimental Hardware	51
4.1	The Physical Structure	51
4.2	The Sensors	56
4.2.1	GPS sensors	56
4.2.2	Rate Gyroscopes	58
4.3	The Actuators	59
4.4	Preliminary Sensor Data Analysis	62
4.5	Summary	64
5	Software Systems Architecture	67
5.1	Real-Time Processing Design	67
5.2	Analysis of Task Execution Timing	69
5.3	Summary	71

6	Physical System Modeling	73
6.1	Generalized Coordinates	74
6.2	Dynamic Modeling	77
6.2.1	Equations of Motion	77
6.2.2	Definition of the State Vector	78
6.2.3	Finding the Modal Transformation	79
6.2.4	Force Modeling	83
6.2.5	Process Noise Modeling	86
6.3	Measurement Kinematics	86
6.3.1	The Measurement Equation	87
6.3.2	Measurement Linearization	89
6.4	Summary	91
7	Real-Time State Estimation	93
7.1	Recursive Estimator Equations	93
7.2	Some Practical Issues	95
7.2.1	Matrix Computations in C	95
7.2.2	Efficient Measurement Equation Computation	96
7.3	Example of Real-Time Estimator Operation	96
7.3.1	Bias Initialization	97
7.3.2	Recursive Operation	99
7.3.3	Linearization About the Rigid-Body Configuration	102
7.4	Summary	104
8	Experiments in Real-Time Control	105
8.1	Controller Design	105
8.2	Thruster Pulse Modulation	109
8.3	Vibration Suppression	113
8.4	Disturbance Rejection	114
8.5	Slew Maneuver Control	119

8.6	Summary	121
9	Conclusions	123
9.1	Summary of Results and Contributions	124
9.1.1	Generalized Flexibility Sensing	124
9.1.2	Bias (Cycle) Ambiguity Resolution with Flexibility	124
9.1.3	Algorithms for Real-Time State Estimation	124
9.1.4	Real-Time Control Demonstration	125
9.1.5	Space Platform Ground Test	125
9.2	Suggestions for Further Work	126
9.3	General Distributed Antenna GPS Carrier Sensing	127
9.4	Closing	128

APPENDICES

A	General Carrier Phase Analysis	131
B	Kinematic Estimator Observability Proof	137
C	CAD Drawings	139
D	MSC/NASTRAN Input File	149
E	Transmitter Phase Center Position Survey	153
	Bibliography	157

List of Tables

2.1	Number of Measurements	14
2.2	Error Table for Laboratory DCP Measurements	25
3.1	Building a Determined Set	29
4.1	Experimental System Characteristics	65
6.1	Definitions of Key Parameters	74
6.2	Modal Characteristics	82
6.3	Damping Time Constants	83
7.1	Estimator Test Experiment Procedure	102
8.1	Thruster Modulation Summary	112

List of Figures

1.1	The Space Station	2
1.2	GPS Carrier Measurement	5
1.3	The Experimental Structure in Motion	10
1.4	Elements in the Control System	11
2.1	Master/Slave Antenna Configuration	14
2.2	DCP Measurement	15
2.3	Planar Wavefront Geometry	19
2.4	DCP Error from Transmitter Position Error	22
2.5	DCP Error from Relative Antenna Attitude	24
2.6	DCP Error from Relative Antenna Attitude	24
3.1	A Simple Example	36
3.2	Linear Constraint	36
3.3	Nonlinear Constraint	39
3.4	Rigid Baseline Constraint	40
3.5	Flexible Baselines	40
3.6	Simple System Diagram	45
3.7	Free Antenna Motion	45
3.8	Examples of Kinematic vs. Dynamic Solutions	46
3.9	Converged Bias Error	47
4.1	A Diagram of the Structure	53
4.2	Photo of Balance Mechanism	53

4.3	Suspension System	54
4.4	Overhead Picture of Assembly	55
4.5	Coordinate System for Physical Properties	55
4.6	Transmit and Receiver Hardware	57
4.7	Antenna Receiver Connection Diagram	58
4.8	Mounted Rate Gyroscopes	59
4.9	Actuation System Diagram	60
4.10	Thruster Cluster	60
4.11	Thruster Configuration	62
4.12	Free Motion Sensor Spectra	63
5.1	Real-Time Processing Setup	69
5.2	Timescan® Screen Shot	71
6.1	Generalized Coordinates	75
6.2	Finite Element Structural Grid	80
6.3	Modes	81
6.4	Thruster Vector Geometry Grid	85
6.5	Deformed Structure and Point Definitions	87
7.1	Diagram of Real-Time Processing	94
7.2	Bias Estimator Convergence	98
7.3	Residuals and RB State After Convergence	98
7.4	Motion Studied for Estimator Evaluation	99
7.5	Static Estimator Comparison	101
7.6	Comparison of GPS and Gyro Based Estimates	103
7.7	GPS and Gyro Estimate Difference	103
8.1	Pole Locations	107
8.2	Pole Locations (zoomed)	107
8.3	Controller Simulations	109
8.4	A Thruster Cycle	111
8.5	PWPF Lookup Table	111

8.6	Motion Studied for Vibration Control Evaluation	113
8.7	Elastic Vibration Control	115
8.8	Pulse Thrusters	116
8.9	Pulse Response	116
8.10	Random Noise Thrusters	118
8.11	Output Spectra	118
8.12	Motion Studied for Slew Control Evaluation	120
8.13	Slew Maneuver Control	120
A.1	General Phase Reception Diagram	132
E.1	Simple System Diagram	154

CHAPTER 1

Introduction

This dissertation presents the development of a new, interesting, and useful application of GPS sensing. GPS is shown to be a key source of information for measuring, and controlling, the motion and orientation of large flexible structures. A prototype structure that could use this technology is the Space Station, shown in Fig. 1.1. Such a structure is large and lightweight by necessity, and thus is very flexible, resulting in slow vibrations with significant deflections if excited. Also, due to the vacuum environment in space and the low internal damping in the structure, such vibrations may persist for a long time. These structural vibrations could be counter-productive for humans and experiments onboard, and, over time, could cause weakening of the platform. Thus, the Space Station is an ideal candidate for vibration control, but it needs a very accurate sensor of low frequency motions.

This thesis discusses mounting an array of GPS antennas on a flexible structure and using measurements of the GPS signals at the antennas to measure vibrations. Additionally, the GPS system can be used to simultaneously measure the orientation of the platform in space, an important ability that is not possible (or not as easy) with other sensors.

To verify this new GPS sensing technology, a model of a large flexible structure was built and suspended in our laboratory that emulates the vibration of a typical orbiting platform. Experiments were performed that test simultaneous vibration and orientation automatic control using GPS as the only source of motion information. Before launching into the theory and experimentation in this thesis, it is useful to explore some basics of GPS sensing and some history of its use. For a broader overview, see [Parkinson *et al.*, 1996].



Figure 1.1: The Space Station

The Space Station is a structural system that could use a GPS based deformation and orientation sensor for vibration and attitude control.

1.1 Background

1.1.1 A First Introduction to the GPS Signal

This section is for those readers that might not already understand communications theory (say my parents decide to read this; it is, in fact, dedicated to them). Sometimes it is useful to make analogies that relate concepts which are not everyday experiences to familiar, everyday ideas (if possible). To this end, this section was written intentionally with a more “familiar” tone than the rest of the dissertation. Footnotes here are used to provide some

technical completeness but are not required for understanding.

At present, a signal is being broadcast from each of the 24 GPS satellites that are in orbit about the earth. This means that if you go outside, and put your hand out, your hand is being radiated by signals from whichever satellites are overhead, much like your hand is being radiated by the sun, but at much lower power.¹ The GPS signal was designed by the architects of the system to provide useful information to people. Now, we just need to *see* it. The job of *seeing* or tracking a signal from a GPS satellite can be compared to the job of reading this dissertation from, say, 100 meters. You would not be able to read it with the unaided eye — in fact, you would not even be able to tell that it were there.²

But say you *do* know that it's there, and you know about where it is located. If you set up a telescope that has a capability for sufficient magnification, point it in the right area, find this dissertation, zoom in, and focus, then you can read the information. The job of a GPS receiver is analogous to the telescope in this example. Let's say you go outside, and instead of putting out your hand, you put out a GPS antenna, and connect it to a receiver. The antenna detects a myriad of signals and noise, and the receiver's job is to focus in where it thinks the signals from GPS satellites might be and to find them. It's a bit different, though, in that the search for GPS signals is not a search in physical space but a search in frequency and phase space. But, the idea is the same.

Once a receiver tracks a GPS signal, the primary information that is available is *range*. The signal is a sort of ruler with which you can measure the distance from the receiver to the transmitter (satellite). There are two main components of this signal, the code and the carrier.³ The code is a long digital sequence of 1's and -1's that is generated at 1 MHz by a known mathematical formula that is unique to each satellite. The carrier is a sine wave at 1.5 GHz and was originally intended to help the code signal travel through space. Traditional GPS techniques rely on recognizing the phase of the known code signal at the antenna to determine the range from transmitter to antenna. By simultaneously tracking signals from four or more satellites, a user is able to estimate his or her position to around 20

¹Your hand is also being radiated by radio signals from nearby stations, etc.

²Presumably, if you could read it, there would be some valuable information there for you.

³For simplicity, we will only consider C/A code and L1 carrier here.

meters accuracy in three dimensions, depending on the sophistication of the receiver.⁴ The ranging accuracy for an individual signal for this case usually works out to approximately 1–10 meters. This *position from ranges* computation is sometimes called triangulation.

It turns out that the carrier is more useful than just as a source of transmission power. The 1.5 GHz wave works out to have a wavelength of about 20 centimeters, and a receiver can track its phase to a fraction of that length — about 5 millimeters. In contrast, the code wavelength (or chip length in a digital signal) is about 300 meters. Unlike the code, though, the carrier waves are not unique, so it is not obvious how many waves are between the transmitter and the receiver, making absolute range unknown. This unknown is called the *carrier cycle ambiguity*. If the cycle ambiguity problem can be solved, we have range information of much greater precision (< 1 cm or about 100–1000 times better) than available from code tracking. As you may know or may have guessed, techniques of solving this ambiguity have been found under certain circumstances.

The following is a thought experiment that, although not exactly technically accurate, is very valuable for understanding the basics of carrier tracking.⁵ Imagine that a wave arrives at an antenna from some source and direction. When the receiver *locks on* or tracks the carrier wave, the wave can be thought of as freezing in space from the point of view of the receiver. Now, as the antenna subsequently moves closer to or further from the signal source, the phase that it measures equals the phase of the standing wave at that position in space.⁶ Figure 1.2 illustrates a phase measurement at an antenna as a reading from a 360° gauge. You can imagine that as the antenna moves to the left, the indicator on its gauge rotates in a clockwise direction, for example.

With this in mind, imagine going back outside with an antenna in hand, that is connected to a receiver. The signals arriving from different directions in the sky can be detected and tracked after a bit of searching by the receiver, creating a three dimensional *field* of carrier waves that contains a wealth of information about the position (and motion) of the antenna.

⁴While three range measurements are enough to determine the three position coordinates, a fourth range is needed to sufficiently refine the accuracy of the receiver time reference for a solution.

⁵Receiver timing errors are neglected here, and throughout the rest of this section.

⁶The receiver measures greater than one cycle of motion by keeping a running count of complete cycle wraparounds. The remaining unknown is the exact wave at the antenna when lock is achieved.

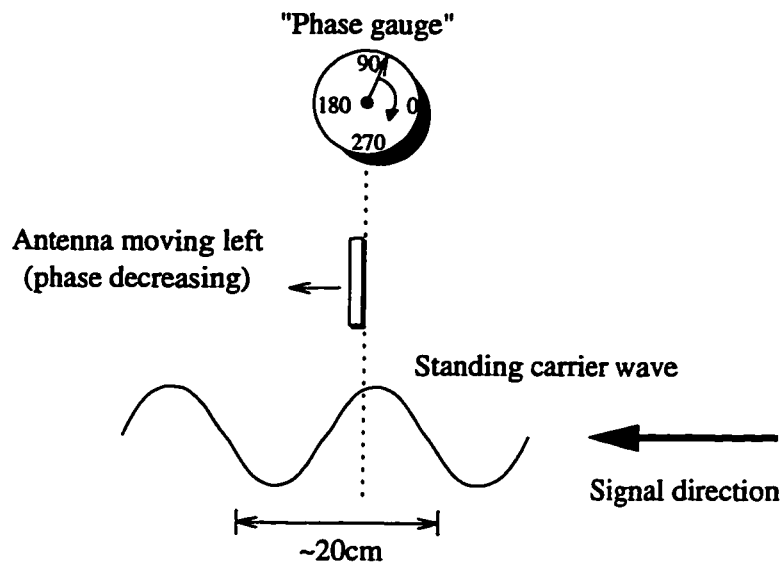


Figure 1.2: GPS Carrier Measurement

This figure shows a simplification of the carrier phase measurement. The GPS receiver can measure the phase of a carrier wave at an antenna to a small fraction of its 20 centimeter wavelength.

An important advantage of GPS is that this signal environment and its information are available anywhere the signal can be tracked, which is almost everywhere on the surface of the Earth, in the sky, and in the lower orbits about the Earth.⁷

Actually, this is not the whole story. Ranging and timing errors must be removed before the centimeter position information is attainable. Also, the cycle ambiguity must be resolved. But this overview is a good starting point, and it illustrates some of the potential of GPS carrier ranging. The next section presents some of the pioneering research that made centimeter GPS carrier ranging a reality.

1.1.2 GPS Carrier Sensing History

This section chronicles the early research on GPS carrier sensing and discusses some of the challenges and achievements of the past 20 years, from static antenna survey to dynamic flexible body attitude and deformation sensing. An emphasis is placed on the details that

⁷ A receiver generally needs a line of sight from satellite to antenna that is unobstructed by solid objects, since the signal does not penetrate most solid materials.

are most relevant to the flexible structure research of this dissertation.

The Global Positioning System exists today because of the efforts of many talented scientists and project leaders in the mid-1970's, sponsored by the U.S. Department of Defense and a collaboration between the U.S. military services. The first Joint Program Office (JPO) was formed in 1973 and led by Dr. (Col.) Bradford W. Parkinson. Impressively, the JPO progressed from inception to first satellite launch in less than four years. A summary of the early history of the JPO and the design of GPS can be found in [Parkinson and Gilbert, 1983].

While the primary ranging signal of GPS was designed to be the digital code signals, investigation of the carrier wave for ranging information took place from the very beginning of GPS research. Much of the initial work was done by the researchers in the field of geodetic survey who required much more accuracy than available from code phase measurements and who could leave antennas static for long periods of time for filtering. These scientists were familiar with continuous wave processing from their work on land based systems RADAR, Loran, OMEGA, and DME systems, as well as the newer satellite radionavigation system, TRANSIT. The back to back articles in *Bulletin Géodésique* in 1979 [Anderle, 1979; Counselman III and Shapiro, 1979; MacDoran, 1979] plus [Bossler *et al.*, 1980] outline the use and benefits of the carrier observable and present some of the difficulties, such as *timing and ambiguity*. More activity in the early eighties led to the *Positioning with GPS-85* [Goad, 1985] conference (sponsored by public and private organizations in the US and abroad) in which many papers (particularly sessions 5, 6 and 7 on Modeling and Processing) further defined the important theoretical and practical aspects of GPS carrier phase processing.

Other notable contributions during this time include the 1982 paper by Hatch [Hatch, 1982], who showed that the high-precision carrier signal could be combined with the non-ambiguous code signal for improved accuracy. The *carrier smoothed code* approach has been used successfully for many years. However, the raw ranging from antenna to satellite has fundamental limits in accuracy due to satellite clock and ephemeris error and to atmospheric signal delay. These sources of error typically add errors on the decimeter and meter level, and drown the receiver's ability to track a carrier at sub-centimeter precision.

The ultimate level of precision using carrier measurement was seen to be possible by processing simultaneous measurements from antennas tracking the same satellite to compute the relative position of antennas (see [Goad and Remondi, 1979] for example). Common mode errors can be eliminated in this way, which reduces errors to centimeters for relative position surveying and for other interferometric applications. For example, the use of carrier phase measurements for attitude and heading measurement aboard ships is suggested in [MacDoran *et al.*, 1984].

The generalization of these ideas to distributed arrays of antennas for non-static, high precision relative ranging was seen to have a wide potential, most immediately for attitude determination of essentially rigid vehicles. Two main technical difficulties needed to be addressed for the realization of this potential: timing and ambiguity. Clock differential between measurements at two antennas can be the dominating effect in single differenced phase measurements (for typical quartz clocks in user equipment). Two primary techniques are used to eliminate clock error: double differencing and common clock. Double differencing subtracts the differential phase from two satellites in common view of an antenna pair, eliminating the clock error. This was introduced in [Greenspan *et al.*, 1982]. See [Van Graas and Braasch, 1991] for a discussion of double differencing for attitude determination with experimental results. Another solution is to provide a common clock reference if the antennas are in close proximity (several meters). Common clock differential carrier phase for attitude experimental results are shown in [Kruczynski *et al.*, 1989], and results using antenna multiplexing are shown in [Cohen and Parkinson, 1992] (reduces the number of required receiver channels).

Use of relative phase measurements also requires accurate determination of the carrier cycle ambiguity. The ambiguity is also referred to as the *integer ambiguity* because the variables are expressed as an integer number of waves. First solution approaches worked by searching the entire space of possible cycles (integers) and using redundant measurements to produce a measurement residual [Hwang, 1991]. The integer set that results in the lowest residual should be the correct set, but this is not guaranteed. This search approach can work well if the search space of possible integers is small (due to a known constraint in antenna

separation). Unfortunately, in the presence of noise, the solution is not unique, and can be prone to erroneous solutions (see [Cohen, 1996] section IV for a graphical visualization of this phenomenon).

It is also important to note that any differences in the hardware between antennas (most notable being antenna cable length) contribute a significant offset in the differential carrier phase (DCP) measurement (referred to as *line bias*). This adds into the measurement in the same way as the integer ambiguity. Often, the line bias can be calibrated, but any errors in the calibration will result in a non-integer character of the subsequent ambiguities, endangering search techniques further.

Another method of determining the ambiguity is to ignore the possible integer character of the variables at first and to do a standard gradient search for the optimal solution, treating the ambiguities as continuous biases. While computation of this gradient and convergence of the algorithm require some special circumstances (for details, see Chapter 3), the technique has proven to be fast, highly reliable, and accurate for a wide scope of applications. A few examples are given in [Cohen and Parkinson, 1992; Cohen *et al.*, 1995; Conway, 1995; Lawrence, 1996]. This work was pioneered by Cohen for the development of a small, inexpensive, solid-state attitude sensor that used only GPS L1 carrier measurements [Cohen, 1992]. This sensor has been the basis for recent studies of GPS attitude determination on aircraft [Cohen and Parkinson, 1992; Cohen *et al.*, 1994b] and spacecraft [Cohen *et al.*, 1994a; Bauer, 1996]. The attitude ambiguity algorithms use large scale rotational motion of the platform to provide the necessary integer observability and are thus called *motion-based* methods.

An important aspect of the attitude determination research on aircraft is the effect of airframe flexibility on the attitude solution. For rigid bodies, attitude accuracy is directly improved by large antenna separations, but large separations increase the motion of the antennas due to structural flexibility. Thus, wing tip mounted antennas can greatly enhance angular sensor accuracy but can cause problems if flexibility is not taken into account (see [Van Graas and Braasch, 1991] for discussion). For this reason, in [Cohen and Parkinson, 1992], aircraft wing flex is included as a single additional state in the attitude

solution. But, for reasons explained in this dissertation, platform elastic motion that maps linearly into the GPS measurements is not simultaneously observable with integer ambiguities using kinematic gradient search techniques. Thus, until now, platform flex states have been assumed *constant* for the integer initialization process. As shown in the simple example in Chapter 3, this approach is a potential problem if the flexibility is not well approximated as a constant during the collection of initialization measurements.

Fortunately, it is possible to take platform flexibility into account during ambiguity resolution using a technique introduced in this thesis (and in [Teague *et al.*, 1996b]) by combining measurements taken during platform motion with a model of platform dynamics. With a sufficiently accurate dynamic model, this technique enables the use of motion-based integer initialization on platforms with large antenna motions due to flexibility.

1.2 Flexible Structure Project Overview

The goal of this research is to develop a sensor for flexible structure motions (vibration and orientation) using measurements of the GPS carrier phase at antennas mounted on the structure. This work includes a laboratory demonstration of the sensor for real-time control of the experimental structure shown in Fig. 1.3 (Chapter 8). The experimental structure moves such that antenna relative motion is in the frequency and sensitivity band of the GPS sensor, with more than 10 observable flexible modes below 2 Hz and centimeter/decimeter level antenna deflections.

The structure was chosen to be representative of the Space Station, but the techniques in this thesis could be applied to any structure with motion that is detectable by current GPS receivers. Other examples include suspension bridges, skyscrapers, oil rigs, radio towers, etc. The GPS sensor could provide valuable information for non-destructive evaluation of structural integrity, and in the presence of actuators, for real-time control.

The rest of this dissertation is arranged as follows. Chapter 2 develops the equations of the DCP observable, its error sources, and its uses. Chapter 3 then discusses the cycle (or

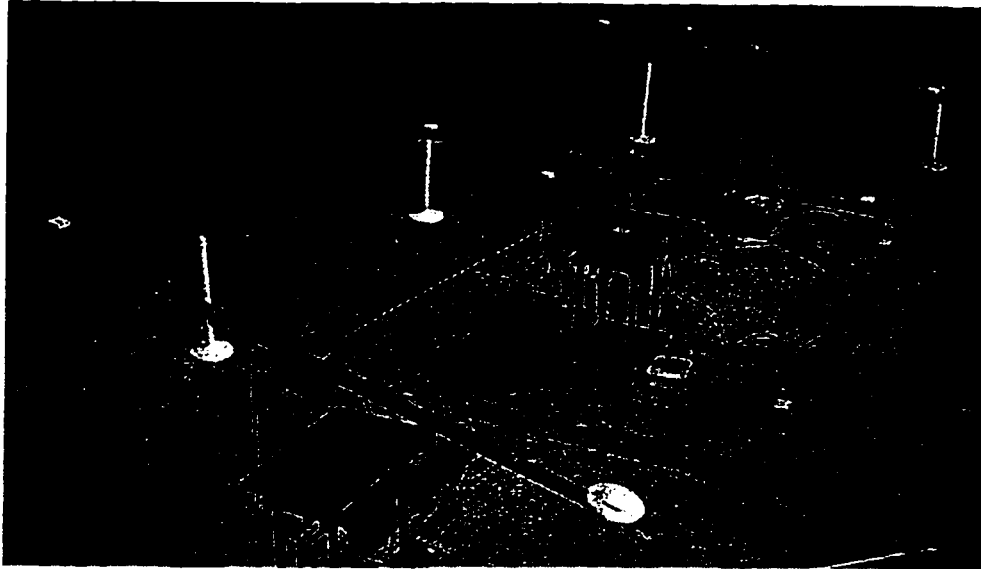


Figure 1.3: The Experimental Structure in Motion

This is a photograph of the experimental structure in motion. The structure is suspended from above by three small threads, and the six GPS antennas are visible as the white patches on circular ground planes at the arm endpoints.

bias⁸) ambiguity and its resolution. The effect of platform flexibility on the bias ambiguity solution is explored in some depth, and an algorithm that takes platform flexibility into account is shown. The details of the experimental hardware used to test the GPS sensor and the processing algorithms are given in Chapter 4.

An overview of the real-time computing system is given in Chapter 5. In this chapter, the philosophy of the hardware and software design is described, and the final implementation is shown. Kinematic and dynamic modeling of the experimental systems is presented in Chapter 6. The experimental work is shown in Chapters 7 and 8. Chapter 7 concentrates on the real-time state estimator, and Chapter 8 describes the control experiments. Finally, conclusions and recommendations for future study are given in Chapter 9.

As an overview of the experimental work in this dissertation, Fig. 1.4 shows a block diagram of the main elements of the control system.

⁸For this work, the cycle ambiguity is considered a continuous *bias*.

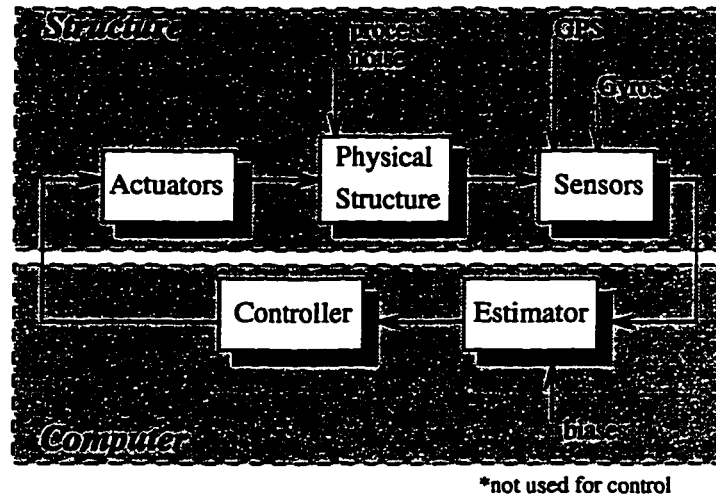


Figure 1.4: Elements in the Control System

This figure shows a block diagram of the primary elements of the experimental system developed for this thesis. The GPS sensing system provides measurements used to control structural vibration and to command orientation slew maneuvers.

1.3 Contributions

The main goal of this thesis is the development of a distributed-antenna GPS-based sensor for structural vibration and orientation control. Contributions described in this thesis were made in the following specific areas during pursuit of this goal:

- This work shows the first demonstration of general structural flexibility sensing and control using only GPS measurements. “General” specifies systems in which antenna motions due to platform flexure are on the same order as those due to overall platform orientation changes.
- This research also shows simultaneous estimation and control of deformation and orientation states of a flexible platform. Control accuracies are demonstrated on the sub-centimeter and sub-degree levels for translation and rotation respectively.
- This dissertation presents development and verification of algorithms that resolve DCP bias ambiguities on a flexible platform, including a method of incorporating a platform dynamic model in bias estimates.

- Hardware techniques are shown for the extension to GPS carrier sensing using a large number of distributed antennas (seven in these experiments) and motivates studies using even larger distributed arrays of interconnected antennas.
- These studies show a simple, low-cost environment for ground-based testing of space platform structural vibration sensing and control. While the experimental structure was not intended to model an actual space platform exactly, the system exhibits the required frequencies and translation magnitudes for flexibility sensing studies in three dimensions.

In addition to the above contributions, the experimental results shown in this dissertation provide confidence in being able to extend these techniques to real-world applications.

CHAPTER 2

The GPS Carrier Phase Measurement

Before designing measurement processing and control algorithms, it is important to understand the fundamental sensor measurement. For this research, the fundamental measurement is the difference in the phase of a GPS signal at two receive antennas. In this chapter, the full non-linear measurement equation is derived and a few simplifications are made based on assumptions that are valid for this research. Since this research requires real-time measurement processing, linearized equations are derived that can be computed efficiently during real-time experimentation. Next, the important measurement error sources are analyzed and quantified. The chapter closes with a comparison between GPS and traditional sensors for flexible structure deformation and attitude.

2.1 Differential Carrier Phase (DCP) Measurement

This research makes use of carrier phase measurements that are differenced between antennas, or differential carrier phase (DCP).¹ The DCP architecture used is a four antenna, six channel Trimble TANS® Quadrex that provides a common clock reference to antenna

¹DCP is also referred to as “single difference” to differentiate from double difference techniques. Some researchers refer to this measurement as carrier differential GPS (CDGPS).

$\alpha = \text{number of antennas}$	2	3	4	5	6	7	8	9	10
$p = \alpha - 1, \text{ for master-slave}$	1	2	3	4	5	6	7	8	9
$p = \sum_{i=1}^{\alpha-1} i, \text{ for all available}$	1	3	6	10	15	21	28	36	45

Table 2.1: Number of Measurements

measurements, eliminating antenna timing based errors. The architecture also uses an antenna multiplexing design (developed for attitude determination [Cohen, 1992; Dentinger and Cohen, 1993]) to reduce the hardware cost and complexity. Also, for reasons of simplicity in hardware, the receiver uses the so-called *master-slave* configuration, in which one master antenna is common to all DCP measurements, and the phase of each slave antenna is measured with respect to that master antenna (see Fig. 2.1). A pair of antennas that is used to produce a DCP measurement is referred to as a *baseline* and the vector from the master to the slave antenna phase center is the *baseline vector*.

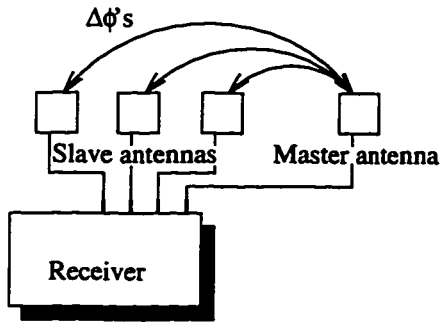


Figure 2.1: Master/Slave Antenna Configuration

Faster processing speed in the latest hardware may make it advantageous to difference all available antennas, rather than using the master-slave configuration. Table 2.1 shows the number of available baseline measurements (per received signal), p , given α antennas in an array for both configurations. The table indicates a rapidly increasing advantage of differencing all available antennas as the number of antennas in an array increases.

2.1.1 DCP Equations

DCP measurements consist of the difference in the line-of-sight distance from a transmitter to each antenna plus bias terms plus noise. The following development is based on results derived in Appendix A. $|\underline{v}|$ denotes the magnitude of the vector \underline{v} . A number under an equals sign denotes a reference to a previous equation. The DCP measurement for a single

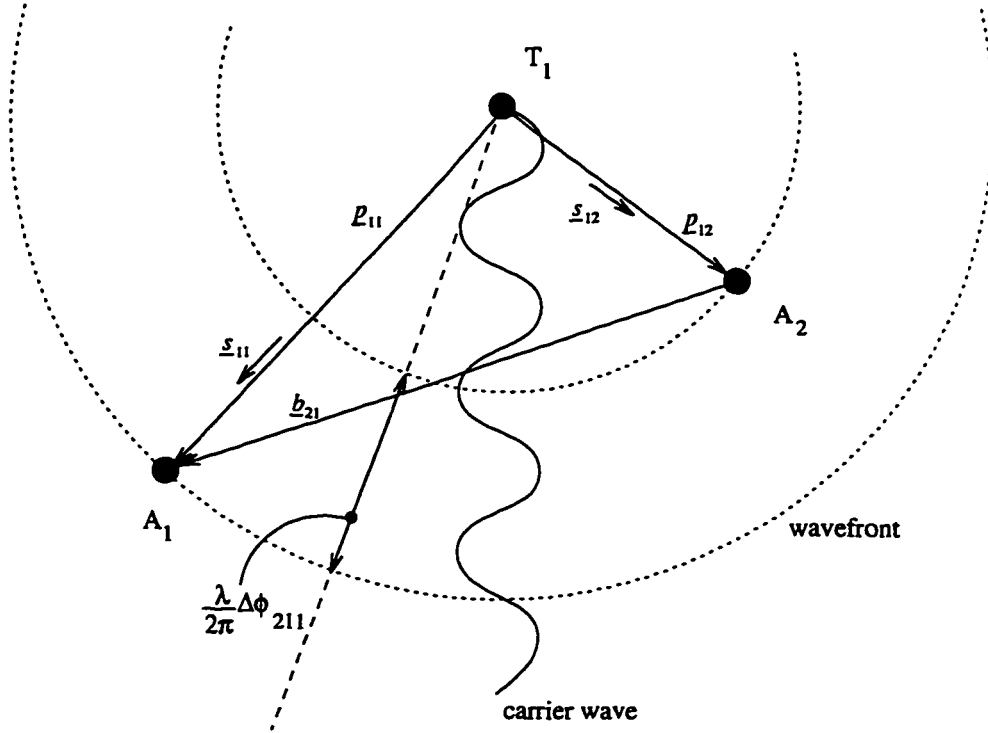


Figure 2.2: DCP Measurement

transmitter and baseline is illustrated in Fig. 2.2. The resulting measurement equation (in units of length) is

$$\frac{\lambda}{2\pi} \Delta\phi_{lij} \stackrel{(A.7)}{=} |\underline{p}_{ji}| - |\underline{p}_{jl}| + \lambda \Delta N_{lij} + \frac{\lambda}{2\pi} \Delta\phi_{line_{li}} + \nu_{lij} \quad (2.1)$$

where the symbols in Fig. 2.2 and Eq. 2.1 are:

- $\Delta\phi_{lij}$ - DCP for antennas l and i , transmitter j
- \underline{p}_{ji} - position vector from T_j to A_i
- λ - the carrier wavelength (approximately 19 cm)
- ΔN_{lij} - the integer ambiguity associated with antennas l and i , transmitter j
- $\Delta\phi_{line_{li}}$ - the line bias (not a function of the transmitter)

ν_{ij} - noise terms

A_i - the point corresponding to the phase center of antenna i ($i = M$ denotes the master antenna)

T_j - the point corresponding to the phase center of transmit antenna j (only 1 is shown in the figure)

\underline{b}_{li} - position (baseline) vector from A_l to A_i

\underline{s}_{jl} - unit (line-of-sight) vector from T_j to A_l

Note that contributions due to antenna phase patterns and polarization (see Eq. A.7) have been dropped. See Section 2.1.3 for a discussion of this assumption. Eq. 2.1 is written for the general case in which all available antennas can be differenced. Henceforth, we will deal only with the master-slave configuration, for which we take $l = M$. Let the absence of the subscript l imply $l = M$, so

$$\frac{\lambda}{2\pi} \Delta\phi_{ij} \stackrel{(2.1)}{=} |\underline{p}_{ji}| - |\underline{p}_{jM}| + \lambda \Delta N_{ij} + \frac{\lambda}{2\pi} \Delta\phi_{linei} + \nu_{ij} \quad (2.2)$$

The following defines some constants that will be used for the remainder of this thesis.

- α - total number of antennas
- $p = \alpha - 1$ - number of baselines (master-slave only)
- r - number of transmitters
- $m = p \cdot r$ - total number of measurements

And, letting $M = \alpha$ (giving the master antenna the largest antenna index) for convenience, the phase measurements (from Eq. 2.2) available to the sensor may be described by

$$\Delta\phi_{ij}, \quad i = 1 \dots p, \quad j = 1 \dots r \quad (2.3)$$

The bias quantities can also be combined into a single variable

$$\beta_{ij} = \lambda \Delta N_{ij} + \frac{\lambda}{2\pi} \Delta\phi_{linei} \quad (2.4)$$

It is advantageous to write Eq. 2.2 in vector and matrix notation. This can be accomplished by combining the measurements into a stacked vector, y (stacking by transmitters,

then baselines):

$$y = \frac{\lambda}{2\pi} \begin{bmatrix} \Delta\phi_{11} \\ \Delta\phi_{12} \\ \vdots \\ \Delta\phi_{1r} \\ \Delta\phi_{21} \\ \vdots \\ \Delta\phi_{pr} \end{bmatrix} \quad (2.5)$$

Finally, we can condense the equations into the simple, standardized form

$$\boxed{y \underset{(2.2,2.4,2.5)}{=} h(x) + \beta + \nu} \quad (2.6)$$

where,

x - state vector (to be defined)

$h(x)$ - measurement function

and β_{ij} and ν_{ij} are stacked in the same manner as Eq. 2.5 to form β and ν , respectively. The state vector, x , is a vector of variables that completely describes the configuration of the antennas. Note that the majority of this work is dedicated to estimating x , given measurements y . Since we assume that the transmitter positions are known, then the position vectors, $|\underline{p}_{ji}|$ from Eq. 2.2, are completely described by x , and $h(x)$ is equal to $|\underline{p}_{ji}| - |\underline{p}_{jM}|$ stacked in the same manner as Eq. 2.5.

$$h(x) = \begin{bmatrix} |\underline{p}_{11}| - |\underline{p}_{1M}| \\ |\underline{p}_{21}| - |\underline{p}_{2M}| \\ \vdots \\ |\underline{p}_{r1}| - |\underline{p}_{rM}| \\ |\underline{p}_{12}| - |\underline{p}_{1M}| \\ \vdots \\ |\underline{p}_{rp}| - |\underline{p}_{pM}| \end{bmatrix} \quad (2.7)$$

To summarize Eq. 2.6, y are measurements from the receiver that consist of differential line-of-sight distances, $h(x)$ (which are completely specified by the antenna configuration, x), plus bias terms, β , plus noise, ν . Transmitter phase centers positions are assumed known.²

2.1.2 Linearized DCP Equation

This section is split into two parts. The first is a general linearization of Eq. 2.6. The second part is a partial linearization that is valid when the transmitters are very distant from the receive antennas, such that the incoming wavefronts are well approximated as planar.

General linearization

Given a guess of the state vector, \hat{x} , Eq. 2.6 may be linearized about \hat{x} to form,

$$y \underset{(2.6)}{\cong} h(\hat{x}) + H(\hat{x})\delta x + \beta + \nu \quad (2.8)$$

where,

$$x = \hat{x} + \delta x \quad (2.9)$$

$$H(\hat{x}) = \left. \frac{\partial h}{\partial x} \right|_{x=\hat{x}} \quad (2.10)$$

Clearly, this approximation in Eq. 2.8 approaches equality as $\delta x \rightarrow 0$. This standard linearization will be useful in later sections.

Planar wavefront approximation

A partial linearization of the measurement equation is possible if the transmitters are far from the baselines. The notation and arrangement of Fig. 2.3(A) are consistent with Fig. 2.2. Fig. 2.3(B) depicts the same geometry in the limit as the transmitter T_j moves away from

²For GPS satellites, the satellite location is broadcast as part of a data message modulated on the GPS signal. Pseudolite transmitter positions must be surveyed (see Appendix E).

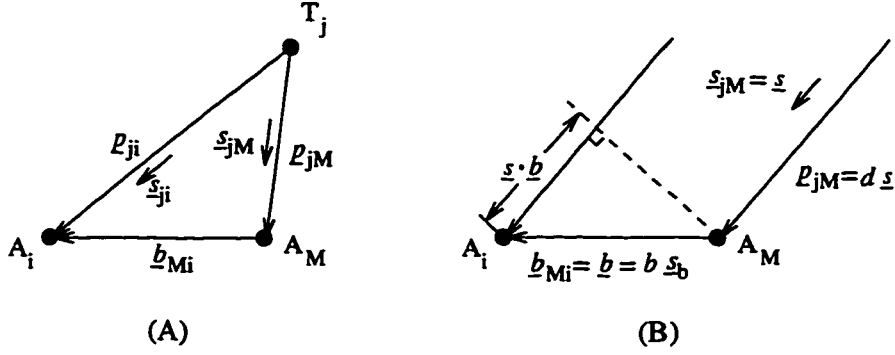


Figure 2.3: Planar Wavefront Geometry

the antennas. For notation convenience, define

$$\begin{aligned}
 \underline{b}_{Mi} &= \underline{b} = b \underline{s}_b \\
 \underline{s}_{jM} &= \underline{s} \\
 \underline{p}_{jM} &= d \underline{s}
 \end{aligned} \tag{2.11}$$

for the case of a single transmitter and a single baseline. \underline{s}_b is a unit vector in the direction of the baseline vector. The geometric portion of the measurement given by Eq. 2.2 is the difference in the position vector magnitudes³

$$|\underline{p}_{ji}| - |\underline{p}_{jM}| = |\underline{p}_{jM} + \underline{b}_{Mi}| - |\underline{p}_{jM}| \tag{2.12}$$

$$\begin{aligned}
 &\stackrel{(2.11)}{=} |d\underline{s} + b\underline{s}_b| - |d\underline{s}| \\
 &= d \left[1 + 2\frac{b}{d}\underline{s} \cdot \underline{s}_b + \left(\frac{b}{d}\right)^2 \right]^{\frac{1}{2}} - d \\
 &= d \left[1 + \frac{b}{d}\underline{s} \cdot \underline{s}_b + \frac{1}{2}\left(\frac{b}{d}\right)^2 \left[1 - (\underline{s} \cdot \underline{s}_b)^2 \right] + \dots \right] - d
 \end{aligned} \tag{2.13}$$

Ignoring the higher order terms in Eq. 2.13 results in the expression

$$|\underline{p}_{ji}| - |\underline{p}_{jM}| \cong \underline{s} \cdot \underline{b} + \frac{b^2}{2d} \left[1 - (\underline{s} \cdot \underline{s}_b)^2 \right]. \tag{2.14}$$

The error term, $b^2/2d$, can be used as a rule of thumb for judging the worst-case first order errors that can be expected due to a planar wavefront assumption.

³The power series expansion is convergent for $|b/d| \leq 1$, which holds for most systems.

In general, wavefronts from the GPS satellites are very well approximated as being planar, due to the large transmit distances (approximately 20,000 km). However, many applications can make use of *pseudolites* (local transmitters that broadcast GPS-like signals). Signals from pseudolites very often have non-planar wavefronts.

With the assumption of planar wavefronts, the partially linearized form of Eq. 2.2 can be written as

$$\frac{\lambda}{2\pi} \Delta\phi_{ij} \stackrel{(2.2)}{=} \underline{s}_j \cdot \underline{b}_i + \lambda \Delta N_{ij} + \frac{\lambda}{2\pi} \Delta\phi_{line i} + \nu_{ij} \quad (2.15)$$

Since this research uses pseudolites with

$$\frac{b^2}{2d} \approx \frac{(3)^2}{2(15)} = 0.3 \text{ m} = 30 \text{ cm}, \quad (2.16)$$

the planar wavefront assumption was not used for this research.

2.1.3 Error Sources

Because the experimentation shown in this thesis was performed indoors using only pseudolite transmitters, some of the error properties seen in the laboratory may not be reproduced exactly outdoors or in space. This section is not intended to be a complete coverage and analysis of system errors, but rather to introduce some of the important errors in the flexible structure control system.

Receiver noise

The carrier tracking phase-lock-loop (PLL) inside the receiver transfers white thermal noise in the raw signal to phase noise with standard deviation

$$\sigma = \sqrt{\frac{B}{C/N_0} \frac{\lambda}{2\pi}} \quad (2.17)$$

where B is the PLL tracking loop bandwidth, C/N_0 is the received carrier-to-noise ratio, and λ is the carrier wavelength [Carlson, 1986]. This shows a direct tradeoff between receiver noise and tracking bandwidth. Because the PLL bandwidth must be (comfortably) above the maximum frequency of detected antenna motion, this fundamentally limits the

vibration frequencies that are detectable. The receivers used in this work were set to a 10 Hz tracking bandwidth, and for typical C/N_0 values, this conservatively translates into a 5 mm noise standard deviation [Pervan, 1996].

This noise level effectively limits GPS sensing to large structures that undergo relatively large amplitude, low frequency vibrations. However, technology improvements that increase the C/N_0 at the phase detector will allow an increase in PLL bandwidth. These changes should enable detection of higher frequency motion, thereby increasing the number of observable modes in a particular structure. For example, aircraft wing flex in turbulence is on the cusp of observability with today's receiver technology.

Multipath

Multipath errors are caused by the reception of unwanted reflected signals at the antenna. Multipath errors are usually significant and sometimes dominant in DCP measurements. Unfortunately, multipath is not well approximated as a white noise signal, limiting the usefulness of time averaging. Given the results of multipath experiments with the same equipment used here (see [Cohen, 1992; Pervan, 1996]), a multipath error magnitude of 1-2 cm is a good conservative estimate, even in the indoor environment. Smaller multipath signals can be expected outside where there are fewer reflective surfaces.

Antenna motion tends to dither the multipath by changing the difference between the reflected and direct signal path lengths. Thus, multipath signals at antennas mounted on a vibrating or rotating structure are likely to be significantly whitened, especially reflections from nearby surfaces where the dithering effect is amplified.

Transmitter position error

The transmitter phase centers are assumed to be known for the calculation of the position vector magnitudes in Eq. 2.1. For the laboratory work shown in this thesis, transmitter positions are estimated using a survey technique as described in Appendix E. It is estimated that the transmitter positions were calculated to within a 20 centimeter radius sphere of truth using this technique.

DCP error due to transmitter position error grows as the ratio of baseline length to transmitter distance increases. So, for the laboratory experiments with pseudolites, accurate transmitter position estimates are especially important. Fig. 2.4 shows the average DCP error magnitude given a particular radial transmitter position offset. Each data point was created by averaging multiple simulations of transmitter locations distributed evenly on a sphere centered at the nominal location. As expected, the error decreases dramatically for increasing transmitter distance, d . But, for indoor experiments, d is constrained to the room size, and for the experiments shown in this thesis, $d \approx 20$ m. So, for a 20 cm radius sphere, an estimate of DCP for the experimental system of 5 mm is assumed.

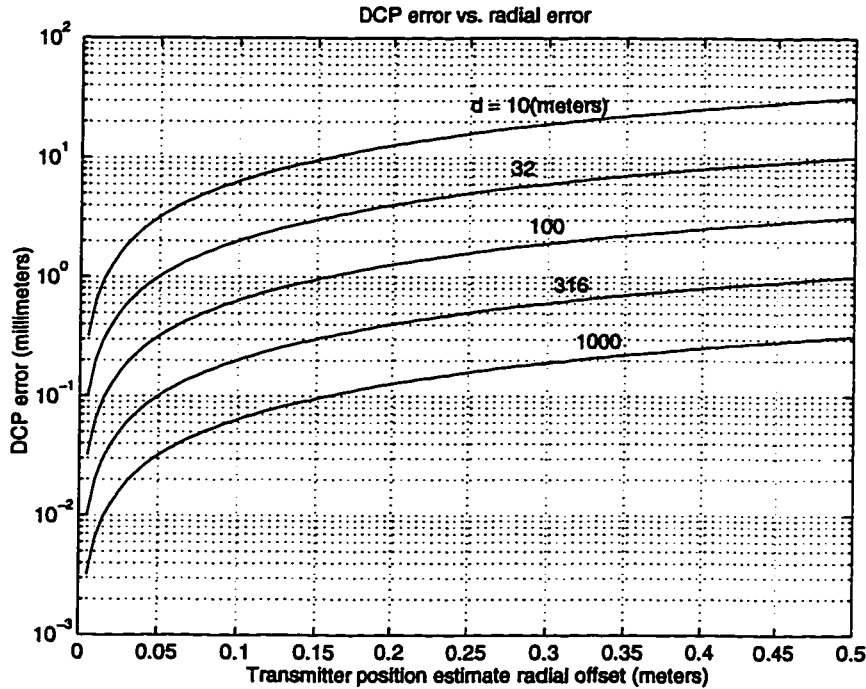


Figure 2.4: DCP Error from Transmitter Position Error

This plot shows errors in the DCP measurement that are due to an imperfect knowledge of transmitter phase center position. Curves for several values of d , the transmitter to receive antenna distance, are given.

Antenna relative attitude error

The antenna attitude error is a carrier ranging error due to the relative orientation of the user antenna to the incoming wave, and due to the circular polarization of the GPS signal. (This effect is denoted ϕ_{pol} in Appendix A.) If the user antenna is rotated about an axis through its phase center, the measured phase may change even though the distance from transmitter to antenna phase centers is constant. For the patch antennas used here, the antenna output depends on the E -field vector as seen in the antenna frame. As an example, if the receive antenna is rotated by some angle about its boresight, the received phase will change by the same angle.

For differential systems, the effect is a function of the relative attitude between antennas and the incoming signal direction. This effect has been largely neglected for DCP systems in the past because antennas pairs have been arranged with common boresight directions by default. The error cancels for aligned antennas. For example, most attitude determination systems have used antennas mounted with common boresight directions. A notable exception was the RADCAL spacecraft work [Cohen *et al.*, 1993] where the antennas were canted for practical reasons.

A simple simulation was performed to illustrate the magnitude of this error for one type of motion. Fig. 2.5 shows two patch antennas that are pointed straight up toward a signal source. The antennas can be canted away from one another by the angle, ψ . Fig. 2.6 shows the error as the antennas are rotated about an axis through the antenna phase centers for several values of ψ . The error is zero, as expected, for the aligned boresight case ($\psi = 0$), but for perpendicular boresights ($\psi = 45^\circ$), the error can reach 5 cm, a significant error for most DCP error budgets. This simulation used the analysis in Section 6.4 of [Lawrence, 1996].

For rigid-body attitude determination systems, the relative antenna attitude is a known constant. Thus, the correction in DCP due to this effect is only a function of the unknown platform attitude, and thus, it becomes a part of the attitude solution. However, antenna relative attitude in flexible systems constantly changes as the platform deforms.

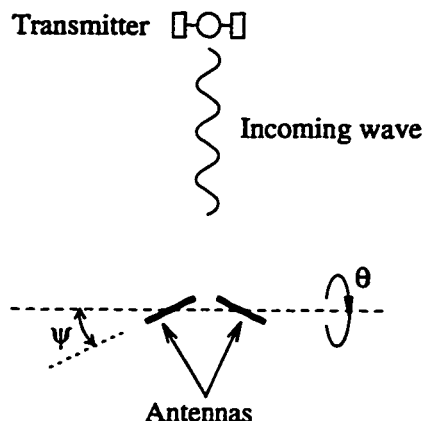


Figure 2.5: DCP Error from Relative Antenna Attitude

This is a simulated antenna configuration to show the effect of canted antennas in the DCP measurement.

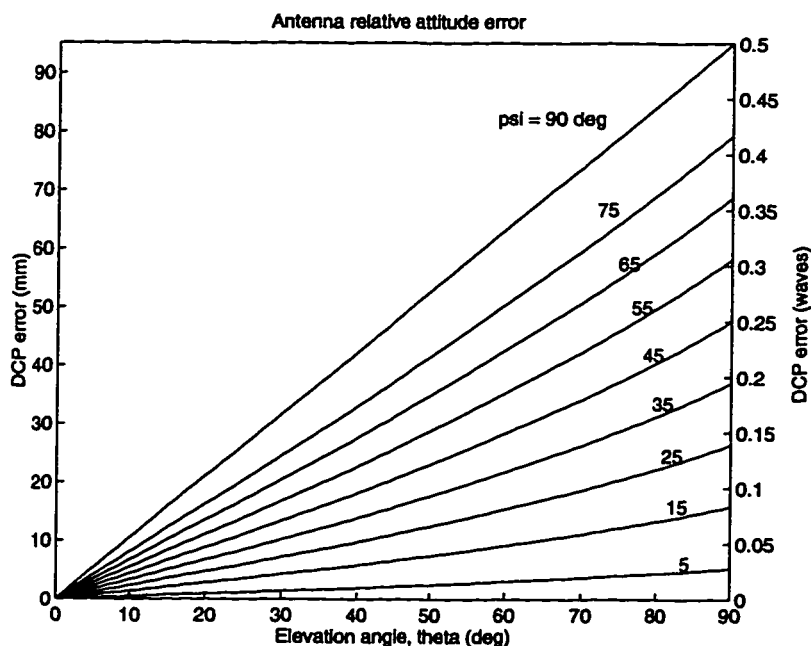


Figure 2.6: DCP Error from Relative Antenna Attitude

This plot shows the DCP error signature as the antenna pair shown in Fig. 2.5 is rotated about an axis through the antenna phase centers. Curves are shown for several values of the cant angle, ψ .

For the flexible structure built for this thesis, antenna relative attitude motions have a limited magnitude. A conservative estimate of the total DCP error due to this effect is 2 centimeters maximum for a particular antenna pair. However, all antennas are aligned in the static configuration of the experimental structure. Given that the error has a relatively small worst-case magnitude and vanishes for the desired configuration (for control), this error was neglected in the experiments shown in Chapters 7 and 8.

Error budget

Table 2.2 summarizes the estimated error magnitudes for individual DCP measurements for the flexible structure experiment. The experimental system uses many redundant measurements (usually 18), reducing the effect of these errors in final state estimates.

Error Source	Magnitude (cm RMS)	Comment
<i>Receiver noise</i>	0.5	white
<i>Multipath</i>	1.5	colored
<i>Transmitter position</i>	0.5	negligible for real satellites
<i>Antenna Relative Attitude</i>	0	neglected (see text)
Total DCP error	2	

Table 2.2: Error Table for Laboratory DCP Measurements

2.2 Comparison with Traditional Sensors

Traditional sensors that might be considered for use on a large space platform include strain, inertial, gravity, star, and magnetic sensors, for example. The list of advantages and disadvantages of these sensors is long and will not be shown here, but it is notable that none of these sensors alone can satisfy the primary space station requirements for absolute platform orientation and internal platform deformation information. A distributed antenna GPS sensor has the potential to satisfy these needs in a single, unified sensor, as demonstrated experimentally in the remainder of this thesis.

The two main advantages of a distributed antenna GPS carrier sensing system are:

1. Because the fundamental observable of GPS DCP is relative range, it provides configuration and orientation information with essentially zero drift. Inertial sensors measure rates and accelerations that must be integrated to provide spatial information. Even high quality inertial instruments (traditionally very expensive) can be limited by the quality of an initialization (in attitude, for example) by some other sensor.
2. The GPS measurements are inherently referenced to a coordinate system that is known and fixed in inertial space — the coordinate system of the GPS satellites. This allows GPS information to be used for internal motion sensing *and* overall orientation sensing simultaneously. Strain sensors and medium to high drift inertial sensors measure only relative (internal) motion and deflection.

The primary limitation of GPS is the sensitivity and bandwidth of motions detectable by current receivers (centimeters of motion below 10 Hz). This sensitivity and bandwidth is sufficient to measure most of the important motions in the space station environment, covering, for example, the primary vibration modes and orientation maneuvers.

For higher frequency, small deflection motion on the space station, or for other applications, GPS could easily be combined with other sensor types. The measurements from different sensors can be processed together to take advantage of the strengths of all of the included sensors. The use of multiple sensors can also provide redundancy improving the robustness to outages or failures.

CHAPTER 3

Bias Ambiguity Resolution

To use the high precision DCP measurements described in the previous chapter to determine the relative positions of antennas is a compelling goal. This information can be useful for analysis and control of many types of engineering systems. Unfortunately, each measurement is corrupted by an unknown bias, and this must be estimated before the measurement is useful. From Chapter 2, the vector measurement equation is

$$y \stackrel{(2.6)}{=} h(x) + \beta + \nu \quad (3.1)$$

If y is an $m \times 1$ vector and x is $n \times 1$, there are m knowns and $m + n$ unknowns in Eq. 3.1. Thus, there are always more unknowns than knowns, so the set of equations does not have a unique solution. This chapter shows ways of finding β using our knowledge of some of the characteristics of β .

3.1 Characteristics of β

The expression for the bias in the ij th measurement (the measurement from the j th signal and the i th baseline) was previously written in Eq. 2.4 as,

$$\beta_{ij} \stackrel{(2.4)}{=} \lambda \Delta N_{ij} + \frac{\lambda}{2\pi} \Delta \phi_{line,i} \quad (3.2)$$

The two main components of this bias are the integer, ΔN , and the line bias, $\Delta \phi_{line}$. ΔN is known to be an integer because it represents the number of full carrier waves in a

differential range measurement, and $\Delta\phi_{line}$ is a real number. Further, ΔN is ambiguous for each measurement every time the signal is acquired. So, each time the receiver is turned on, or a signal is lost, then reacquired, ΔN must be determined. $\Delta\phi_{line}$, however, is mostly a function of the physical hardware, particularly the difference in “electrical length” of the cables of an antenna pair. This bias component is constant for a particular hardware setup.¹ So if it is possible to calibrate the line bias prior to use (which is usually the case), the unknown is an integer.

Because of these characteristics, the bias ambiguity problem for GPS is sometimes referred to as *cycle ambiguity* or *integer ambiguity*. Several methods exist to solve this problem, and these are outlined in the following sections.

3.2 Solution Methods

3.2.1 Integer Search

Search methods have been demonstrated that can determine unknown integers by defining a region of possible integers for a particular application. For example, if it is known that two antennas will never exceed a particular maximum separation distance, the space of possible integers may be constrained. A measure of the accuracy of a particular estimate of the state and bias (\hat{x} and $\hat{\beta}$) is the measurement residual,

$$\rho \stackrel{(3.1)}{=} y - [h(\hat{x}) + \hat{\beta}] \quad (3.3)$$

The search procedure is to pick a candidate integer vector that lies inside the known constraint, and to solve for the best estimate of x given a set of measurements, y . If ΔN is the correct integer set, then ρ should be consistent with the noise magnitude. ΔN is estimated by scanning through all possible integer sets that are inside the constraint, and picking the set that has the lowest residual.

There are two problems with this approach. First, the set of possible integers can be enormous for antennas that may be separated by only several wavelengths. But this

¹Sometimes, large temperature shifts can cause the line biases to drift over time.

is just an issue of computation. More importantly, the technique relies on the following assumption. *It is unlikely that an incorrect set of integers will produce a small residual.* The “unlikeliness” depends on the particular application ($h(x)$ and the integer constraint). In many cases, the assumption is not reliable, and erroneous solutions are possible. Worst of all, the erroneous solutions can be arbitrarily far from the true solution. See [Cohen, 1996] section IV for a graphical visualization of this phenomenon for a pair of antennas on a rigid baseline.

3.2.2 Gradient Search

Another way of determining the ambiguity is to ignore the possible integer character of the variables at first and to do a standard gradient search for the optimal least-squares solution, treating the ambiguities as continuous biases. But a gradient is not defined for the underdetermined Eqs. 3.1. To generate a determined (or overdetermined) set of equations, we use the knowledge that β is a constant over time (while signal lock is held). Thus, if measurements are taken at several instances in time (epochs), an overdetermined set of equations can be achieved because β is the same for all epochs. Again, with m measurements and n independent states at each epoch, we now have Nm knowns and $Nn + m$ unknowns after N epochs, as illustrated in Table 3.1.

epoch	# knowns	# unknowns
1	m	$n + m$
2	$2m$	$2n + m$
\vdots	\vdots	\vdots
k	km	$kn + m$
\vdots	\vdots	\vdots
N	Nm	$Nn + m$

Table 3.1: Building a Determined Set

To have a determined/overdetermined set requires

$$Nm \geq Nn + m$$

$$\text{or, } N \geq \frac{m}{m - n} \quad (3.4)$$

This reveals that $m > n$ (more measurements per state per epoch) is required, which makes sense because, otherwise, additional epochs do not reduce the difference between the number of unknowns and knowns.

While the condition in Eq. 3.4 is necessary to have a determined/overdetermined set of equations, it is certainly not sufficient for a full solution of the problem. A complete statement of the problem at hand is

$$y_k \stackrel{(3.1)}{=} h_k(x_k) + \beta + \nu, \quad k = 1, \dots, N \quad (3.5)$$

$$\rho_k \stackrel{(3.2)}{=} y_k - [h_k(\hat{x}_k) + \hat{\beta}] \quad (3.6)$$

Given:

y_k and h_k , $k = 1, \dots, N$, and
positive definite symmetric weighting matrix, R ,

Find estimates:

\hat{x}_k and $\hat{\beta}$, $k = 1, \dots, N$,

that minimize the cost function

$$J = \sum_{k=1}^N \rho_k^T R^{-1} \rho_k \quad (3.7)$$

Note that the function h is allowed to change with time k to account for the possibility of transmitter (satellite) motion during data collection. That Eq. 3.4 is not *sufficient* to solve Eq. 3.7 should make intuitive sense. If h_k and x_k are constant throughout data collection (if the transmitters and antennas are stationary), no information is added by taking additional measurements over time. The conditions on h_k and x_k that are required for a solution to exist will be explored more completely in Section 3.3. It will be shown that one of the conditions is that the function h_k , which depends solely on transmitter and

antenna positions, varies with k . This condition is why gradient search methods of this type are sometimes referred to as *motion-based methods*.

Assume for now that the conditions for a solution *have* been met. Since Eqs. 3.5, 3.6, and 3.7 are non-linear, a gradient search may not converge, or may converge to a wrong (local) minimum. The convergence of a nonlinear optimization of this type depends primarily on the accuracy of the initial guess. However, a convergence to an incorrect local minimum results in a large final J in practice and is, thus, easily recognizable as an incorrect solution.

The main advantage of gradient search ambiguity resolution techniques over integer search techniques is *integrity*. The additional information added by motion of the system over time makes an undetected erroneous solution very unlikely. For an additional layer of solution integrity, the best estimate of the bias unknowns can be checked to see if ΔN_{ij} in Eq. 3.7 are actually integers, making the probability of an incorrect solution even more remote. For a detailed discussion and derivation of these probabilities, see [Pervan, 1996].

Gradient search techniques were used exclusively for the experimental work shown here, and further references to “bias ambiguity resolution” in this dissertation will imply techniques of this type.

A final note is warranted at this point. It is possible to simultaneously take advantage of the known integer character in biases and to search the solution space in an ordered manner (rather than blind search). See [Hassibi and Boyd, 1995] for more details. Such methods may speed up the solution process, and this is a suggested area for further research.

3.3 Kinematic Bias Estimation

A kinematic bias estimator is a method of solving Eqs. 3.5, 3.6, and 3.7 using knowledge of the function h_k only. As discussed in the previous section, there are conditions on h_k and x_k that are required for a solution to exist. This section will explore those conditions in some depth. First, though, the derivation of the equations for the batch non-linear least squares solution is shown.

3.3.1 A Batch Algorithm

The batch gradient search algorithm is an iterative algorithm for computing a gradient based on the current best guess of the state and updates the state in the direction of the computed gradient. Linearization of the problem about the best guess of \hat{x} and $\hat{\beta}$ is first ($\beta = \hat{\beta} + \delta\beta$). From Eq. 2.8,

$$y_k \stackrel{\cong}{\underset{(2.8)}}{=} h_k(\hat{x}_k) + H_k(\hat{x}_k)\delta x_k + \hat{\beta} + \delta\beta + \nu \quad (3.8)$$

$$\rho_k \stackrel{\cong}{\underset{(3.6,3.8)}}{=} H_k(\hat{x}_k)\delta x_k + \delta\beta + \nu \quad (3.9)$$

Stacking these equations for all $k = 1 \dots N$,

$$\begin{bmatrix} \rho_1 \\ \rho_2 \\ \vdots \\ \rho_N \end{bmatrix} \stackrel{\cong}{\underset{(3.9)}}{=} \begin{bmatrix} H_1 & & 0 \\ & H_2 & \\ & & \ddots \\ 0 & & & H_N \end{bmatrix} \begin{bmatrix} I \\ I \\ \vdots \\ I \end{bmatrix} \begin{bmatrix} \delta x_1 \\ \delta x_2 \\ \vdots \\ \delta x_N \\ \delta\beta \end{bmatrix} + \nu \quad (3.10)$$

Letting,

$$\tilde{H} \stackrel{\cong}{\underset{(3.10)}}{=} \begin{bmatrix} H_1 & & 0 \\ & H_2 & \\ & & \ddots \\ 0 & & & H_N \end{bmatrix} \begin{bmatrix} I \\ I \\ \vdots \\ I \end{bmatrix}, \quad \delta x \stackrel{\cong}{\underset{(3.10)}}{=} \begin{bmatrix} \delta x_1 \\ \delta x_2 \\ \vdots \\ \delta x_N \end{bmatrix} \quad (3.11)$$

thus,

$$\rho \stackrel{\cong}{\underset{(3.10,3.11)}}{=} \tilde{H} \begin{bmatrix} \delta x \\ \delta\beta \end{bmatrix} + \nu \quad (3.12)$$

where,

$$H_k = H_k(\hat{x}_k) \quad (3.13)$$

The weighted least squares solution of Eq. 3.12 is found by iterating

$$\begin{bmatrix} \delta\hat{x} \\ \delta\hat{\beta} \end{bmatrix} = (\tilde{H}^T R^{-1} \tilde{H})^{-1} \tilde{H}^T R^{-1} \rho. \quad (3.14)$$

The iteration starts with an initial guess of \hat{x} and $\hat{\beta}$. Then, use the guess to compute ρ and \tilde{H} and use Eq. 3.14 to refine the guesses using $\hat{x}_{\text{new}} = \hat{x}_{\text{old}} + \delta\hat{x}$ and $\hat{b}_{\text{new}} = \hat{b}_{\text{old}} + \delta\hat{b}$. The process can be repeated until the updates become smaller than some threshold. A good choice of R (from Eq. 3.7) is an estimate of the measurement noise covariance [Bryson and Ho, 1975].

It is now possible to make a concrete mathematical definition of the requirements for a solution, which will henceforth be referred to as *requirements for observability* (of the state $(\delta x, \delta\beta)$ given the measurements δy).

3.3.2 Requirements for Observability

For a solution to Eq. 3.12 to exist, we must be able to evaluate Eq. 3.14, which requires that $(\tilde{H}^T R^{-1} \tilde{H})^{-1}$ exist. Recalling that R is positive definite, this reduces to the requirement that all columns of \tilde{H} be linearly independent, or equivalently, \tilde{H} must have full column rank. So, for state observability, and hence bias observability, in the kinematic estimator,

CONDITION 3.1 *\tilde{H} must have full column rank.*

Henceforth, let “full rank” imply full column rank. There are a few mathematical “sub-requirements” on H_k that must hold for CONDITION 3.1 to be true. These sub-requirements will now be stated and related to their physical significance. This will help us understand the implications of CONDITION 3.1 on real sensing systems. Finally, it will help to explain the failure of these techniques when applied to flexible platform sensing, which motivates the new techniques presented in Section 3.4.

First, the number of epochs, N , must be large enough such that \tilde{H} is *tall* (more rows than columns) or square. As stated before (in Section 3.2.2), this requires that each H_k matrix be tall ($m > n$ from Eq. 3.4). Thus, at each epoch, there must be more measurements than states at that epoch. Now, define the i th column of H_k to be $\eta_k^{(i)}$ such that²

$$\eta_k^{(i)} = \left. \frac{\partial h_k}{\partial x_k^{(i)}} \right|_{x_k = \hat{x}_k} \quad (3.15)$$

² $x_k^{(i)}$ denotes the i th element of the state vector x .

$$H_k \stackrel{(2.10, 3.15)}{=} \begin{bmatrix} \eta_k^{(1)} & \eta_k^{(2)} & \dots & \eta_k^{(i)} & \dots & \eta_k^{(n)} \end{bmatrix}. \quad (3.16)$$

$\eta_k^{(i)}$ is the *sensitivity* of the measurements to perturbations in the i th state variable at $x_k = \hat{x}_k$. It is obvious from the structure of \tilde{H} in Eq. 3.11 that the columns of H_k (namely $\eta_k^{(i)}$) must be linearly independent for \tilde{H} to have linearly independent columns. So, H_k must have full rank (for all k). This leads to the second condition,

CONDITION 3.2 *H_k must be full rank and tall.*

A final requirement (less obvious than the previous) is the following: No column of H_k may be constant for all k . In other words, the sensitivity vector for each state variable must not be constant for all measurement epochs. A proof of this fact is given in Appendix B.

CONDITION 3.3 *No column of H_k may be constant for all k .*

The physical reason for this condition is that a state with constant sensitivity is indistinguishable from bias states in the kinematic estimator. From Eqs. 2.7 and 2.10, H_k is only a function of the transmitter positions at epoch k and the corresponding antenna position estimates, \hat{x}_k . It is this functionality that we use to satisfy CONDITION 3.3. The question now is “what does CONDITION 3.3 imply about the requirements for motion of antennas and transmitters during data collection?” Techniques for satisfying CONDITION 3.3 can be separated into the following two types:

1. **Transmitter motion** - Transmitter motion can provide the variation required in the columns of H_k . This is the main method employed by survey systems that place antennas statically and then wait for the satellites to move. But, since the satellites move slowly, it can take many minutes for the motion to provide the required observability for an accurate measurement. Transmitter motion can be accelerated by using local pseudolite transmitters. Most systems of this type to date use stationary pseudolites and allow antennas to move with respect to the pseudolites to satisfy CONDITION 3.3, for example [Cohen *et al.*, 1995].

2. **Antenna relative motion** - In some circumstances, relative motion of the antennas in an array can satisfy CONDITION 3.3 without transmitter motion. The techniques are sometimes referred to as *motion-based* techniques. This is the most attractive solution (when possible) because it can provide bias observability quickly and without external hardware (such as pseudolites). But CONDITION 3.3 is satisfied by antenna relative motion alone only in certain circumstances, as explained below.

Observability using only antenna relative motion

For the experiments that were conducted for this research, a method of providing bias observability using only antenna relative motion was needed because transmitters (pseudolite) are fixed in the laboratory. For this development, we assume that the signal wavefronts are planar and that transmitters are at fixed points. Then H_k is *only* a function of the antenna position estimates, \hat{x}_k . With this assumption, CONDITION 3.3 becomes

CONDITION 3.3' $h_k(\hat{x}_k)$ *must be a non-linear function of each element of the state estimate \hat{x}_k , and the measurements y must depend on this non-linearity.*

By definition, if $h_k(\hat{x}_k)$ is a linear function of the i th element of the state, then the derivative in Eq. 3.15 with respect to that state variable (namely $\eta_k^{(i)}$) is *constant*. This violates CONDITION 3.3. Thus the function $h_k(\hat{x}_k)$ must be non-linear.

3.3.3 A Simple Physical Example

To illuminate the important physical requirements that must be met to satisfy CONDITION 3.3', we will explore the simplest possible system: a single baseline in two dimensions. Further, assume that the transmitters are fixed, wavefronts are planar, one antenna is fixed, and there are no relative clock errors. These assumptions are typical for motion-based methods. The geometry of this situation is shown in Fig. 3.1. The goal is to find the position(s) of antenna A and the corresponding values for β_j .

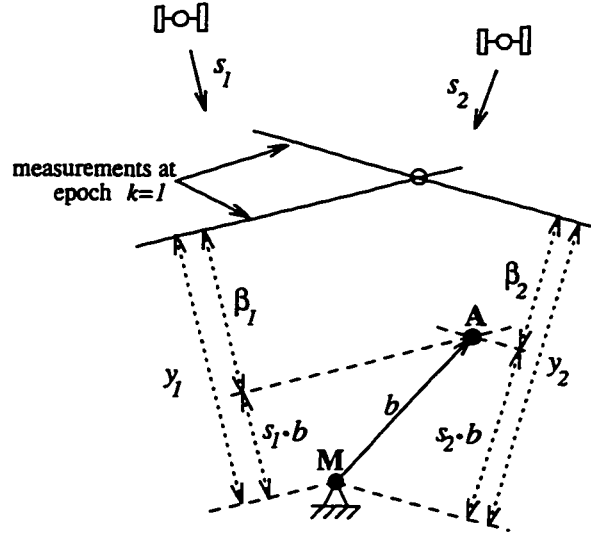


Figure 3.1: A Simple Example

This example shows one baseline with one antenna fixed and the other antenna free to move in two dimensions. The biased measurements are denoted by solid lines perpendicular to the signal arrival direction, and the biased state estimate is shown at their intersection.

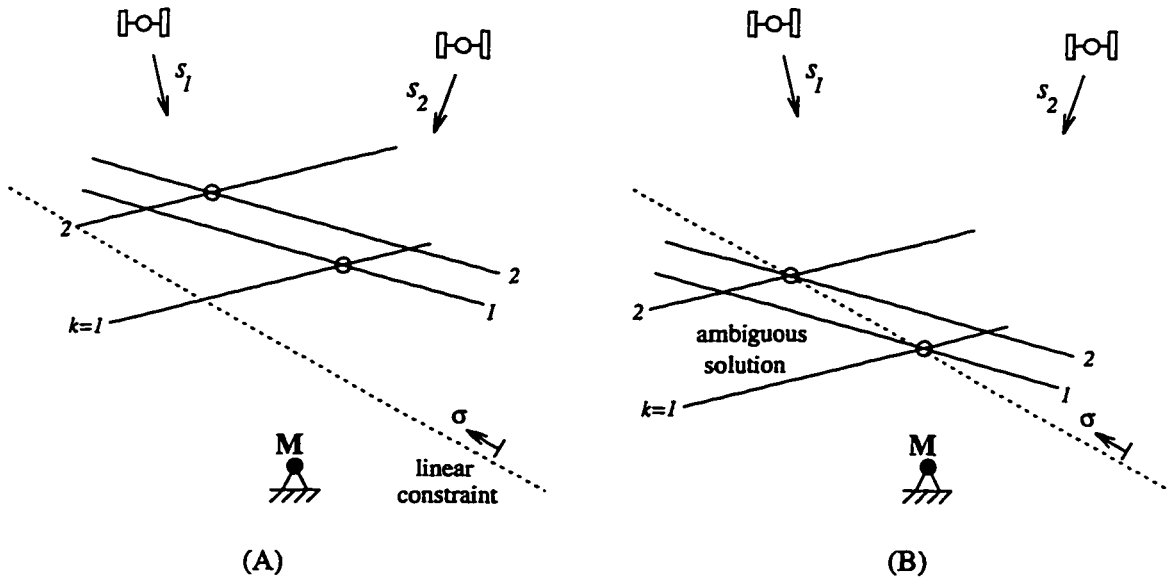


Figure 3.2: Linear Constraint

While providing the constraint of antenna positions as shown satisfies some of the requirements for bias observability, the solution is still ambiguous. We will see that the constraint is insufficient for observability due, in fact, to its linearity.

With these assumptions, the simplified measurement equation becomes,³

$$y_k \stackrel{(3.5)}{=} h(x_k) + \beta + \nu \quad (3.17)$$

$$\stackrel{(3.17, 2.15)}{=} S^T b(x_k) + \beta + \nu \quad (3.18)$$

where,

$$S = \left[\begin{array}{c|c|c|c} s_1 & s_2 & \dots & s_p \end{array} \right] \quad (3.19)$$

This analysis follows from Eq. 2.15 with s_j denoting line-of-sight unit vectors, and b denoting the baseline vector from M to A . The measurements that are available are the biased components of the distance between M and A in the direction of each signal. In the figure, and in subsequent figures, a measurement is denoted by a solid line perpendicular to signal line-of-sight.

To satisfy the requirement for more measurements than states at each epoch (CONDITION 3.2), constrain the motion of antenna A to lie on some known curve. Now, measurements may be collected for a number of epochs while the antenna is free to move along the known curve. Since the position of the antenna may now be defined by a single parameter (the position on the known curve), the state becomes a single scalar value. So, for this example, define the state *scalar*, σ_k . Thus,

$$y_k \stackrel{(3.18)}{=} S^T b(\sigma_k) + \beta + \nu \quad (3.20)$$

One possible example of the curve constraint is shown in Fig. 3.2: a linear curve. The dashed line is the locus of all possible locations of antenna A . Fig. 3.2(A) shows the measurement from two transmitters at each of two epochs. These measurements define the solid lines shown, and the distance between the lines of measurement for a particular transmitter is known.⁴ However, the absolute location of the lines for a particular transmitter is not known due to the bias ambiguity. The intersection of the measurement lines from the two

³Note that h is no longer subscripted by k because with stationary transmitters, h is a constant function of x_k .

⁴As long as the receiver successfully tracks the signal from the transmitter between measurement epochs.

transmitters define candidate state values, denoted as open circles. Because the relative position of the lines of measurement is known (and because the wavefronts are planar), the pattern of circles can be thought of as being fixed with respect to itself, but free to translate in any direction as a whole in the two dimensions of the page. Solution of the problem can be thought of as shifting the fixed pattern of circles (equivalent to adjusting the biases) until the antenna locations for all epochs are consistent with the constraint, as in Fig. 3.2(B). However, with the linear constraint shown, the position of the pattern on the constraint is ambiguous. We can show that this makes sense mathematically given the requirements developed above. Since the constraint is linear, we can write the 2D baseline vector as $b(\sigma_k) = B\sigma_k$, where B is a (2×1) linear transformation. Thus,

$$y_k \underset{(3.18)}{=} S^T B \sigma_k + \beta + \nu \quad (3.21)$$

$$h(x_k) \underset{(3.18, 3.21)}{=} S^T B \sigma_k \quad (3.22)$$

$$\text{and,} \quad H_k \underset{(2.10)}{=} \frac{\partial h}{\partial \sigma_k} = S^T B \quad (3.23)$$

which is *constant*. So, Eq. 3.22 violates CONDITION 3.3', and Eq. 3.23 violates CONDITION 3.3.

If, instead of the linear constraint on the antenna positions, a general non-linear curve is specified as the constraint used to satisfy CONDITION 3.2, a solution may be obtained. This case is as shown in Fig. 3.3(A). The solution for the correct states and biases is shown as the solid circles in Fig. 3.3(B). This example graphically shows how CONDITION 3.3' provides bias observability. As shown in Fig. 3.3(B), an alias solution can exist because more than one location of the pattern of circles satisfies the known constraint. In practice, the potential for an alias solution can be greatly reduced by taking measurements at many more than two epochs.

This simple example shows physically how non-linear measurement functionality provides bias ambiguity observability for motion-based resolution methods (antenna motion only). The non-linear constraint allows separation of the biases, that map into the measurement linearly, from the state.

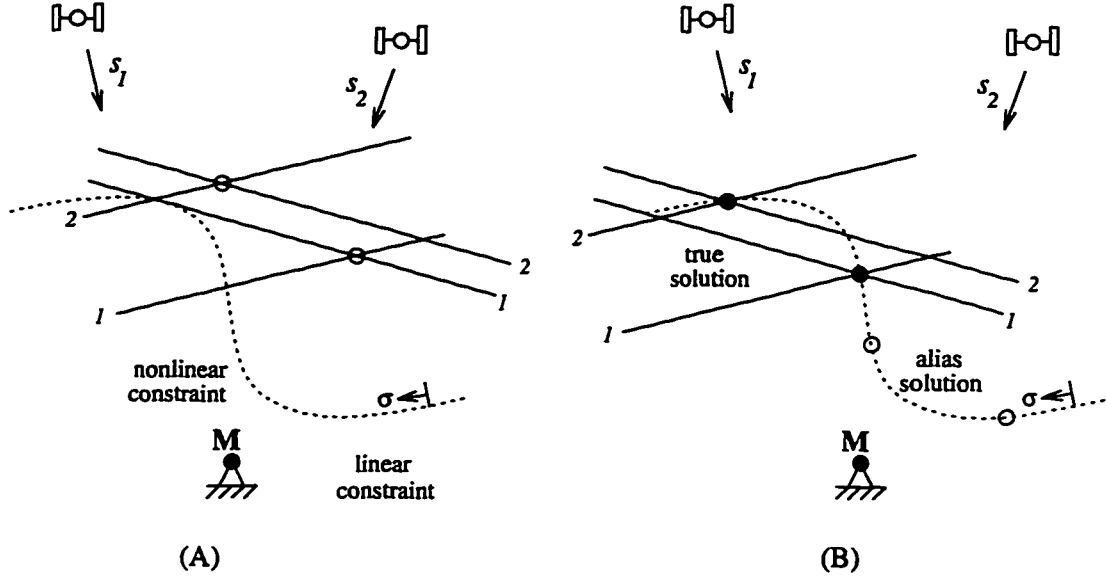


Figure 3.3: Nonlinear Constraint

This figure shows how a general non-linear constraint provides observability for an unambiguous solution for states and biases — almost. Fortunately, the alias ambiguity shown can often be solved by taking measurements at many epochs.

It is this principle that provides observability for GPS-based attitude determination systems using platform motion to initialize the unknown biases. In this case, the constraint is a rigid baseline. For our current example, this case can be represented as a curve of constraint which is a circle centered at the rigid antenna. Fig. 3.4(A) shows the raw measurements at five epochs and the rigid baseline constraint. Bias resolution moves the pattern such that it coincides with the line of constraint, as shown in Fig. 3.4(B). The additional measurement epochs remove the possibility of alias solutions.

3.3.4 Effect of Platform Flexibility

The previous section showed the fundamental requirements for bias observability in a GPS system using antenna relative motion alone. The next topic is one of the primary concerns of this thesis. GPS carrier attitude determination systems use the knowledge that the platform is rigid (with known antenna placement) as the kinematic constraint that allows estimation of bias unknowns. However, some platforms are not well modeled as rigid. As

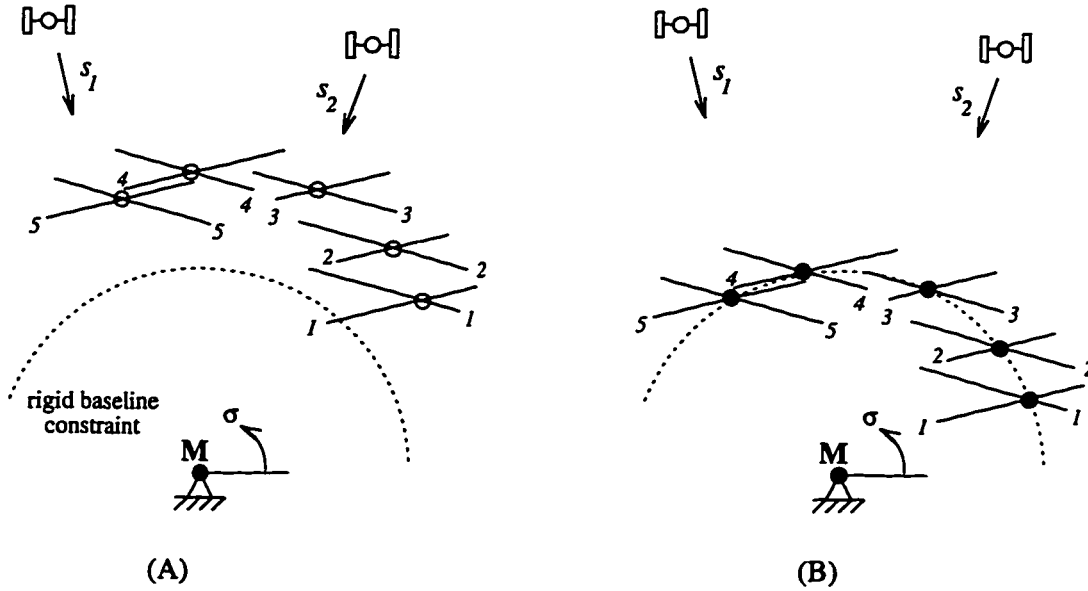


Figure 3.4: Rigid Baseline Constraint

The rigid baseline is a specific type of non-linear antenna motion constraint that applies when antennas are mounted on the same rigid platform. The figure shows an unambiguous solution given measurements at five epochs. The next question is, "How does flexibility in the platform affect bias estimation?"

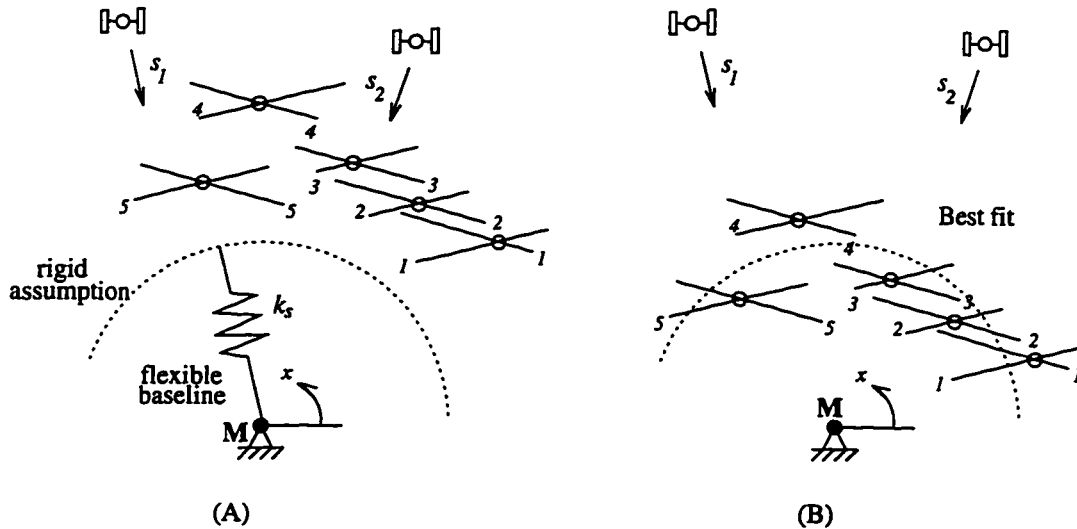


Figure 3.5: Flexible Baselines

Flexibility in a platform causes the antenna motion to deviate from the known constraint, introducing error into the bias solution. Since the kinematic algorithms depend on the constraint for observability, the error cannot be removed. And, as antenna motion due to flexibility becomes large, the kinematic algorithm fails.

the influence of platform flexibility on the measurements increases, solution for biases using the rigid constraint degrades.

Fig. 3.5(A) shows an adaptation of the previous simple example that has a baseline modeled as a spring, with spring constant k . Measurements are taken during motion that includes extension and compression of the spring. The degree to which a rigid constraint approximates the true kinematics depends on the spring stiffness. If the spring is very stiff, then the approximation is good. However, as the spring stiffness is made smaller, the constraint becomes less valid, and the position of the antenna is no longer well approximated with a single state parameter; and we know that without the constraint to provide the non-linearity in the measurement, the biases cannot be estimated. Fig. 3.5(B) shows a best fit for measurements taken given a spring of “intermediate” stiffness. Bias estimates for this measurement set would be marginal.

Cohen took platform flexibility into account during studies of GPS carrier based attitude determination on aircraft [Cohen, 1992]. He noted that wing flexure would unacceptably degrade attitude estimates, and included a wing flex state in addition to the attitude states to describe the relative position of the antennas on the aircraft. But since wing flex was small and linear, it was not observable as a dynamic state during bias determination using platform motion alone (due to CONDITION 3.3'). Because it was known that flex was relatively small, wing flex was *assumed to be constant during data collection for bias determination*.

This flex was included mathematically as a bias in the state space as follows:

$$\begin{bmatrix} \rho_1 \\ \rho_2 \\ \vdots \\ \rho_N \end{bmatrix} \stackrel{(3.10, 3.15)}{=} \begin{bmatrix} H_1 & & 0 & \eta_1^{(flex)} & I \\ & H_2 & & \eta_2^{(flex)} & I \\ & & \ddots & \vdots & \vdots \\ 0 & & H_N & \eta_N^{(flex)} & I \end{bmatrix} \begin{bmatrix} \delta x_1 \\ \delta x_2 \\ \vdots \\ \delta x_N \\ \delta f \\ \delta \beta \end{bmatrix} + \nu \quad (3.24)$$

where,

δf - the wing flex bias state

$\eta_k^{(flex)}$ - sensitivity of the measurements to perturbations in the flex state, δf

It is interesting to note that the sensitivities, $\eta_k^{(flex)}$, must not be constant over k , or the flex state will not be observable. A proof of this is very similar to the proof in Appendix B.

As the flexibility of the platform increases to the point that the magnitude of relative antenna motion due to flexibility is on the order of that due to overall platform orientation changes, the kinematic approach of Eq. 3.24 fails. Also, for large elastic motions, modeling the flexibility as a constant bias (as in Eq. 3.24) is rarely sufficient. This point is demonstrated in Section 3.4.2 with some simulations of a simple spring/mass system. But, before showing the simulations, a method of estimating biases is shown that can take flexibility into account using a known model of platform dynamics.

3.4 Dynamic Bias Estimation

In this section, an alternate approach to bias estimation is derived that incorporates platform model information. It is shown that the dynamic approach not only adds more information to the estimator but also provides observability that is *not* present in a kinematic estimator for platforms with significant flexibility. These results are demonstrated with simulations of our simple single baseline example for a range of spring constants. But first, the equations of the dynamic estimator are developed.

3.4.1 A Second Batch Algorithm

If the antennas are mounted to a system for which we have a dynamic model, it is possible to use this information to improve our bias estimate. For example, given a (discrete) dynamic model of the form,

$$x_{k+1} = Ax_k + B_w w_k, \quad k = 1, \dots, N-1 \quad (3.25)$$

with w_k a vector of unknown process noise at epoch k . If the augmented state

$$x_{aug} = \begin{bmatrix} x_1 \\ w \\ \beta \end{bmatrix} = \begin{bmatrix} x_1 \\ w_1 \\ w_2 \\ \vdots \\ w_{N-1} \\ \beta \end{bmatrix} \quad (3.26)$$

is formed, a linearized equation that incorporates all the data and known system information (Eqs. 3.17, 3.25, and 3.26) is given by [Bryson, 1993].

$$\begin{bmatrix} \rho_1 \\ \rho_2 \\ \vdots \\ \rho_N \\ 0 \\ 0 \\ \vdots \\ 0 \end{bmatrix} = \begin{bmatrix} H_1 & 0 & 0 & 0 & 0 & I \\ H_2 A & H_2 B_w & 0 & 0 & 0 & I \\ H_3 A^2 & H_3 A B_w & H_3 B_w & \cdots & 0 & I \\ H_4 A^3 & H_4 A^2 B_w & H_4 A B_w & & 0 & I \\ \vdots & \vdots & \vdots & \ddots & \vdots & \vdots \\ H_N A^{N-1} & H_N A^{N-2} B_w & H_N A^{N-3} B_w & \cdots & H_N B_w & I \\ \hline & & & I & & \end{bmatrix} \begin{bmatrix} \delta x_1 \\ w_1 \\ w_2 \\ \vdots \\ w_{N-1} \\ \delta \beta \end{bmatrix} + \nu \quad (3.27)$$

The process noise, w_k , is not written as a perturbation because it is assumed to be a linear effect and zero mean. The zeros on the left and the lower partition identity matrix provide a means of quantifying the process noise covariance for a least squares solution (as shown below). Now defining a new matrix, \tilde{A} as

$$\tilde{A} = \begin{bmatrix} I & 0 & 0 & 0 & 0 & 0 \\ A & B_w & 0 & 0 & 0 & 0 \\ A^2 & A B_w & B_w & 0 & \cdots & 0 \\ A^3 & A^2 B_w & A B_w & B_w & & 0 \\ \vdots & \vdots & \vdots & \vdots & \ddots & \vdots \\ A^{N-1} & A^{N-2} B_w & A^{N-3} B_w & A^{N-4} B_w & \cdots & B_w \\ 0 & 0 & 0 & 0 & \cdots & 0 \end{bmatrix} \quad (3.28)$$

leads to

$$\begin{bmatrix} \rho \\ 0 \end{bmatrix} \stackrel{(3.11, 3.27, 3.28)}{=} \begin{bmatrix} \tilde{H} \tilde{A} \\ I \end{bmatrix} \begin{bmatrix} \delta x_1 \\ w \\ \delta \beta \end{bmatrix} + \nu \quad (3.29)$$

with \tilde{H} the same as in the kinematic equations of Section 3.3.1 (i.e. Eq. 3.11).

The procedure for performing a batch dynamic solution of the measurement biases is as follows.

1. Collect and store measurements at N equally spaced epochs as the physical system is in motion.
2. Define the diagonal weighting matrix $W = E[w_k w_k^T]$ as the best estimate of the process noise covariance. As in Eq. 3.14, define $R = E[\nu_k \nu_k^T]$ as the best estimate of the white measurement noise covariance.
3. Define the diagonal weighting matrices, \mathfrak{B}^{-1} and X_1^{-1} . These determine the relative weighting of the $\delta\beta$ and δx_1 portions of the state, and nonzero values limit the magnitude of β and x_1 updates per iteration. They may be set to zero or scaled to improve convergence of the batch estimator.
4. Perform the batch solution by iterating Eq. 3.30 until convergence.

$$\begin{bmatrix} \delta \hat{x}_1 \\ \hat{w} \\ \delta \hat{\beta} \end{bmatrix} = \left(\tilde{A}^T \tilde{H}^T R^{-1} \tilde{H} \tilde{A} + \begin{bmatrix} X_1^{-1} & \\ & W^{-1} \\ & & \mathfrak{B}^{-1} \end{bmatrix} \right)^{-1} \tilde{A}^T \tilde{H}^T R^{-1} \rho \quad (3.30)$$

The iterative algorithm is required because of the non-linearity in the measurement equation (\tilde{H} depends on the state). The dynamic solution requires much more information about the system dynamics and noise, but it provides a way to explicitly include a model in the batch algorithm.

3.4.2 The Simple Example, Revisited

Here, a numerical simulation is shown that compares the performance of the kinematic and dynamic bias estimators using the simple example of a flexible baseline of Section 3.3.4

A diagram of the system is shown in Fig. 3.6, and the state variables are r and θ , as shown. The linearized equations of motion⁵ are

$$\ddot{r} = - \left(\frac{k_s}{m_a} \right) r \quad (3.31)$$

$$\ddot{\theta} = 0 \quad (3.32)$$

⁵We use the linearized equations for this example so that the model will be consistent with Eq. 3.25. This allows us to compare the performance of the kinematic and dynamic approaches directly using the simple example of this chapter.

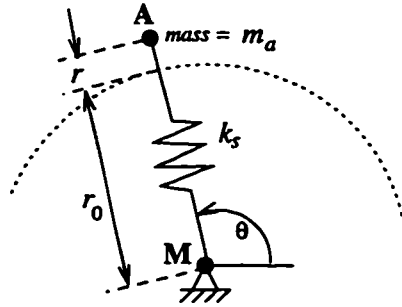


Figure 3.6: Simple System Diagram

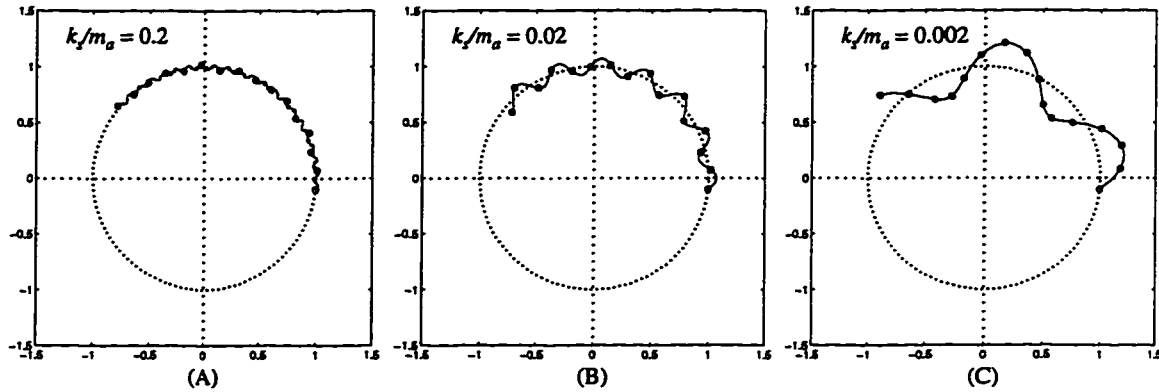


Figure 3.7: Free Antenna Motion

This figure shows the motion of the antenna at the spring endpoint given an initial position and velocity. Figures A, B, and C show the antenna motion given different spring constants. This shows that the kinematic constraint becomes less valid as the baseline elasticity increases.

The plots in Fig. 3.7 show the propagation of these equations, given a particular initial condition, for three different spring stiffness values. The plots show that the kinematic constraint for a rigid baseline (or infinite spring stiffness) becomes less valid as the elasticity of the baseline increases.

Since the flexible motion that exists during data collection is unobservable in a kinematic bias estimator, kinematic techniques must ignore such motion.⁶ Fig. 3.8(A) shows the best solution available to the kinematic estimator for a baseline with high flexibility. Although the estimates shown minimize the error in a least squares sense, the state errors are large

⁶ An offset in the nominal baseline length, r_0 , would be an example of a flex bias states, such as δf in Eq. 3.24. We assume here, for simplicity in the example, that the offset is zero.

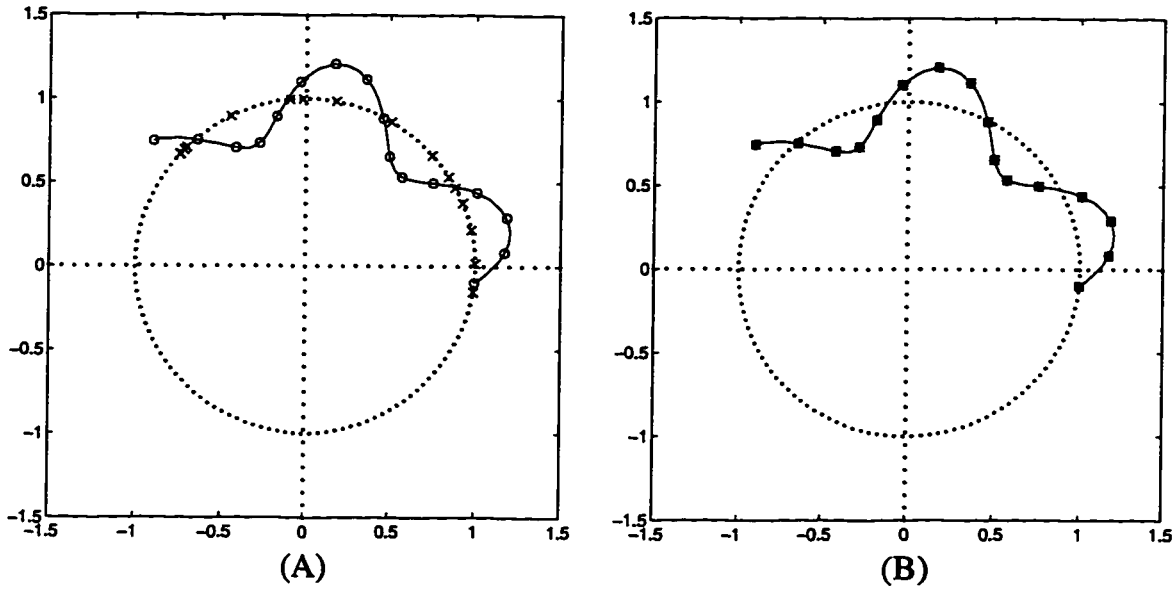


Figure 3.8: Examples of Kinematic vs. Dynamic Solutions

Because the kinematic estimator relies on the nonlinear constraint to provide bias observability, the kinematic solution in (A) must ignore flex motion. Measurement epochs are denoted as circles on the path of antenna motion, and x's are the corresponding converged estimates. The dynamic solution in (B) shows the benefit of dynamic approach.

due to the necessary rigid baseline constraint.

Because of the addition of the platform dynamic model, the dynamic estimator can observe all states, including flexibility. As shown below, the additional information can provide significantly greater bias estimate accuracy. Fig. 3.8(B) shows the solution of the dynamic estimator and illustrates the benefit of using the dynamic algorithm. Because the states of the system can be estimated to greater accuracy, the corresponding bias estimates are also improved. Now, a comparison between the kinematic estimator and the dynamic estimator is shown for a range of platform (baseline) stiffnesses in our simple example. The effect of model accuracy on the dynamic bias estimator is also explored and is found to have a direct impact on the final solution accuracy.

Fig. 3.9 shows the result of repeated simulation trials. Platform rigidity is varied along the horizontal axis with rigidity increasing to the right. The top line shows the performance of the kinematic estimator. The plot reveals that there is a high performance degradation as

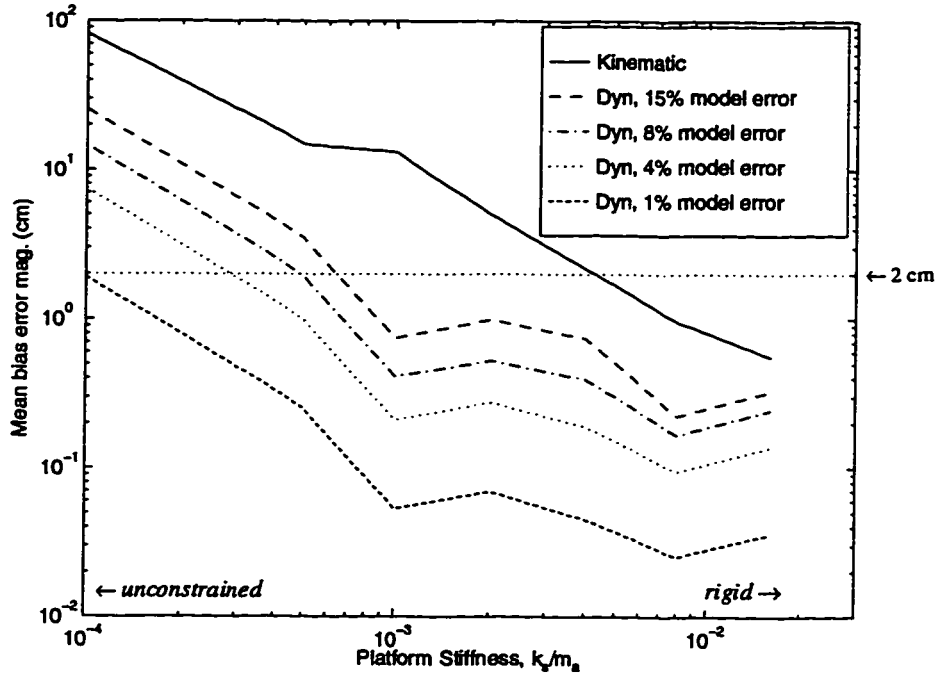


Figure 3.9: Converged Bias Error

This plot compares the bias error of five simulated estimators over a range of spring stiffnesses for the example problem of this section. Dynamic estimators perform better, especially when spring elasticity is high. Also as expected, the dynamic algorithm results degrade with increasing model error.

baseline flexibility increases. These results are for the nominal baseline length of one meter, and bias errors will increase for longer baselines. The results for the dynamic estimator are almost an order of magnitude better even when the model is significantly in error, and are nearly two orders of magnitude better when an accurate model is available.

3.4.3 Observability and Model Accuracy

The primary difference between the dynamic and kinematic estimators of Section 3.3 and Section 3.4 is the assumption of correlation of the states between measurement epochs. The kinematic estimator (Eq. 3.14) assumes that dynamic states at different times are independent, and thus could have an arbitrarily large change between epochs. But it is known that the states at one time are related to another, and it is possible to quantify

this relationship mathematically through the dynamic model. The correlation magnitude is specified through the weighting matrix, W (in Eq. 3.30), with uncertainty in the model information increasing as W increases.

Using the model of correlation between states over time, we eliminate the need for a non-linear constraint of antenna motion. The example was chosen with a non-linear constraint plus flexibility so that the dynamic and kinematic estimators could be compared directly. Though, for cases that are linearly constrained or unconstrained, the dynamic algorithm can still provide a solution.

As one would expect, the performance benefit of the dynamic estimator depends on the accuracy of the available model. Given an a priori estimate of model accuracy, the estimator can be tuned for the best solution by adjusting the parameter W . However, models that are significantly in error could limit the usefulness of the dynamic algorithm. The effect of model error for the simple example of this chapter is shown in Fig. 3.9. The solution with zero model error assumed is not shown because it results in essentially zero estimate error. As the model error increases (realized as a percent error in the spring constant), the resulting bias errors grow. The impact of model error on the bias estimates will depend on the particular application of interest, and this issue is a suggested topic for further investigation.

3.5 Summary

Differential carrier phase measurements contain bias (or integer) ambiguities that must be resolved to realize the potential centimeter level measurement precision. One of the most powerful techniques to determine the biases is to use the knowledge that the biases are fixed in time, combined with measurements taken during geometric motion of the antennas and/or transmitters to allow simultaneous observation of dynamic states and biases. The algorithms discussed in this chapter use gradient search techniques that iteratively linearize the equations about a state estimate, compute a gradient based on the state estimate, and update the state estimate based on the computed gradient. However, these solution

techniques require a full rank linearized measurement matrix. Since the biases linearly span the entire measurement space, additional states must enter the measurement equation in a non-linear way over time to satisfy the full rank requirement.

One method of providing the non-linear functionality required is to take advantage of transmitter motion over time. For some systems, though, it is not possible (e.g. transmitters fixed) or desirable (e.g. slow transmitter motion) to rely on transmitter motion. For these systems, a method of providing measurement non-linearity using antenna relative motion alone is needed. But general antenna motion enters the measurement linearly, and thus is not distinguishable from the measurement biases. If a constraint on the relative motion of antennas is known and if the constraint is non-linear in the measurements, a kinematic solution is obtainable. For example, attitude determination systems use the knowledge that the antennas are mounted to a common rigid platform as such a constraint. And if multiple measurements are taken from the antennas while the rigid platform undergoes large attitude changes, the biases and attitude states can be resolved.

Sometimes, the constraint that is vital to the observability of the biases is only approximately valid. For instance, platforms that are only approximately rigid may allow antenna motions that do not satisfy the constraint exactly. As the platform flexibility increases, kinematic constraints can no longer be used to describe the antenna motion, and kinematic solution algorithms are not sufficient. To address this issue, a bias determination algorithm is shown that eliminates the need for a non-linear kinematic constraint and replaces it with a different type of constraint, a dynamic model. The dynamic model approach enables bias determination in the presence of significant antenna motion caused by platform flexibility during the collection of data.

To demonstrate the requirements for observability in the kinematic estimator and the effect of flexibility on these requirements, a simple example is developed in this chapter consisting of a single antenna pair with one antenna fixed. The essence of the bias estimation problem can be understood from the geometry in the example. Finally, a variation of the example is developed that allows direct comparison of kinematic and dynamic algorithms using a simple spring to provide “platform” flexibility. Simulations of bias estimation are

presented for a range of spring stiffnesses. While the kinematic algorithms perform well for high stiffness, they perform poorly as the magnitude antenna motion due to spring flexibility becomes large. The dynamic algorithms perform well for all the spring stiffnesses studied. It is also shown that the performance of the dynamic algorithm degrades gracefully as model error is increased for the example problem.

CHAPTER 4

The Experimental Hardware

For development and testing of the GPS sensing system for flexible structures, an experimental structure was constructed that has the important characteristics needed for this task. The test structure was built to emulate the motions of a large, flexible, orbiting platform, moving with low frequencies and large structural deflections. The test structure is suspended from an overhead crane in a large high-bay (20 meter) facility at Stanford and is outfitted with sensors and actuators for real-time control experiments. An array of six GPS antennas is mounted on the structure to provide information about the motion and configuration of the structure. However, since the testing is performed indoors, the signals from the GPS satellites are not detectable in the laboratory. To reproduce the GPS signal environment for use in these experiments, a constellation of six GPS pseudolite transmitters was built and mounted on the walls and ceiling of the laboratory.

This chapter presents the details of the experimental hardware, including the physical structure, the actuators, and the sensors.

4.1 The Physical Structure

A structure was designed that has the following characteristics:

- **Large elastic deformations with low damping** - Since a major goal of this work is to study the effect of non-negligible structural elasticity on GPS motion sensing, large elastic deformations are required. Also, the low damping of the system makes it suitable for active vibration control.

- **Antenna motions detectable by GPS** - Antenna motions during system deformation that are detectable by GPS receivers are required. The carrier phase tracking loops in the receivers used for this work have a bandwidth of approximately 10 Hz, and they can detect antenna motions of approximately 1 cm or greater. Motions of a typical flexible orbiting platform are well within these sensor limits.
- **Simultaneous elastic and orientation motion** - A major goal of this work is to study simultaneous control of structure vibrations and overall structure pointing using GPS as the sole source of flex motion and overall attitude information.

The structure is an assembly made primarily of aluminum and steel that hangs from twelve meter threads from an overhead crane. The assembly comprises three massive, and essentially rigid, sections that are connected together in a horizontal line by long, elastic beams with endpoints that are fixed to the rigid sections (see Fig. 4.1). Each rigid section consists of a 25 cm aluminum cube with two iron arms that are rigidly attached to the cube and extend outward in the horizontal plane. The arms provide the mounting points for the antennas and actuators on the structure.

This configuration, with massive rigid sections connected by light elastic beams, provides the low frequencies needed by achieving high mass and high elasticity simultaneously. The elastic beams are 1/2 inch diameter, thin-walled aluminum tubes that bend and twist during motion of the entire system. While the beams are very flexible and long (3.7 meters), they sag only 1 – 2 centimeters at their midpoints due to gravity.

The experimental structure is suspended from above by three long threads. Each thread is attached to one of the rigid sections of the assembly just above its center of mass. This suspension technique reduces the frequency of the suspension induced pendulum modes, and allows the entire system to move like a structure in a zero gravity environment, with low frequencies and low damping. Balancing the structure after full assembly is required and can be performed using mechanisms that allow millimeter-level adjustment of the point of attachment of the suspension thread to the rigid section in three dimensions. The balancing mechanism designed as part of this work is shown in Fig. 4.2.

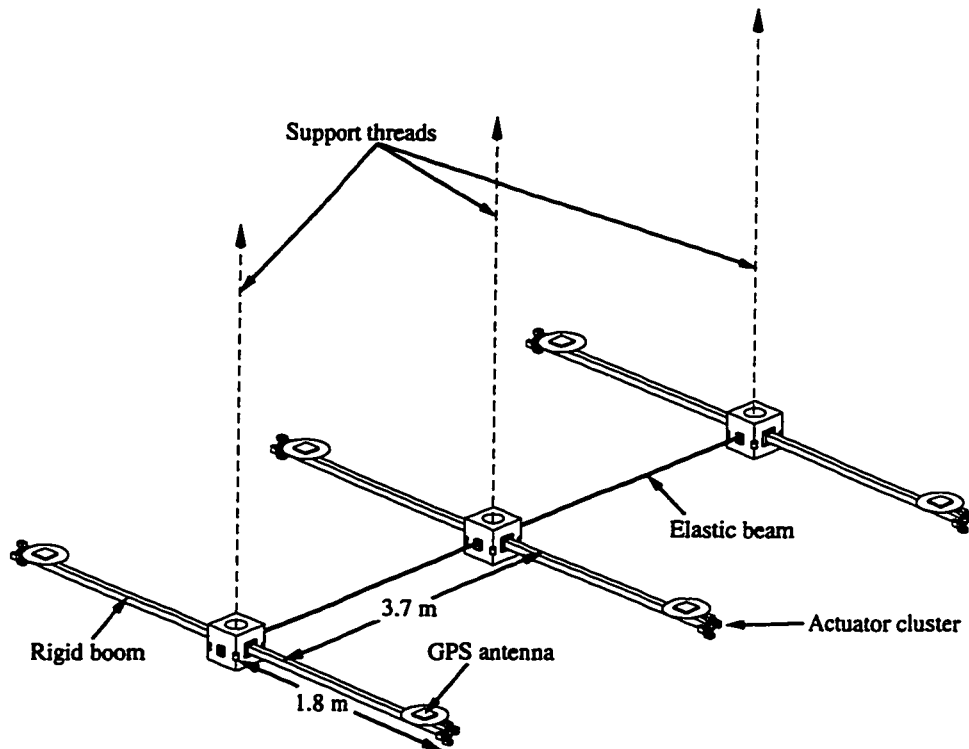


Figure 4.1: A Diagram of the Structure

This is the experimental structure that was used to imitate motion of a flexible orbiting platform. GPS antennas are mounted on the structure to sense deformations and orientation changes of the platform.

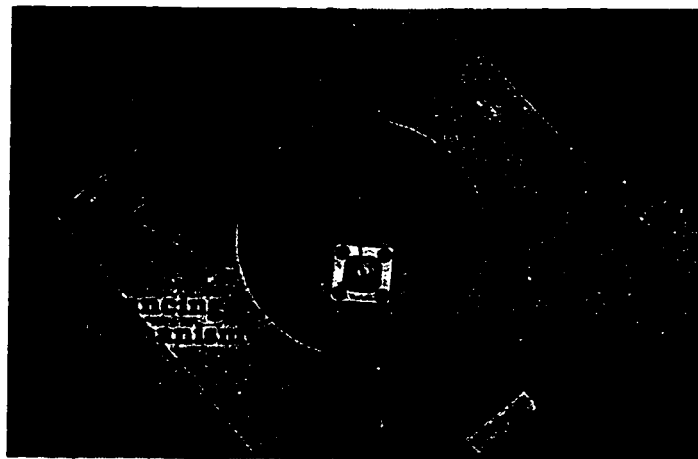


Figure 4.2: Photo of Balance Mechanism

This photograph shows the point of attachment of the suspension thread as seen from above. A frustum is cut in the cube for attachment near the center of mass. A mechanism is shown at the base of the frustum for fine adjustment of the point-of-attachment location for suspension balancing.

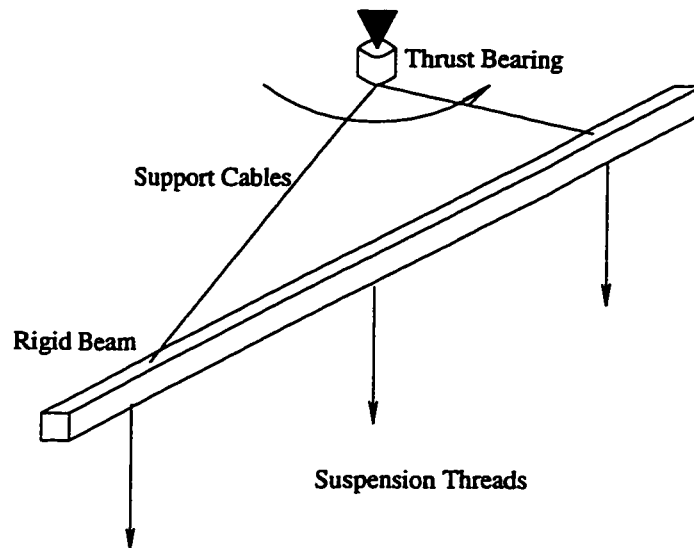


Figure 4.3: Suspension System

Suspension threads are attached at the top to a rigid beam that is free to rotate in the horizontal plane. This freedom enables experiments in pointing control of the structure below.

Finally, to allow overall orientation changes of the structure, the suspension threads are attached at the top to a rigid beam that is mounted to a thrust bearing, allowing the beam, and the structure below, to rotate freely in the horizontal plane (see Fig. 4.3). This rigid-body mode allows experiments in structural pointing control and slew maneuvers.

Fig. 4.4 shows a photograph of the entire assembly. The GPS antennas (square white patches) can be seen at the end of each arm. A person is shown for scale. As shown, the entire structure rests on the three tables prior to experimentation. Before estimation and/or control experimentation, the overhead crane lifts the assembly 40 cm above the table surfaces. Then, it is possible to remove the tables so that they do not interfere with structural motion.

A CAD package called Pro/ENGINEER® by Parametric Technology Corporation was used for designing and drawing the test structure. The program allows direct three dimensional modeling and viewing during the design process. Also, the CAD program was used to generate the drawings of systems and parts for fabrication. Appendix C shows some example drawings from the CAD package.

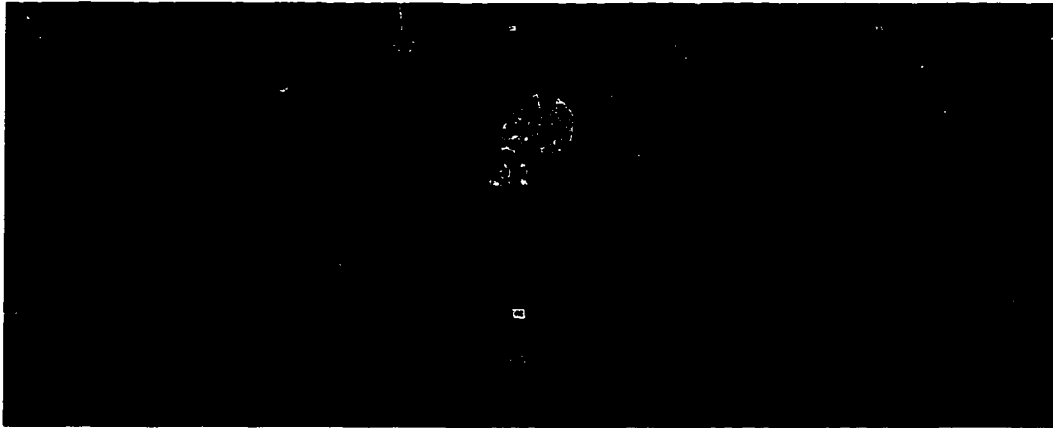


Figure 4.4: Overhead Picture of Assembly

This is a photo of the experimental structure as seen from above. The GPS antennas are the white patches at the end of each arm. Note that the thrusters were not installed when this picture was taken.

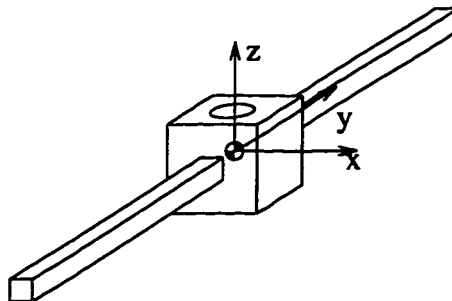


Figure 4.5: Coordinate System for Physical Properties

This is the principle coordinate system used for definition of the physical properties of the rigid sections of the structure.

Dynamic modeling requires estimates of the mass and elasticity properties of the system and subsystems. Physical properties of the system and subsystems were computed using Pro/ENGINEER® and were checked by weighing the system components. See Table 4.1 for the important physical specifications of the test structure, including mass and elasticity properties. The coordinate system used for rigid section inertial properties is shown in Fig. 4.5.

4.2 The Sensors

4.2.1 GPS sensors

Transmitters

Since the testing is done indoors, the signals from the GPS satellites are not detectable. Therefore, a set of six pseudolite transmitters with custom transmit antennas was constructed and mounted on the ceiling and walls of the laboratory. The GPS signal is generated by a credit card-sized integrated circuit designed by Cobb [Cobb *et al.*, 1994] that uses standard, off-the-shelf electronic parts. The electronics are mounted in an RF shield aluminum case. The final product is a pocket sized unit that has a RF output and can run for 24 hours on a standard 9 volt battery.

To broadcast the GPS signal in the laboratory, a helical transmit antenna was built for each pseudolite. The helical design was used because it broadcasts a signal with a narrow beam width and reduces the chance of reflected signals reaching the receiver antennas (multipath). The antennas used here are replicas of the helical antennas used by Zimmerman [Zimmerman and Cannon Jr., 1995], with an additional impedance matching microwave circuit added to increase antenna efficiency. The antennas are constructed of standard materials that can be bought at any hardware store. The top section of Fig. 4.6 shows the transmit hardware used for this project. All of this hardware was designed and built by graduate students at Stanford.

Finally, the pseudolites are mounted such that they are broadly and evenly distributed in the “sky” to provide favorable signal geometry and are pointed toward the structure below. One of the pseudolites (referred to here as the master pseudolite) was modified to broadcast a data message that is used for coarse synchronization of our GPS receivers (see [Zimmerman, 1996]).

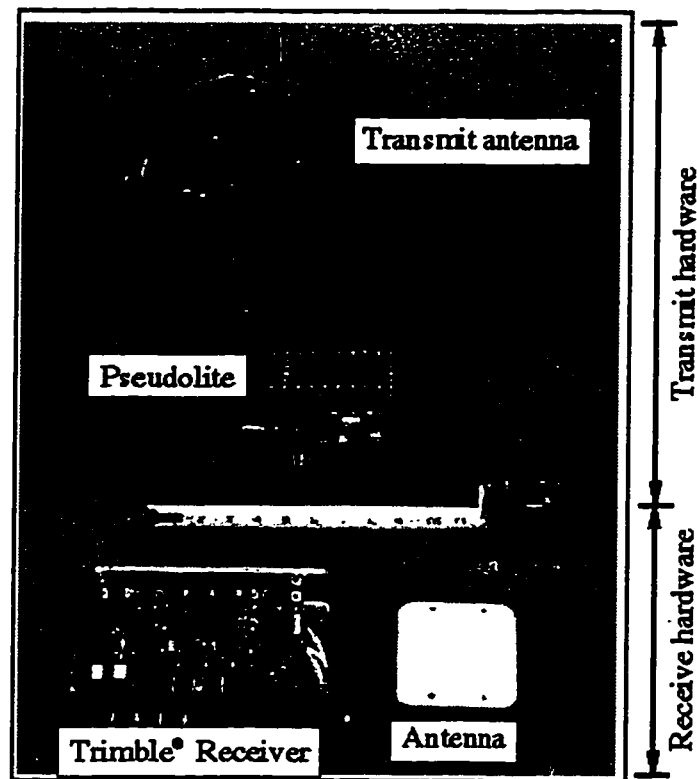


Figure 4.6: Transmit and Receiver Hardware

This photograph shows the GPS transmit and receive hardware used for this research. All of the transmit hardware was designed and built at Stanford. The receive hardware was provided by Trimble Navigation. The core code of the receiver was modified by me and by other students in the Stanford GPS lab for our experimental needs.

Receivers

The pseudolite signals are received at antennas mounted on the experimental structure. Two hemispherical GPS patch antennas are mounted to each rigid body for a total of six antennas (a seventh antenna is also on a static stand in the lab and was used for calibration and testing but is not essential to system operation). Two 4-antenna Trimble TANS Quadrex® receivers measure the pseudolite signals and output DCP measurements at 10 Hz. The receiver core code is modified at the signal processing level to suit the experiment requirements (e.g. to receive the pseudolite signals). The signal from one of the antennas on the structure is split and runs to both receivers. Each receiver synchronizes

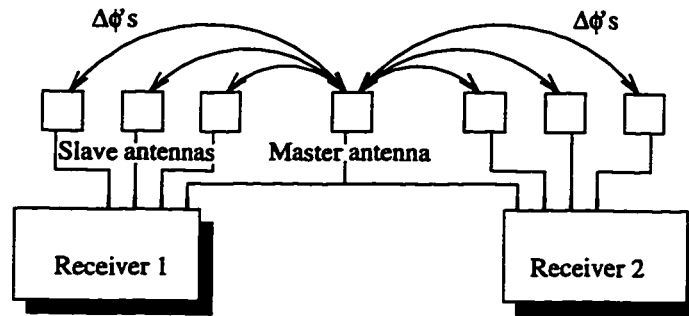


Figure 4.7: Antenna Receiver Connection Diagram

Two receivers (four antennas each) were used simultaneously for this research. To prevent errors due to timing, phases are differenced only between antennas connected to the same receiver and thus the same clock reference. The common master antenna aids coarse synchronization of the receivers to the master pseudolite data message.

its data collection and output to the data message sent by the master pseudolite. While two receivers are used, carrier phase measurements are differenced only between antennas connected to the same receiver. As shown in Appendix A, this technique eliminates some potential timing errors. Fig. 4.7 shows a diagram of the receiver/antenna connection.

The resulting GPS sensing system consists of an array of interconnected antennas that provide enough information to resolve the overall motion with sufficient bandwidth and deflection sensitivity for control. The DCP measurement available to these antennas is discussed further in Chapter 2, and techniques of resolving the motion of the structure given these measurements are discussed in Chapter 7. See Table 4.1 at the end of this chapter for a list of some characteristics of the GPS sensor system.

4.2.2 Rate Gyroscopes

In addition to the GPS sensors, six inexpensive rate gyroscopes (see Table 4.1 for specifications) were mounted on the test structure, primarily to provide an independent measurement with which to compare the GPS results. It is possible to take advantage of the good high frequency performance of the gyros to enhance the state estimates [Montgomery *et al.*, 1994], but this was not the primary focus of this work.

The gyros are mounted to the arms of the rigid sections, three on the center section, two

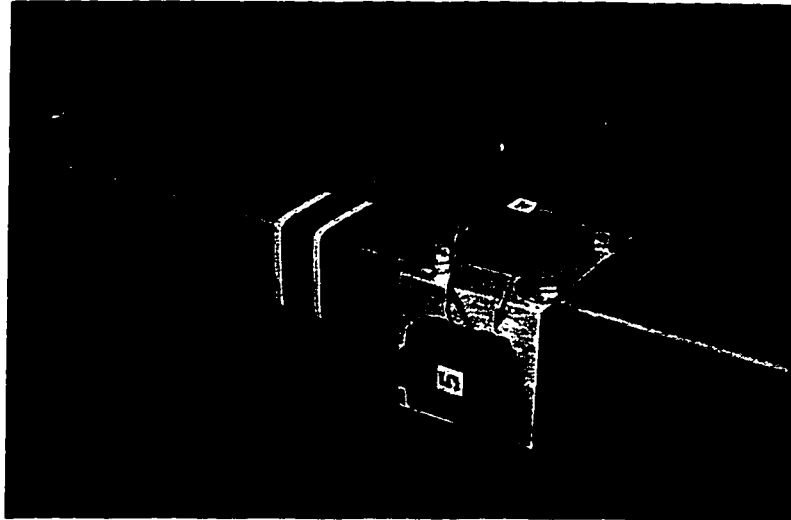


Figure 4.8: Mounted Rate Gyroscopes

Two rate gyroscopes are shown mounted to an arm. The lower gyro measures rotation rates parallel to the arm. The other gyro measures rates orthogonal to the arm in the horizontal plane.

on one of the outer sections, and one on the third section. Fig. 4.8 is a picture of a pair of gyros mounted to an arm. Orientation of a rigid section can be found by simply integrating the signals from the gyroscopes. A calibration of the gyros was performed to find the gyro offsets and to minimize inherent drift errors from these inertial sensors. However, even with calibration prior to each experimental session, the gyro drift is non-negligible, even for the relatively short duration experiments (1-2 minutes). This points out an important advantage to GPS sensing over inertial sensing: DC performance. GPS and gyroscope measurements are compared in Chapters 7 and 8. Table 4.1 lists some properties of the rate gyros.

4.3 The Actuators

A system of 24 on/off cold gas thrusters is used to impart forces on the test structure. These thrusters are used for control actuation and for disturbance input in the control experimentation described in this thesis (see Chapter 8). Each thruster valve can be opened or closed by the real-time computer through a digital interface card. Fig. 4.9 shows a block

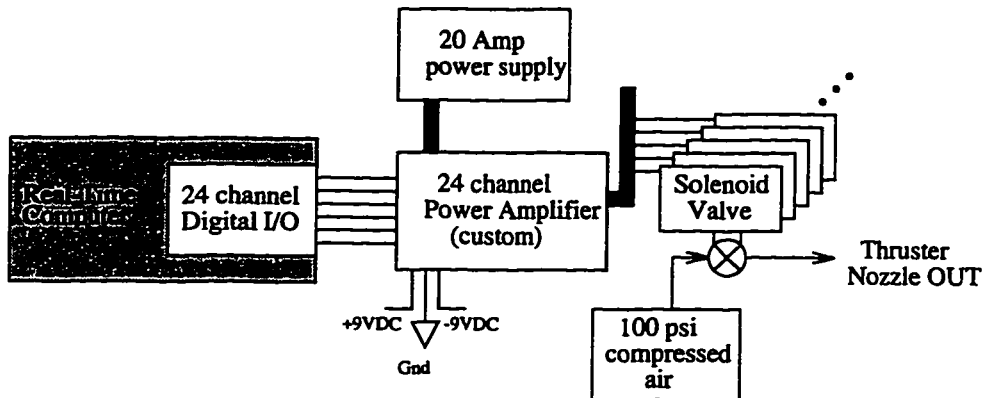


Figure 4.9: Actuation System Diagram

This diagram shows the operation of the thrusters by computer command. The computer can open and close each thruster valve independently at 100 Hz.

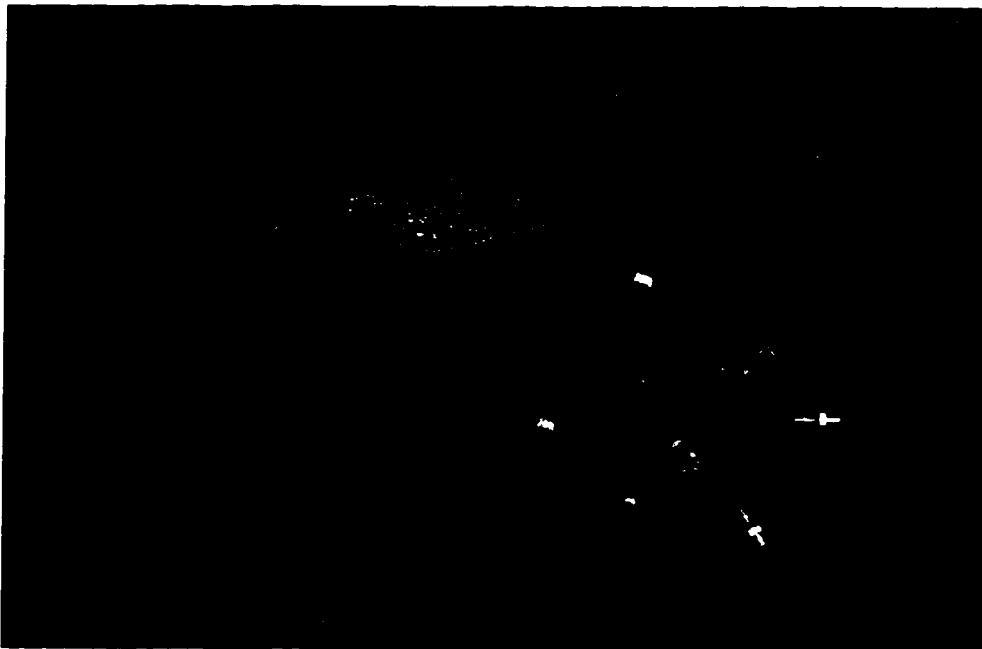


Figure 4.10: Thruster Cluster

A cluster of four thrusters is shown at an arm endpoint. Given a cluster at each arm endpoint, all important motions of the overall system can be controlled.

diagram of the actuator system. The computer sends a signal for each thruster valve to a 24 channel power amplifier, which creates the 0.9 amp current required to operate the valve. When a valve is opened, it allows high pressure compressed air to flow through a nozzle mounted on the structure. A cluster of four thrusters is mounted at the end of each arm. Fig. 4.10 is a picture of one of the clusters. See Table 4.1 for some properties of the thrusters.

Since control algorithms typically output control commands that are real valued, and since gas jets are positive definite, the nozzles for jets of this type are sometimes mounted in directly opposing pairs. An opposing pair nozzle configuration allows a negative command to be realized by simply firing the opposing jet. Note the orientation of the nozzles in the picture (Fig. 4.10). Given an axis along the centerline of the arm, each of the four nozzles is oriented 45° from the axis and is in either the vertical or horizontal plane through the axis. The nozzles for this experiment are *not* mounted in opposing pairs chiefly because requiring opposing thrusters necessitates additional thrusters. However, even without opposing pairs of thrusters, the 45° cluster configuration at each arm endpoint allows control of all the important modes of structural motion.

Fig. 4.11 shows the important forces and torques on a rigid section needed to control the primary system modes (see Fig 6.3 for a picture of the primary system modes). The six important forces/torques include forces in the y -direction and torques in the x and z -directions. As an example, the *second bending mode* shown as the 6th mode in Fig 6.3 can be actuated using the z -axis torques ($+T_z$ and $-T_z$). An advantage of the 45° cluster configuration is the high translation forces attainable due to the use of four thrusters simultaneously ($+F_y$ and $-F_y$ in Fig. 4.11). This is an advantage because the rigid sections have much more translational inertia than rotational inertia. Also, higher translation forces translate to faster slew maneuvers because rotation of the entire system in the horizontal plane is actuated primarily¹ with translation forces on the outer two rigid sections.

These actuators were chosen because they are simple and inexpensive. Their main disadvantage is that they are fundamentally limited to two states – on and off. While computed

¹A small z -axis torque on the center rigid section is also required.

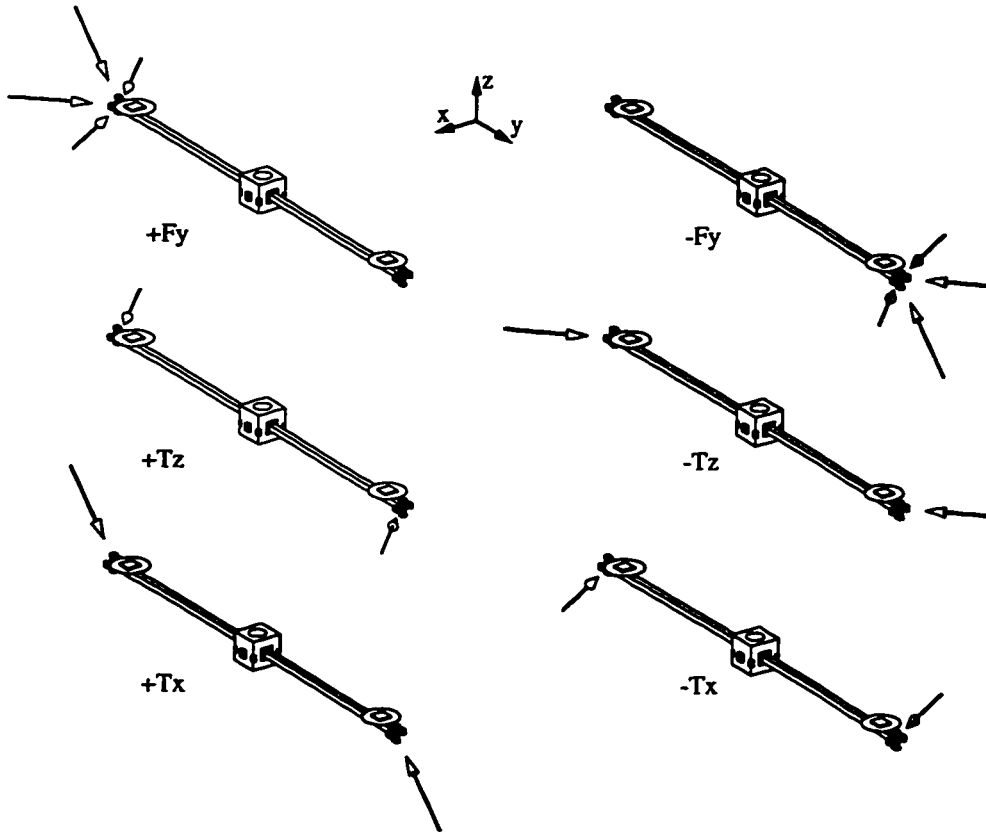


Figure 4.11: Thruster Configuration

Control of the important structural modes requires primarily the six forces/torques on each rigid section as shown. $+F_y$ denotes a force in the positive y -direction, for example, and $-T_z$ denotes a negative torque about the z -axis.

control commands are generally continuous-valued, and thus not directly realizable with a on/off actuator, it is possible to approximate a force that is less than the thruster maximum capacity by pulsing a thruster rapidly. Some of the details of this technique as applied to this work are shown in Section 8.2.

4.4 Preliminary Sensor Data Analysis

One of the first steps after completion of the physical system construction and sensor installation was a preliminary sensor test. First, the structure was lifted from its support

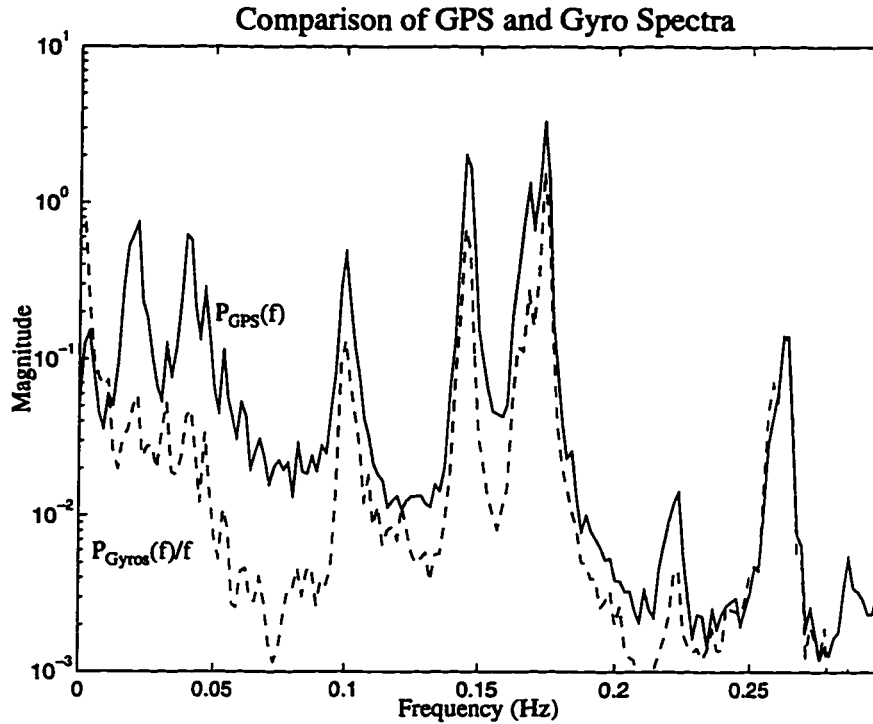


Figure 4.12: Free Motion Sensor Spectra

This plot shows power spectral densities of GPS and gyroscope data taken during free motion of the flexible structure. The presence of clear, coincident, resonant peaks is a preliminary sensor validation.

tables, and balanced. Then, random excitation was applied (manually) in an attempt to introduce energy into the primary system vibration modes. GPS DCP data and rate gyroscope data was taken during this random free motion of the flexible structure. To analyze the sensor data and to compare the GPS and gyroscope information, the power spectral density was computed for each sensor. Fig. 4.12 shows a comparison of these two spectra. The gyroscope spectrum is divided by frequency to allow one-to-one frequency domain comparison of its rate measurements with the position measurements from GPS. Modal behavior is shown by the clear resonance peaks,² and the agreement of the peak frequencies between the GPS and gyroscope data is apparent. These preliminary results

²This data was collected before the final system hardware assembly. As a result, the mode frequencies in Fig. 4.12 do not agree with the final model presented in Chapter 6.

clearly show that GPS can be used to sense the flexible vibrations of the test structure.

Differences in the spectral magnitudes between the two sensors illuminate their different observability characteristics. A notable contrast is the lack of low frequency modes in the gyroscope data. This could be caused by the poor low frequency performance of the imperfect inertial sensor or by the unobservability of some modes (such as modes involving predominantly rigid-body translation) from rate gyroscope measurements.

4.5 Summary

To test the applicability of GPS for flexible structure sensing for control, an experimental apparatus was built consisting of a flexible structure, a set of actuators to impart forces on the structure, and a set of sensors to measure the motion. The structure moves like a large flexible platform in space, with low vibration frequencies and low damping, and thus is an ideal candidate for real-time control studies using GPS for motion sensing.

	Parameter	SI	English
Full Assembly	Length	8.1 m	26.5 ft
	Arm span	3.94 m	12.9 ft
	Mass	183.1 kg	402.8 lb
Rigid Section	Cube material	Aluminum 6061T6	
	Arm material	2 inch Square Steel Tubing	
	Cube edge length	25.4 cm	10 in
	Mass	60.9 kg	134 lb
	I_{xx}^a	42.5 kg·m ²	207.8 lb·ft ²
	I_{yy}^a	0.478 kg·m ²	2.34 lb·ft ²
	I_{zz}^a	43.1 kg·m ²	210.8 lb·ft ²
Elastic Beam	Material	Aluminum 6061T6 Circular Tubing	
	Length	3.66 m	12 ft
	Diameter	12.7 mm	0.5 in
	Wall thickness	0.89 mm	0.035 in
Suspension Threads	Material	Symmetric Braid Vectran [®]	
	Length	13.7 m	44.8 ft
	Cross-section	1.36 mm	0.0535 in
	Tensile strength	2005 N	450 lb
Actuation System	System design	24 On/Off Cold-Gas Thrusters	
	Max thruster cycle rate	100 Hz	
	Air pressure	690 kPa	100 psi
	Thruster mass (per jet) ^b	0.5 kg	1.1 lb
	Thruster force (per jet)	1.4 N	0.31 lbf
GPS Sensors	Signal source	6 custom pseudolite transmitters ^c	
	Antennas	6 Trimble patch antennas	
	Antenna mass	191 g	6.7 oz
	Receivers	2 Trimble Quadrex	
	Data type	Common clock differential carrier phase (DCP)	
	Data rate	10 Hz	
	Measurements	5 baselines, 6 signals = 30 measurements	
Rate Gyros	Type	Murata single axis	
	Mass	41 g	1.5 oz
	Max rate	±1.40 rad/s	±80 deg/s
	Drift rate: Published Measured ^d	0.157 rad/s 0.017 rad/s	9 deg/s 1 deg/s

^aMoments of inertia are in the principle coordinate system, shown in Fig. 4.5

^bIncludes solenoid valve, fittings and nozzle.

^cThe signal from one transmitter contains a data message used for receiver coarse synchronization.

^dStatic test. After static calibration.

Table 4.1: Experimental System Characteristics

This table lists some of the most critical characteristics of the flexible structure experimental hardware.

CHAPTER 5

Software Systems Architecture

This chapter describes the design of the real-time code architecture used for this research. The block diagram shown in Fig. 1.4 in the introduction is separated into two main components, the *structure* and the *computer*. Up to this point, the structure and its subsystems have been explained in some detail. We can now focus on the computer. This chapter explains the software framework in which the estimator and controller algorithms (Chapters 7 and 8) are implemented. Because the system being controlled is complicated and task execution is time critical, a powerful and flexible real-time computing environment is required for reliable performance and ease of debugging. This chapter describes the final system setup and shows an example of the control loop from a computer operating system perspective.

5.1 Real-Time Processing Design

When using a computer to close a control loop, issues of timing can be very important. This is especially true when 1) tasks such as input and output happen rapidly, 2) the processor is fully loaded during closed-loop operation, and 3) input and output timing is critical. All three of these conditions are true for this project. For example, logging of data must not jeopardize the timely output of control commands. For these reasons, a real-time operating system was chosen that allows millisecond level control of the execution of specific tasks in the computer and allows tasks to be prioritized. Further, software was obtained that

allows microsecond level post-execution analysis of task execution timing — an invaluable debugging tool.

Specifically, real-time data collection, processing, and control implementation are performed on a Pentium Pro 200 computer running LynxOS[®] Version 2.4.0 from Lynx Real-Time Systems[®] [LynxOS, 1995]. The code was written in a multi-threaded, priority-based framework conforming to POSIX real-time standards [Gallmeister, 1995].

Fig. 5.1 illustrates the main components of the real-time code. Each of the shaded boxes represents a thread of execution. A “thread of execution” is an independent set of executable instructions in memory. The threads have access to a common area of data memory, and the operating system decides which thread currently resides in the processor. This decision is aided by constructs¹ that a programmer can use to ensure logically correct execution, e.g. that data is new before it is used.

At the lowest processing level, a thread waits for individual bytes to become available at each of the two serial ports. Each port receives approximately 500 bytes of information per second and buffers the data. When a full serial packet (as defined by the receiver serial interface) is received, the thread extracts the pertinent information (primarily differential carrier phases) and places the new data in global memory space. This data is then marked as “new.”

This phase data is then ready for real-time processing. A high-level thread that handles state estimation and control computation notes the presence of new data, reads the data, and marks the global data “old.” The new data is then used to estimate the configuration and motion states of the plant (the physical structure), and control commands are computed based on the difference between the actual and the desired states.

For post-processing analysis and debugging, a data logging thread stores the raw data and/or the processed data to disk. Due to the inconsistent nature of disk access (caused by other needs of the operating system, periodic head sweeps, etc.) an asynchronous data logging package was developed that double buffers data, and writes to disk only when the

¹Mutexs, semaphores, condition variables, priorities etc. — for readers familiar with real-time programming.

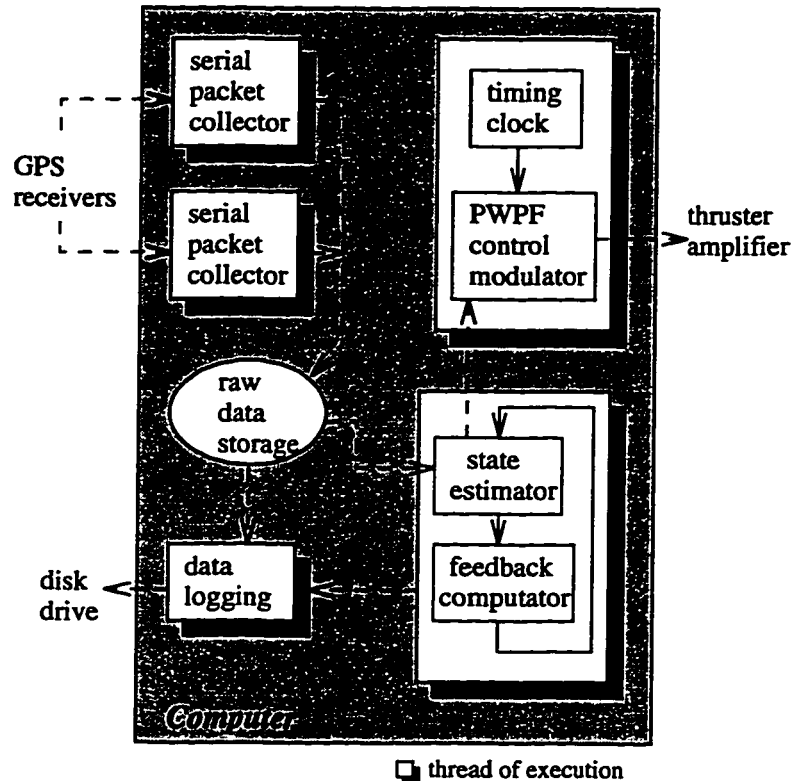


Figure 5.1: Real-Time Processing Setup

This diagram shows the primary execution threads (shaded boxes) and their interaction during real-time operation.

processor is free from the more time critical tasks. This technique was found to be the most efficient and reliable way to store data in real-time.

Finally, a low-level thread PWPF modulates (Section 8.2) the control commands and pulses the thrusters accordingly (through a digital I/O card as shown in Fig. 4.9) to complete the control loop.

5.2 Analysis of Task Execution Timing

Fig. 5.2 shows an example screen-shot of the Timescan[®] timing analysis program. To create this figure, the programmer inserts function calls throughout an application that are called “event logs.” Execution of the code then produces an event log file that can be loaded

by Timescan®. The result is a method of observing the timing of code execution to the microsecond level in post processing, a crucial tool for code debugging.

The figure shows eight threads (labeled “process traces”), numbered one through eight. This screen-shot is an example of the real-time code at its busiest. All data is being displayed to the screen and dumped to disk, and all of the functionality of the code is being exploited. Here is a description of the role of each thread shown. The labels in the following list refer to thread numbers.

- 1: This is the primary feedback loop thread. When new data is available (from threads 7 and 8), this thread begins. First, the gyroscope data are read and processed. Next, the gyro data and raw GPS phase data are displayed to the screen. The next task is the primary processing load, state estimation. Next, control commands based on the new state estimates are computed. The thread finishes its cycle by displaying the new data and sending all of the data to buffers ready to be written to disk when the processor is available.
- 2,3,4,5: These threads handle the dumping of data to disk (one thread for each of four output files). Because data storage is not time critical, these threads run with low priority. Only one disk writing event is shown in the time interval displayed.
- 6: This thread controls the thruster valves directly. This is a time critical task that runs at high priority. Each time the thread is serviced (occurs at 100 Hz), all 24 thruster valves are opened or closed (or left alone) according to the control commands computed in thread 1.
- 7,8: These threads monitor the serial ports that are connected to the GPS receivers (one port/thread per receiver). When a packet of data arrives (10 Hz), the data is extracted and written to memory in a format for use by thread 1.

The prioritized, multi-threaded code design produces a final application that runs smoothly and efficiently. All tasks for the feedback loop are completed in each 100 millisecond cycle period, and the high priority tasks of input and output are handled in a timely fashion.

Fig. 5.2 makes it clear that the majority of processor time is dedicated to the state estimation algorithm. The combination of a complicated physical system (18th order model) and many measurements (36) results in a large matrix computation that takes place every measurement cycle. While more efficient computation was not required for this research,

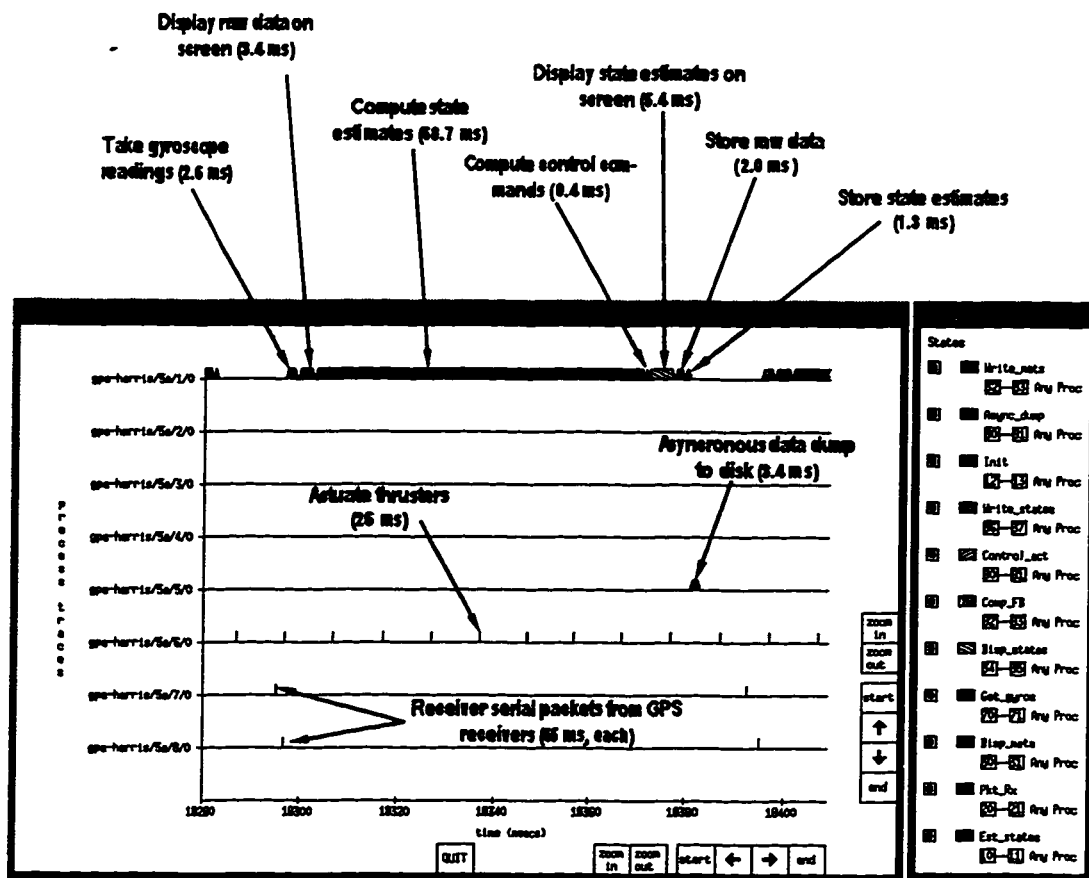


Figure 5.2: Timescan® Screen Shot

This figure shows an example screen produced by the Timescan® analysis program, which was used to find timing discrepancies and inefficiencies during code development.

larger systems with more states and measurements may benefit from development of more efficient algorithms. This is a suggested area for future research.

5.3 Summary

It is very likely that any builder/designer of a digital real-time control system will spend a large amount of time with the details of the software setup. While the heart of a control system is often the theory and mathematical algorithms, timely data collection, processing

and control output are also essential. This project makes use of a real-time operating system that supports multiple prioritized threads and has tools for post-processing analysis of thread execution timing. Coding within this framework is intuitive and well-suited for debugging.

CHAPTER 6

Physical System Modeling

This chapter presents the approach and results of modeling the flexible structure system. Chapters 3, 7 and 8 require a model of system dynamics and measurement kinematics. The objective is to find matrices $A, B, B_w, H(\hat{x})$ and vector $h(\hat{x})$ in the following equations:

$$x_{k+1} = Ax_k + Bu_k + B_w w_k \quad (6.1)$$

$$y = h(x) + \beta + \nu \quad (6.2)$$

$$\cong H(\hat{x})\delta x + h(\hat{x}) + \beta \quad (6.3)$$

$$\text{with,} \quad x = \hat{x} + \delta x \quad (6.4)$$

These equations are the same as (2.6–2.10) and (3.25) in Chapters 2 and 3. This chapter addresses the following main topics:

- Definition of the quantities used to define the motion of the system: state variables and generalized coordinates.
- Development of the models for free and forced motion (Eq. 6.1).
- Formulation of the relationship between states and measurements and a computational technique to re-linearize this relationship in real-time (Eq. 6.3).

Before writing model equations, it is necessary to define parameters that describe the configuration and motion of the system under investigation. These parameters are represented by the state vector, x .

C_1, C_2, C_3	Names of the three rigid body sections in the assembly. Also refers to frames fixed to the respective rigid bodies.
C_1^*, C_2^*, C_3^*	Points corresponding to the center of mass locations of rigid bodies C_1, C_2 , and C_3 .
B	The “body frame.” Reference frame about which equations are linearized.
N	The “Newtonian frame.” A frame fixed in the lab.
$\underline{b}_1, \underline{b}_2, \underline{b}_3$	Orthonormal unit vectors fixed in B .
q_1, q_4, q_7	Generalized coordinates describing the translation of bodies C_1, C_2 , and C_3 respectively in the \underline{b}_2 direction.
q_2, q_5, q_8	Generalized coordinates describing the rotation of bodies C_1, C_2 , and C_3 respectively about the \underline{b}_1 unit vector.
q_3, q_6, q_9	Generalized coordinates describing the rotation of bodies C_1, C_2 , and C_3 respectively about the \underline{b}_3 unit vector.
N^*	A reference point fixed in N .
q_{10}	A generalized coordinate describing the rotation of the B frame with respect to the N frame about the \underline{b}_3 unit vector.

Table 6.1: Definitions of Key Parameters

This table contains some brief descriptions of the parameters used to describe the configuration and motion of the flexible structure physical system. These parameters are illustrated in Fig. 6.1.

6.1 Generalized Coordinates

Eqs. 6.1–6.4 are all in terms of the state vector, x . But before defining the state, it is necessary to describe the motion of the physical system in terms of generalized coordinates. For the flexible structure system, it is easiest to assign generalized coordinates to translations and rotations of the rigid bodies (denoted C_1, C_2 , and C_3) of the system. Then, the state can be defined in terms of the generalized coordinates such that the equations of motion are easy to express and propagate (see Section 6.2.2). The generalized coordinates and some useful bodies and frames are shown in Fig. 6.1. Table 6.1 summarizes definitions of the coordinates and the frames shown in the figure.

Reference frames

A reference frame, N ,¹ is defined that is fixed in the laboratory. Further, the point N^* is a point fixed in N that coincides with the center of mass of body C_2 (C_2^*) when the entire

¹ N for Newtonian. A “Newtonian frame” is a frame in which Newton’s laws are assumed to correctly describe the motion of particles and bodies.

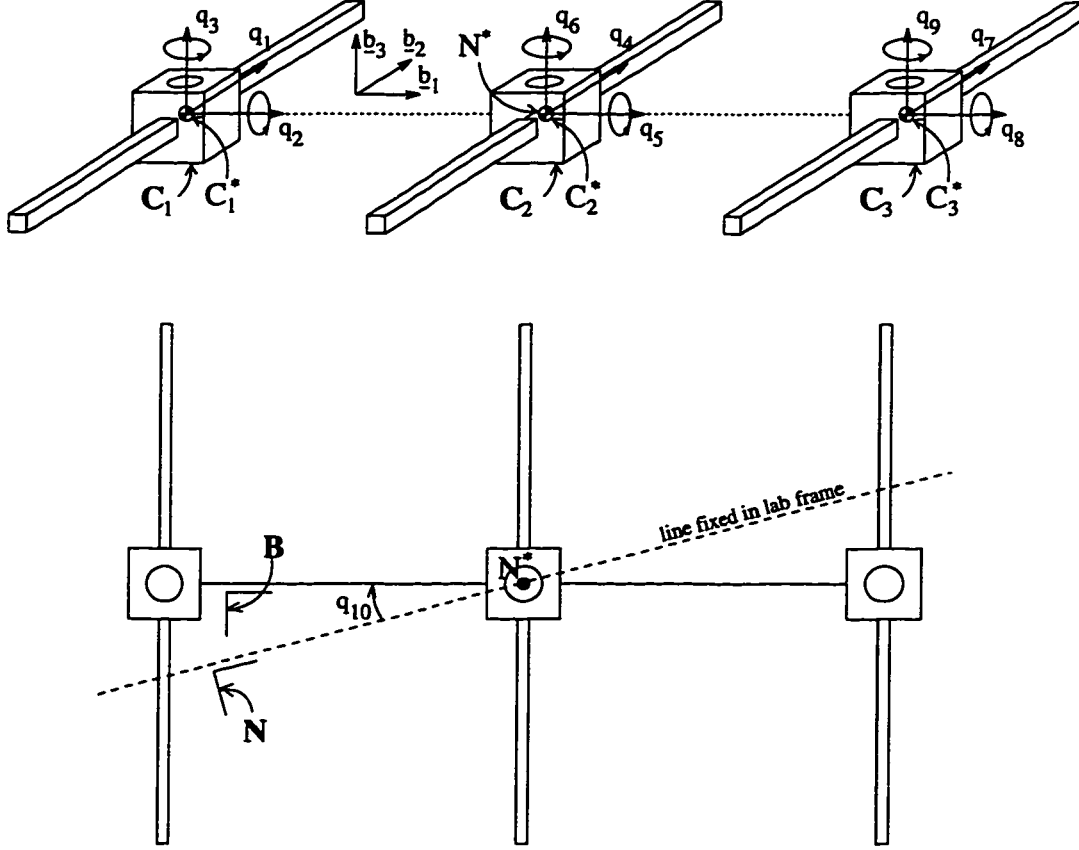


Figure 6.1: Generalized Coordinates

This figure illustrates the definitions of the generalized coordinates and some useful points and frames. The notation used is discussed in Table 6.1

system is at rest. Let \mathbf{B} denote a frame that is free to rotate about an axis that passes through N^* and is parallel to \underline{b}_3 , and let \underline{b}_1 , \underline{b}_2 , and \underline{b}_3 define an orthonormal dextral set of unit vectors fixed in \mathbf{B} (\underline{b}_3 points “up” in the laboratory).

Elastic motion

Generalized coordinates q_1 – q_9 define the motion of the system in \mathbf{B} . These correspond to the so-called “elastic motion” and are characterized by small perturbations, or deformations, of the structure about its undeformed (rigid-body) state. For example, q_1 is the translation of C_1 in the horizontal plane, in the \underline{b}_2 direction, and q_2 and q_3 are rotations of C_1 about \underline{b}_1 and \underline{b}_3 , respectively. Coordinates q_4 – q_9 similarly define the motion of C_2 and C_3 in \mathbf{B}

(see Fig. 6.1). These motions are assumed small, and all equations are assumed linear in q_1 – q_9 . Thus, the order of rotations is not important.²

While six coordinates are required to define the motion of a rigid body in general, only three were used for this work. The additional degrees of freedom (e.g. translation in the \underline{b}_1 and \underline{b}_3 directions) are not critical for typical motions of the system, and are left out in the interest of computational efficiency. The primary modes of motion that are included in the final model (see Section 6.2) do not require the additional parameters and are specified completely by q_1 – q_9 .

“Rigid-body” motion

The generalized coordinate, q_{10} , defines the angular rotation of \mathbf{B} in \mathbf{N} . This defines the so-called rigid-body motion of the system. Because a goal of this research is to control large angle rotational slew maneuvers of the structure in the horizontal plane, q_{10} is not assumed to be small.

An interesting topic in the literature of flexible body dynamics involves the definition of the “unstressed or rigid-body configuration” of a system. If the full non-linear equations of motion of an unrestrained flexible system are written, this unstressed configuration is entirely arbitrary [Kane and Levinson, 1980]. However, there are significant computational advantages to finding a frame about which the elastic motions are small, and about which equations may be linearized. A problem with this technique arises when errors in the rigid-body mode parameters are large, resulting in an invalid linearization.

This points out an important advantage of GPS over inertial sensors for flexible body sensing. While biases in rigid body position and rotation can be unobservable with inertial sensors alone, distributed antenna GPS can provide unbiased estimates of rigid-body motion and elastic motion simultaneously (as will be demonstrated in Section 7.3.3 of this thesis).

²In general, the orientation of a rigid body in a frame can be defined by successive rotations, where rotation order is important, i.e. Euler angles.

6.2 Dynamic Modeling

This section contains the derivations of the equations of free and forced motion of the flexible structure system. First, the equations of motion are developed without process noise terms ($B_w w_k$ in Eq. 6.1). A process noise model will be added in Section 6.2.5.

6.2.1 Equations of Motion

It is possible to write a standard second order linear differential equation describing the variation of q with time:

$$\ddot{q} = \Phi q + \Psi \dot{q} + \Upsilon u \quad (6.5)$$

where,

Φ - Stiffness matrix

Ψ - Damping matrix

Υ - Forcing matrix

u - Vector of forcing terms

This equation relies on a key assumption about the rigid-body motion (q_{10}). It is assumed that while q_{10} is not small, its derivatives, \dot{q}_{10} and \ddot{q}_{10} (rigid-body rotation rate and acceleration), are well approximated as small. Hence, the equations are linear in q_{10} , and any coupling³ between the rigid-body motion (q_{10}) and the elastic motion (q_1 - q_9) may be neglected.

It is convenient to decouple these equations into "modal form" with the modal transformation matrix, U :

$$q = U\xi \quad (6.6)$$

where,

ξ - Vector of modal coordinates

U - The modal matrix. The columns of U are the mode vectors.

³Such coupling is sometimes called "centrifugal stiffening" since rotation tends to increase modal frequencies.

The mode matrix, U , is an orthonormal matrix ($I = U^T U$), that diagonalizes Φ ,

$$\Lambda = U^T \Phi U, \quad \Lambda \text{ diagonal.} \quad (6.7)$$

It is also assumed that U diagonalizes Ψ . This is a necessary assumption to find uncoupled equations with damping. Since the damping in the flexible structure system is very light, the errors contributed by this assumption are not significant. This assumption is equivalent to using the concept of modal damping, which is often used for analytic models of flexible structures since the true damping mechanisms are difficult to determine and express in a linear model.

$$C = U^T \Psi U, \quad C \text{ diagonal.} \quad (6.8)$$

Now, it is possible to write second order uncoupled differential equations in ξ ,

$$\ddot{\xi} \stackrel{(6.5-6.8)}{=} \Lambda \xi + C \dot{\xi} + U^T \Upsilon u \quad (6.9)$$

6.2.2 Definition of the State Vector

To transform Eq. 6.9 into state space form (first order), let

$$x = \begin{bmatrix} \xi \\ \dot{\xi} \end{bmatrix} \quad (6.10)$$

then,

$$\begin{bmatrix} \dot{\xi} \\ \ddot{\xi} \end{bmatrix} \stackrel{(6.9)}{=} \begin{bmatrix} 0 & I \\ \Lambda & C \end{bmatrix} \begin{bmatrix} \xi \\ \dot{\xi} \end{bmatrix} + \begin{bmatrix} 0 \\ U^T \Upsilon \end{bmatrix} u \quad (6.11)$$

$$\dot{x} \stackrel{(6.10, 6.11)}{=} A_c x + B_c u \quad (6.12)$$

with,

$$A_c = \begin{bmatrix} 0 & I \\ \Lambda & C \end{bmatrix}, \quad B_c = \begin{bmatrix} 0 \\ U^T \Upsilon \end{bmatrix} \quad (6.13)$$

Now, to arrive at the desired form stated in Eq. 6.1, convert to discrete form using the zero-order-hold approximation on the inputs [Franklin *et al.*, 1990] and with sampling period T , as follows:

$$A = e^{A_c T}, \quad B = \int_0^T e^{A_c \eta} d\eta B_c \quad (6.14)$$

Now, the state is defined (Eqs. 6.6 and 6.10) and state-space equations of motion are formulated (Eqs. 6.1 and 6.14). The next step is to find the mode matrix (U), the mode frequencies (Λ), and the mode damping (C).

6.2.3 Finding the Modal Transformation

Harmonic motion, Λ and U

To find the mode matrix and mode frequencies (Λ and U in Eq. 6.5), a model of the flexible structure was constructed for analysis with the finite element computer package, MSC/NASTRAN®. Computing facilities at NASA/Ames Research Center were used for this task.⁴ The structure was divided into elements as shown in Fig. 6.2. The elastic beams were divided into eight elements each, and the suspension threads were modeled as a single elastic rod. The arms were assumed to be rigid. Appendix D shows the final NASTRAN® input file.

The input to the finite element package is the mass, inertia, and elasticity properties of the system elements, and the output is a set of modes, each of which includes a frequency of vibration and the associated set of nodal displacements. To reduce computational load for real-time processing, only nine of the lowest frequency modes are retained in the final model. Eight of these modes are shown graphically in Fig 6.3 (the ninth mode is the rigid-body mode – horizontal plane rotation of the entire assembly). The first two modes in the figure are the suspension-induced modes. These two modes (as well as the rigid-body mode) do not bend or twist the elastic beams.

⁴The help of Mladen Chargin and Roy Hampton at NASA/Ames is gratefully acknowledged.

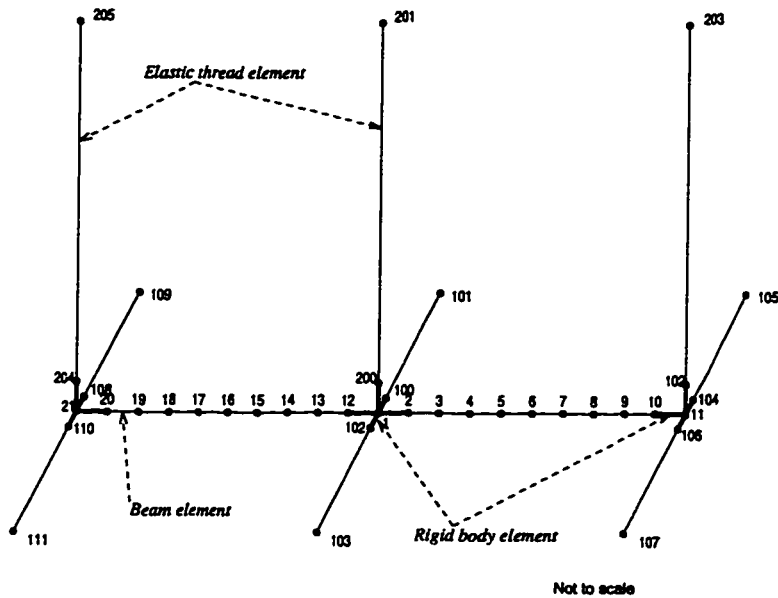


Figure 6.2: Finite Element Structural Grid

This is the finite element grid used to model the flexible structure. The node points are numbered and the element types indicated.

Modes 3–8 are the elastic modes, modes that *do* bend or twist the elastic beams. Consistent with Tables 6.2 and 6.3, modes 3, 6, 7 and 8 are called the first, second, third, and fourth bending modes, respectively, and modes 4 and 5 are called the first and second twist modes.

The predicted modes agree qualitatively with the motions observed during testing of the structure's free motion. However, the frequencies were observed to differ from experimental results by as much as 50%. This can be attributed to the uncertainty in determining some input parameters (such as the suspension thread attachment point) and unmodeled suspension beam dynamics. To obtain the best possible finite element based model, analytically determined mode shapes were combined with the experimentally determined frequencies. A series of tests were performed to find the modal frequencies. Each mode predicted by the finite element analysis was excited manually, and data from the GPS sensors were collected. A power spectral density plot was computed from the collected data. The mode frequency

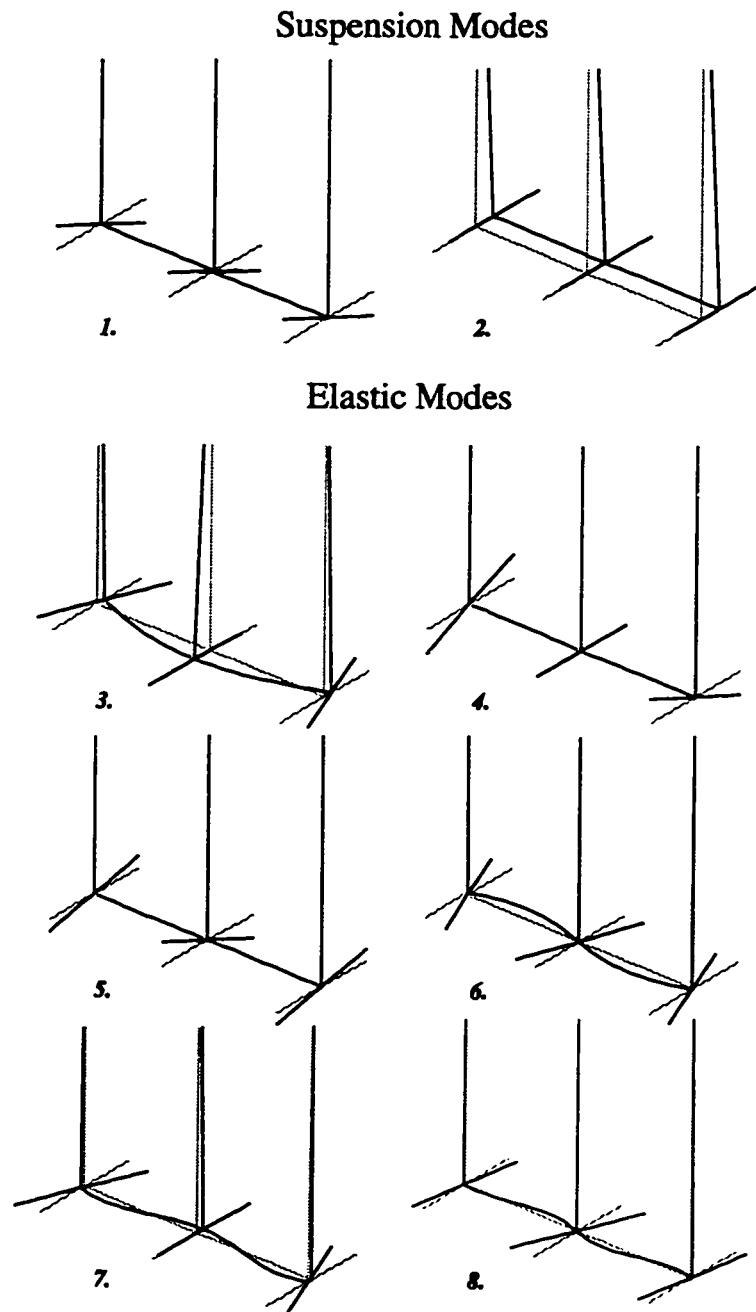


Figure 6.3: Modes

This figure shows the eight primary modes predicted by finite element analysis that were retained in the final reduced-order model. Two suspension modes and six elastic modes are shown. The rigid-body mode (horizontal plane rotation) is not shown.

Mode number	Description	Frequency (Hz)
1	Pendulum mode	0.0594
2	Swing mode	0.1596
3	First bending mode	0.1321
4	First twist mode	0.0852
5	Second twist mode	0.1377
6	Second bending mode	0.1349
7	Third bending mode	0.2302
8	Fourth bending mode	0.2781
9	Rigid body mode	0.0000

Table 6.2: Modal Characteristics

This table lists the final model mode frequencies. These modes correspond to the mode shapes in Fig. 6.3

was assigned by locating the peak in the power spectrum. The experimentally determined frequencies are given in Table 6.2.

These frequencies enter the model by setting the diagonal elements of Λ as follows:

$$(\Lambda)_{ii} = -w_n^2 \quad (6.15)$$

where i is the mode index and w_n is in radians per second.

Further model studies using input/output system identification would be interesting here, and this is a proposed area for future research. Further modeling was not attempted for this dissertation due to the success of this simple model in the real-time experiments shown in Chapters 7 and 8.

Damping, C

The last step is to find the diagonal damping matrix C in Eq. 6.5. Damping is small for this structure and does not have a large effect on system motion, especially between 10 Hz estimator updates. Nevertheless, a crude damping model that was derived from experimental data was included for completeness.

It is standard to define the “time constant” of a damped harmonic vibration, τ , as the time for the amplitude of a vibration to reduce in magnitude by 63% ($0.63 = 1 - e^{-1}$). Time constants were estimated for each mode by collecting data during the damped free vibration

Mode	Description	τ (sec)	$\zeta = \frac{1}{\omega_n \tau}$
1	Pendulum mode	20	0.134
2	Swing mode	130	0.007
3	First bending mode	200	0.006
4	First twist mode	45	0.042
5	Second twist mode	35	0.033
6	Second bending mode	140	0.008
7	Third bending mode	50	0.014
8	Fourth bending mode	25	0.023
9	Rigid body mode	140	—

Table 6.3: Damping Time Constants

This table lists the modal damping time constants (τ) as determined from experiment. Also listed are the corresponding damping ratio values (ζ)

of each mode separately and estimating the time constant from this data. Table 6.3 contains the results of these tests. The damping enters the model by setting the diagonal elements of C as

$$(C)_{ii} = -2/\tau_i \quad (6.16)$$

where i is the mode index. Note that these values correspond to a very lightly damped system, as evidenced by the small damping ratios in Table 6.3.

6.2.4 Force Modeling

The force model describes how the thruster forces should be included in the equations of motion. The end result of this analysis is the matrix, B , in equation Eq. 6.1. This reduces, through Eqs. 6.13 and 6.14, to finding Υ in Eq. 6.5. A set of force and moment equations is written for each of the rigid sections independently, and finally, an equation of the entire assembly angular velocity is written to include the rigid-body rotation degree of freedom.

Specifically, for each rigid body, the standard Newton's Laws equations of rotation and

translation are formed as follows:

$$\underline{\mathfrak{M}} = \frac{N\partial}{\partial t} ({}^N\underline{H}^C) \quad (6.17)$$

$$\underline{\mathfrak{F}} = m \frac{N\partial^2}{\partial t^2} ({}^N\underline{p}^{C^*}) \quad (6.18)$$

$$\text{with, } {}^N\underline{H}^C = \underline{I} \cdot {}^N\underline{\omega}^C \quad (6.19)$$

where,

- $\underline{\mathfrak{M}}$ - The vector sum of all moments on C about its center of mass, C^* , due to thrusters
- $\underline{\mathfrak{F}}$ - The vector sum of all forces on C due to thrusters
- $\frac{N\partial}{\partial t}, \frac{N\partial^2}{\partial t^2}$ - Partial derivative and second derivative operator with respect to time of a vector in frame N
- m - The mass of C (see Table 4.1)
- \underline{I} - The principle axis moment of inertia tensor of C (see Table 4.1)
- ${}^N\underline{H}^C$ - The angular momentum of C in N
- ${}^N\underline{p}^{C^*}$ - The position vector to C^* (the center of mass position of C in N)
- ${}^N\underline{\omega}^C$ - The angular velocity of C in N

All of the rotational generalized coordinates ($q_2, q_3, q_5, q_6, q_8, q_9$, and q_{10}) are contained in ${}^N\underline{\omega}^C$, and the translation coordinates (q_1, q_4 , and q_7) are contained in ${}^N\underline{p}^{C^*}$.

To express the moments and forces ($\underline{\mathfrak{M}}$ and $\underline{\mathfrak{F}}$), define two vectors for each thruster, a position vector from the center of mass of the rigid body to a point on the line of action of the thruster, \underline{p}_i , and a unit vector along the line of action, \underline{f}_i . Fig. 6.4 shows an example of the geometry of these two vectors for one thruster. (See Fig. 4.11 for a more detailed view of the thruster geometry.) Thus, the moments and forces on a rigid body may be written

$$\underline{\mathfrak{M}} = \sum_i -\underline{p}_i u_i \times \underline{f}_i \quad (6.20)$$

$$\underline{\mathfrak{F}} = \sum_i -\underline{f}_i u_i \quad (6.21)$$

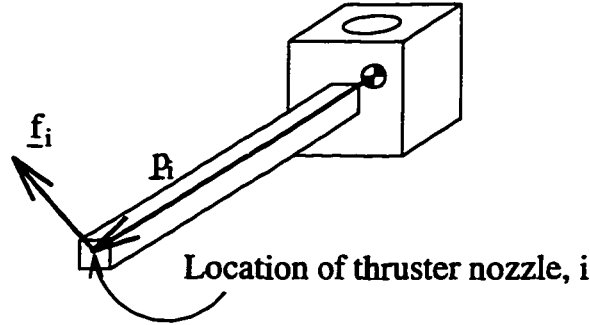


Figure 6.4: Thruster Vector Geometry Grid

Two vectors are defined for each thruster. The position of the thruster on the rigid-body, \underline{p}_i , and a unit vector in the direction of its thrust, \underline{f}_i . These two vectors are defined for all 24 thrusters.

where u_i is the magnitude of the force of thruster i , as well as an element of the input vector u in Eq. 6.5 (the minus signs are present in Eqs. 6.20 and 6.21 because the force on the rigid body is opposite the thrust direction).

The final equation of motion takes into account the rigid-body degree of freedom:

$$\underline{\mathcal{M}}_t = \frac{\partial}{\partial t} \left(\underline{I}_t \cdot N_{\omega}^B \right). \quad (6.22)$$

The subscript, t , indicates the total quantity for the entire structure (all three rigid sections, C_1 , C_2 , and C_3). It is assumed that the moment of inertia tensor, \underline{I}_t , is equal to the inertia of the undeformed structure.

Now it is possible to complete the force modeling by forming and linearizing Eqs. 6.17–6.22. These equations contain only the thrust magnitudes (u 's) and the second derivatives of the generalized coordinates (\ddot{q} 's). It is possible to now solve the equations for \ddot{q} and write the result in the form,

$$\ddot{q} = \Upsilon u \quad (6.23)$$

All of the algebraic manipulations including linearization of the equations were performed by the symbolic manipulator computer program Autolev®.

6.2.5 Process Noise Modeling

A model of process noise is an important part of the real-time recursive estimator (Chapter 7) and the bias estimator (Chapter 3). The primary goal of the process noise model is to affect the relative weighting between the model and the measurements in optimal state (and bias) estimators. The general process noise model developed here assumes that the noise enters as modal accelerations, so the portion of the state due to process noise is:

$$x_{k+1} = \begin{bmatrix} \dot{\xi} \\ \ddot{\xi} \end{bmatrix}_{k+1} = \begin{bmatrix} 0 \\ I \end{bmatrix} w_k = B_w w_k \quad (6.24)$$

Since there is really no significant process noise for the experimental system (such as vibration or wind) the process noise model is fictitious. However, the process noise cannot be neglected in an estimator, or the estimates will ignore the information from measurements. Any model error will then cause the estimator to diverge from truth (see [Franklin *et al.*, 1990], Section 9.5.1 for discussion). Since the process noise is fictitious, process noise magnitudes are difficult to assign *a priori*. For the experiments shown in this thesis, process noise magnitudes (Eqs. 3.30 and 7.1) were chosen to obtain the best estimator performance in practice.

This completes the formulation of the free and forced motion dynamic model summarized by Eq. 6.1. The equations are formulated by inserting Λ (Eq. 6.15), C (Eq. 6.16), Υ (Eq. 6.23), and U (columns are the modes in Fig 6.3) into Eqs. 6.13 and evaluating Eqs. 6.14 which gives the final A and B matrices in Eq. 6.1. B_w is from Eq. 6.24.

6.3 Measurement Kinematics

The goal of this section is the mathematical formulation of the position vectors⁵ from transmitters to antennas for the flexible structure system. In summary, the question of interest is “What are \underline{p}_{ji} (short for $\underline{p}^{T_j A_i}$) in Eq. 2.1?” To answer this, it is first necessary

⁵A position vector written in the form \underline{p}^{AB} is read “the position vector from point A to point B .”

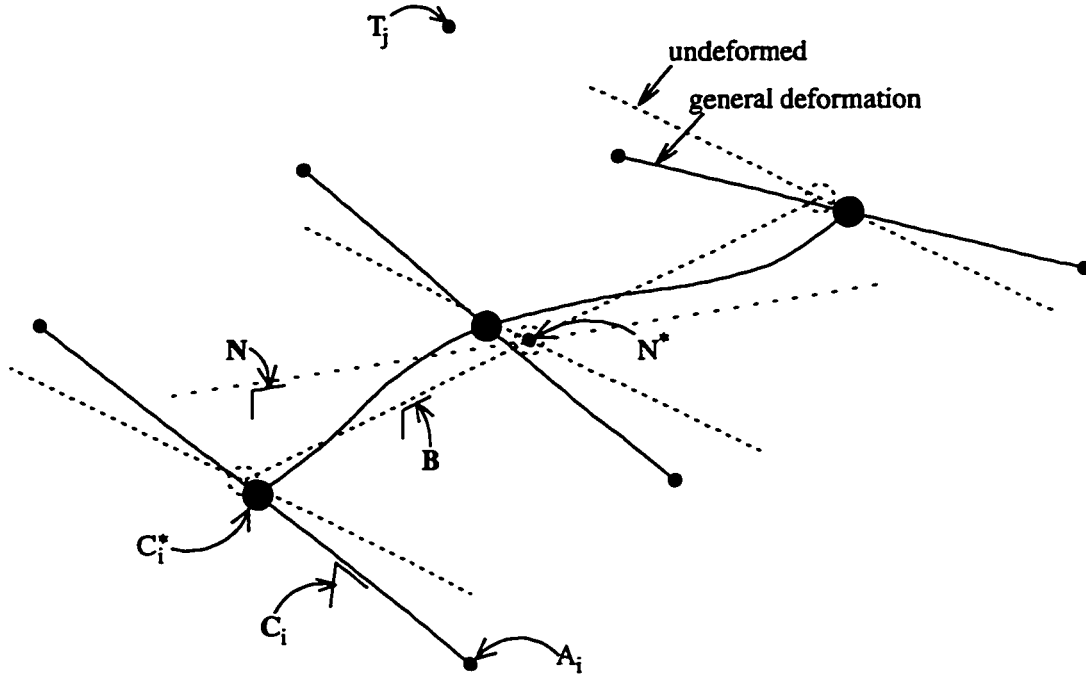


Figure 6.5: Deformed Structure and Point Definitions

The position vector from point T_j to point A_i is expressed in three parts — T_j to N^ , N^* to C_i^* , and C_i^* to A_i , all expressible in terms of the generalized coordinates, q .*

to know the phase center positions of the transmit antennas in the laboratory. These transmitter positions are denoted $\underline{p}^{N^*T_j}$ and are assumed known. A survey was performed in the laboratory to determine the phase center locations of the transmitters that used the GPS signals from the transmitters as the information source. A description of this calibration is given in Appendix E.

6.3.1 The Measurement Equation

Fig. 6.5 shows an example of the geometry of the deformed flexible structure. Some useful reference points are denoted on the figure. Now, it is possible to build $\underline{p}^{T_jA_i}$ in terms of known quantities and generalized coordinates. First, expand the position vector as follows:

$$\underline{p}^{T_jA_i} = \underline{p}^{T_jN^*} + \underline{p}^{N^*C_i^*} + \underline{p}^{C_i^*A_i} \quad (6.25)$$

$\underline{p}^{T_j N^*}$ - A constant vector known from a survey.

$\underline{p}^{N^* C_i^*}$ - A vector expressible in the B frame in terms of generalized coordinates.

$\underline{p}^{C_i^* A_i}$ - A known constant vector in the C_i frame.

Now, let a left superscript denote a reference frame in which a position vector is expressed.⁶

Also, denote a linear coordinate transformation matrix, \mathbf{T} .⁷ Thus,

$$\underline{p}^{N^* T_j A_i} = \underline{p}^{N^* T_j N^*} + {}^{NB}\mathbf{T} \left(\underline{p}^{B N^* C_i^*} + {}^{BC_i}\mathbf{T} \underline{p}^{C_i^* C_i^* A_i} \right) \quad (6.26)$$

Diagram illustrating the components of the position vector equation (6.26):

- $\underline{p}^{N^* T_j A_i}$: Desired vector. A function of q .
- $\underline{p}^{N^* T_j N^*}$: Known from static survey.
- $\underline{p}^{B N^* C_i^*}$: Written in terms of rigid-body parameter, q_{10} .
- $\underline{p}^{C_i^* C_i^* A_i}$: Written in terms of rotation generalized coordinates, $q_2, q_3, q_5, q_6, q_8,$ and q_9 .
- $\underline{p}^{C_i^* C_i^* A_i}$: A known constant vector in the C_i frame.
- $\underline{p}^{C_i^* C_i^* A_i}$: Written in terms of translation generalized coordinates, $q_1, q_4,$ and q_7 .

Now, all that is required is to substitute the expressions for the position vectors and transformation matrices in terms of the generalized coordinates (q 's) into Eq. 6.26. Then the measurement function, $h(x)$, is given by Eq. 2.7. One final detail is that the position vectors are actually a function of q 's rather than the states, x , but because the measurements are not a function of the rate of change of coordinates, the measurement function can be written (let fn denote any functional),

$$h(x) \underset{(6.10)}{=} fn(\xi) \underset{(6.6)}{=} fn(U^T q) \underset{(U \text{ const})}{=} fn(q) \quad (6.27)$$

⁶ A position vector written \underline{p}^{AB} is read "the position vector from point A to point B expressed in terms of unit vectors fixed in frame C ."

⁷ A transformation matrix written ${}^{BA}\mathbf{T}$ is read "the transformation of a vector expressed in frame A to frame B ."

6.3.2 Measurement Linearization

The final step is linearization of $h(x)$ such that the function may be efficiently computed in real-time. Also, the linearization provides the gradient matrix, H , which is used in the estimator of Chapter 7. The goal is to express the linearized measurement equation as in Eqs. 6.3 and 6.4,

$$h(x) \cong H_x(\hat{x})\delta x + h(\hat{x}) \quad (6.28)$$

$$\text{with,} \quad x = \hat{x} + \delta x$$

$$q = \hat{q} + \delta q$$

$$H_{(\cdot)} = \frac{\partial h}{\partial (\cdot)}$$

The state estimate, \hat{x} , is the state about which equations are linearized. Now it is possible to take advantage of the assumption that all generalized coordinates are assumed small (and nominally zero) except the rigid-body rotation variable, q_{10} . Write,

$$U_{\hat{x}} \stackrel{(\text{6.10})}{=} \begin{bmatrix} U_{\hat{\xi}} \\ U_{\dot{\hat{\xi}}} \end{bmatrix} \stackrel{(\text{6.6})}{=} \begin{bmatrix} \hat{q} \\ \dot{\hat{q}} \end{bmatrix} = \begin{bmatrix} 0 \\ \vdots \\ 0 \\ \hat{q}_{10} \\ 0 \\ \vdots \\ 0 \end{bmatrix} \quad (6.29)$$

Thus the functions of \hat{x} in Eq. 6.28 are only a function of \hat{q}_{10} :

$$h(x) \cong H_x(\hat{q}_{10})\delta x + h(\hat{q}_{10}) \quad (6.30)$$

where $H_x(\hat{q}_{10}) = H_x(\hat{x})$ and $h(\hat{q}_{10}) = h(\hat{x})$. It is also useful to note that

$$H_x = \frac{\partial h}{\partial x} \stackrel{(\text{6.10})}{=} \frac{\partial h}{\partial \begin{bmatrix} \xi \\ \dot{\xi} \end{bmatrix}} = \left[\frac{\partial h}{\partial \xi} \mid \frac{\partial h}{\partial \dot{\xi}} \right]$$

$$\stackrel{(\text{6.27})}{=} \left[\frac{\partial h}{\partial q} \frac{\partial q}{\partial \xi} \mid 0 \right] \stackrel{(\text{6.6})}{=} \left[H_q U \mid 0 \right]$$

$$H_x(\hat{q}_{10}) = \left[H_q(\hat{q}_{10})U \mid 0 \right] \quad (6.31)$$

This leads to the final expression of the measurement,

$$h(x) \cong \left[H_q(\hat{q}_{10})U \mid 0 \right] \delta x + h(\hat{q}_{10}) \quad (6.32)$$

For this research, the following steps were completed to enable evaluation of Eq. 6.32 by the computer in real-time.

1. Wrote algebraic expressions for $h(q)$ by substituting Eq. 6.26 into Eq. 2.7.
2. Wrote the partially linearized expression by substituting $q = \hat{q} + \delta q$ and linearizing in δq .

$$h(q) = h(\hat{q}, \delta q) = h(\hat{q}_{10}, \delta q) \quad (6.33)$$

3. Separated the terms of h by δq .

$$h(q) = H_q(\hat{q}_{10})\delta q + h(\hat{q}_{10}) \quad (6.34)$$

4. Wrote functions that can be evaluated in real-time to return the matrix $H_q(\hat{q}_{10})$ and vector $h(\hat{q}_{10})$ given the current best estimate of rigid-body rotation angle, \hat{q}_{10} .

Steps 1–3 were performed using the computer symbolic manipulator Autolev[®] for algebraic manipulations and linearization. Algebraic expressions for $H_q(\hat{q}_{10})$ and $h(\hat{q}_{10})$ were written to a text file in Autolev[®] format (50 pages). Next, a translation program was written in Perl 5.0 [Wall and Schwartz, 1991] that reads the Autolev[®] file and writes a file (70 pages) containing functions in the C language that can be compiled with the real-time code. The final compiled real-time code can compute $H_q(\hat{q}_{10})$ and $h(\hat{q}_{10})$ in 5 milliseconds on a Pentium[®]200 computer.

6.4 Summary

This chapter describes the dynamic and kinematic modeling of the flexible structure system. The first step is the definition of generalized coordinates, q , that specify translations and rotations of the rigid sections of the assembly. The definition of the rigid-body degree of freedom is also given.

Next, linear equations of motion are written that predict the variation of q with time. A modal transformation based on the results of a finite element structural analysis is presented and the results inserted into the equations of motion. The equations of motion are expressed in terms of the state vector, x , composed of modal coordinates and their rates of change. Next, a force model analysis is shown for inclusion of thruster forces in the equations of motion.

The next part of the model involves measurement kinematics. The measurement equations are derived as a function of generalized coordinates, q . Since the rigid-body coordinate is not assumed to be small, the measurement equation cannot be fully linearized. A method of linearization is shown that takes advantage of the assumption that all generalized coordinates except the rigid-body rotation coordinate are small. This results in a set of equations that can be evaluated efficiently in real-time.

The physical modeling shown in this chapter is fundamental to bias initialization (Chapter 3) and the real-time experimental work (Chapters 7 and 8) shown in this dissertation.

CHAPTER 7

Real-Time State Estimation

An integral part of many control systems is a real-time state estimator. The real-time estimator answers, “Given past estimates, a model, and current measurements, what is the best guess of the state?” This chapter shows the elements of the real-time estimator that is used to provide state estimates for the control work in the following chapter. A block diagram of the estimator is shown in Fig. 7.1. Notice that in addition to the model and measurements, an initialization of the unknown bias ambiguities (see Chapter 3) is required to start the estimator. Once the biases are known, the recursive estimator can be started.

7.1 Recursive Estimator Equations

The recursive real-time estimator used for this work is based on the discrete Extended Kalman Filter [Gelb, 1974], or EKF. After the arrival of the measurements, the estimator processes the new information in two steps:

- 1. Time Update:**

The new system state propagated from the previous state using the system model. Also, an estimate of the state error covariance matrix is propagated using the model.

- 2. Measurement Update:**

The state and covariance estimates are updated using the current measurement information.

The EKF equations that implement these steps are as follows:

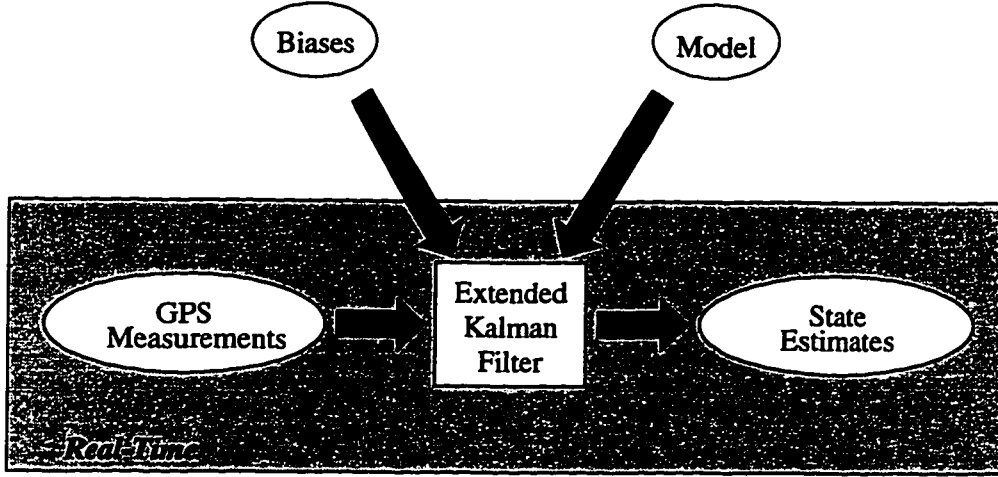


Figure 7.1: Diagram of Real-Time Processing

Given initial knowledge of the bias ambiguities and a model, the real-time estimator computes state estimates with each new set of GPS data.

GIVEN

The model of Eqs. 6.1–6.3

x_0 = initial condition guess

β = bias ambiguity estimate

$$W = E[w_k w_k^T] \quad (7.1)$$

$$R = E[\nu_k \nu_k^T] \quad (7.2)$$

TIME UPDATE

$$\bar{x}_k = A x_{k-1} + B u_{k-1} \quad (7.3)$$

$$\bar{P}_k = A P_{k-1} A^T + B_w W B_w^T \quad (7.4)$$

MEASUREMENT UPDATE

$$P_k = \bar{P}_k - \bar{P}_k H_k^T [H_k \bar{P}_k H_k^T + R]^{-1} H_k \bar{P}_k \quad (7.5)$$

$$r_k = y_k - h_k(\bar{x}_k) \quad (7.6)$$

$$K = P_k H_k^T R^{-1} \quad (7.7)$$

$$x_k = \bar{x}_k + K r_k \quad (7.8)$$

“Barred” variables denote intermediate quantities between the time and measurement updates. A , B , and B_w are from the model of Eq. 6.1. The discrete process and measurement noises, w_k and ν_k , are assumed white and zero mean. The measurement noise covariance in Eq. 7.2, R , is set to $0.02^2 \cdot I$ to reflect the expected 2 cm measurement noise standard deviation. The process noise covariance in Eq. 7.1 was chosen based on observed estimator performance. The final choice used is $W = \text{diag}(0.5^2 \dots 0.5^2 \ 0.05^2)$.

7.2 Some Practical Issues

7.2.1 Matrix Computations in C

The bulk of the real-time processing effort is spent computing the matrix arithmetic of the EKF filter. For example, Fig. 5.2 shows that almost 70% of the 100 ms cycle is spent in the estimator.¹ Thus, computational savings in the matrix manipulations may significantly increase the real-time processing capability.

It is also important for the researcher to have matrix operation code that is intuitive and safe. Intuitive code is code that does not hide the underlying mathematics, and safe code will warn a programmer of an error rather than crashing.

Unfortunately, “efficient” and “intuitive/safe” are usually conflicting characteristics. In an attempt to find the best combination of efficiency and ease of use for this work, a library of functions for matrix operations in C was developed based on previous work by Lawrence [Lawrence, 1996] and Pervan [Pervan, 1996]. The library routines are a convenient interface to code optimized for speed and efficiency. This new matrix library allows a programmer to manipulate matrices and vectors using “index vectors.” Index vectors provide the ability to manipulate a subset of the rows and columns of matrices.² An index vector is a vector of monotonically increasing, non-repeating integers that represent row or columns numbers. With index vectors, new measurements can be brought online and invalid measurements dropped seamlessly in real-time. Also, states (such as new measurement bias

¹Further investigation reveals that about 70% of the estimator computation is spent in the measurement covariance update (Eq. 7.5), an operation with many multiplications, and a large matrix inversion.

²This is similar to the operation of the matrix language MATLAB[®].

states) can be easily included or excluded from the estimator in real-time.

7.2.2 Efficient Measurement Equation Computation

Because the measurement equation is complex and non-linear, it is advantageous to compute the measurement function, h_k , and its gradient, H_k , only when necessary. Since these functions are non-linear only in the rigid-body variable, \hat{q}_{10} , the functions need to be re-evaluated only if the rigid-body angle has changed by a large angle since the last evaluation. This logic can be summarized by the following steps:

1. Let the reference state for linearization, \hat{x} , equal the initial state guess, x_0 .
2. Compute $H_q(\hat{q}_{10})$ and $h(\hat{q}_{10})$ in Section 6.3.2 using \hat{x} .
3. Upon the arrival of new measurements, compute the time update (Eq. 7.3) and let $\delta x = \bar{x} - \hat{x}$.
4. Compute the measurement update using $H_k = H_x(\hat{q}_{10})$ from Eq. 6.31 and the approximate $h(x)$ from Eq. 6.30.
5. Next, check if the rigid-body estimate has changed by more than some threshold since the last linearization (a threshold of 4° was used for this research).
 - If no, go to step 3.
 - If yes, let \hat{x} equal the new state estimate, and go to 2.

This logic was implemented and used for the experiments shown in this dissertation.

7.3 Example of Real-Time Estimator Operation

This section describes an experiment designed to evaluate the performance of the real-time state estimator. First, some results of the necessary bias initialization process (using the techniques of Chapter 3) are presented. Then, the system maneuver is described, and the estimator output is shown. Results are compared with estimates based on the rate gyroscope sensors.

7.3.1 Bias Initialization

The first step is initialization of the unknown biases, as discussed in Chapter 3. Data were collected during free motion of the flexible structure that included 35° of rigid-body rotation. The batch dynamic estimator described in Section 3.4 was applied to the data and a solution found. Fig. 7.2 shows the convergence of the iterative estimator. The solid line is the mean of the RMS residuals. The residual magnitudes are shown to converge to under one centimeter in 20 iterations. The dashed line is the mean of the roots of the diagonal elements of the covariance matrix corresponding to the bias states. A covariance root of one to two centimeters plus the residual magnitudes at convergence indicate that the error in the bias solution, due to random noise, is approximately 2 cm. This accuracy is sufficient to confidently set the bias states. Also, if line bias estimates are available (see Section 3.1 for discussion), the bias solution error can confidently be rounded to the nearest integer, since 2 cm is only 10% of a carrier wavelength.

Fig. 7.3 shows the residuals and the rigid-body state after convergence. The residuals appear to be white and regular (no stray values). This is a common check for estimator convergence. The rigid-body state appears to be nearly linear throughout data collection, except for a deviation at the end. The deviation is likely due to forces exerted on the system near the end of the test by the researcher (not modeled). This also explains the small deviation in a few of the residuals near the same time in the plot.

A practical note about bias estimates is important here. Bias estimates are only valid while the receiver maintains lock on a signal. If a signal is newly acquired (or reacquired), some biases must be initialized (reinitialized). For example, if a satellite rises in the sky and becomes visible during operation, use of the new signal requires a bias initialization. Fortunately, it is usually possible to estimate the new biases without resorting to the batch technique used to find the biases initially. The knowledge of biases from other signals can provide the information needed to estimate new biases. This technique was verified in some tests using simulated data but was not tried experimentally.

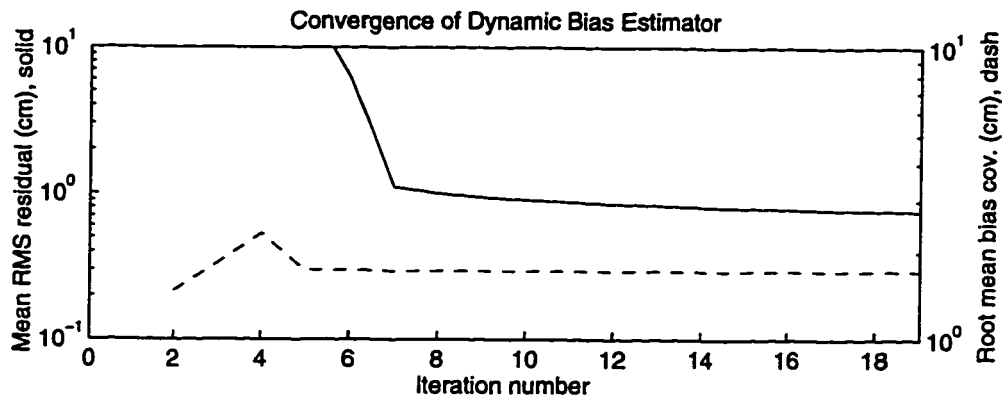


Figure 7.2: Bias Estimator Convergence

The convergence of residual magnitudes for twenty iterations is shown in this plot. The corresponding covariance of the bias states is also shown.

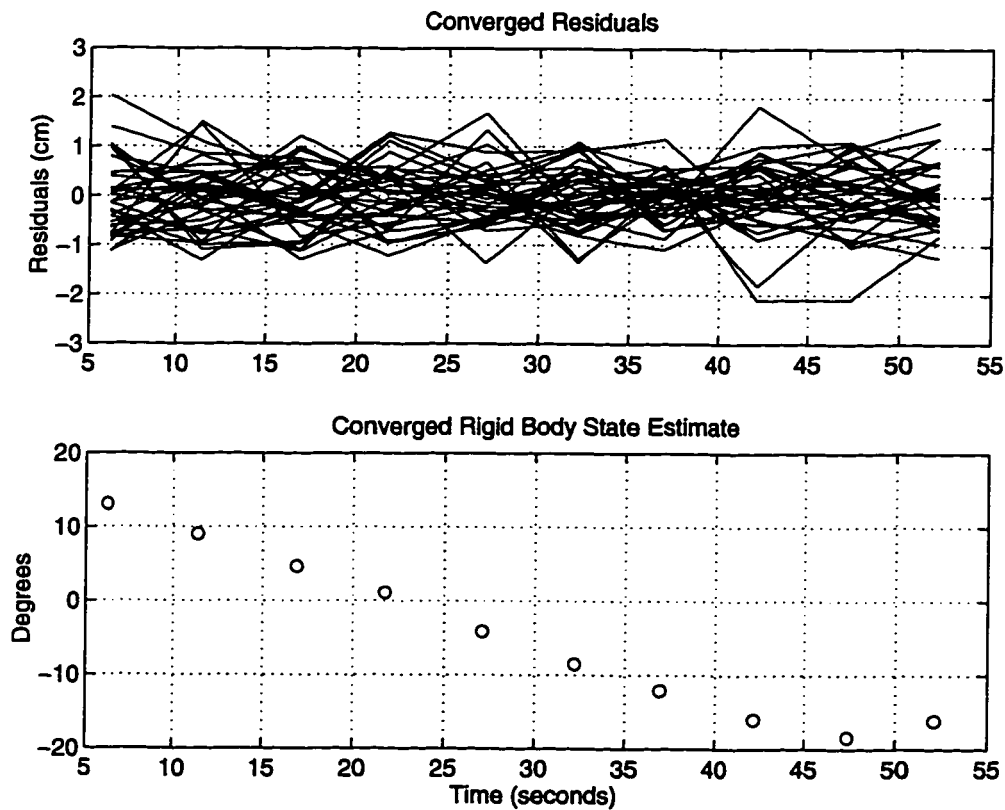


Figure 7.3: Residuals and RB State After Convergence

These plots reveal some important results of the bias estimator convergence, the final residuals, and the resulting estimate of the rigid-body state.

The result of the initialization is a set of bias estimates accurate to a few centimeters. These estimates can then be used to start the recursive estimator.

7.3.2 Recursive Operation

In this section, two tests of the recursive estimator operation are shown. The data presented were taken after a bias estimate computation as described in the previous section. While the structure possesses many degrees of freedom, a single DOF was chosen that is easy to visualize for evaluation of the estimator performance: the rotation angle of the structure's center rigid section about a lab-fixed vertical axis (see Fig. 7.4). This angle will henceforth be referred to as the CSV angle (center section vertical).

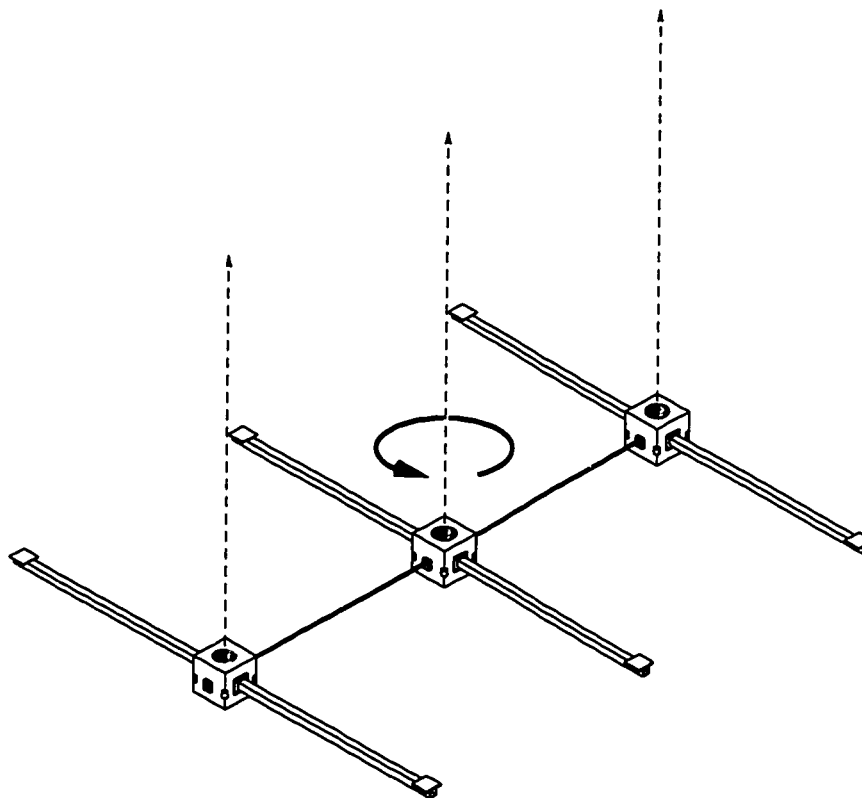


Figure 7.4: Motion Studied for Estimator Evaluation

The CSV angle (center section vertical) is the rotation of the structure's center rigid body about a lab-fixed vertical axis (indicated with the arrow). This parameter is used to evaluate estimator accuracy in Section 7.3.2.

Each test compares the GPS based estimate of the CSV angle and the estimate of the same angle computed from rate gyroscope measurements. The rate gyroscope estimates are obtained by integrating the body-fixed vertical axis gyro signal, which is equal to the laboratory-fixed rotation for small out-of-plane rotations (out-of-plane motions were small for all the tests shown).

Static test

After bias resolution, the structure was allowed to come completely to rest at approximately 0° rigid-body angle (\pm a couple of degrees). A laser optical survey of the rest position estimated the CSV angle to be -1.4° . Then, data from GPS and gyro sensors was collected. The resulting estimates of the CSV angle from GPS and gyro estimates can be seen in Fig. 7.5. The top plot shows the GPS and gyro estimates and the bottom plot shows their difference. The GPS estimator predicts the CSV angle to be approximately -1.48° , and the corresponding GPS estimate noise is less than 0.02° RMS. The gyro estimate (initialized by the GPS estimate) has comparable white noise magnitude but has a noticeable drift over time. As expected, the GPS estimate has no detectable drift for this static test.

The extremely low GPS estimate noise is due to the low measurement noise for static tests (about 2mm RMS for this test) and the highly redundant measurement set (36 measurements and 18 states). The drift of the gyros is noticeable, but small for these static tests. The gyro drift is much more significant for the dynamic tests, as demonstrated in the next section.

It is very encouraging that the GPS estimates and the laser survey agree to within a tenth of a degree. This result is a confirmation of the validity of both the transmitter phase center survey (see Section 6.3 and Appendix E) and the bias estimate computed prior to the static test.

Dynamic test

The following maneuver was performed to test the estimator performance for rigid-body and vibration motions. This test was performed after a bias estimate was found as described

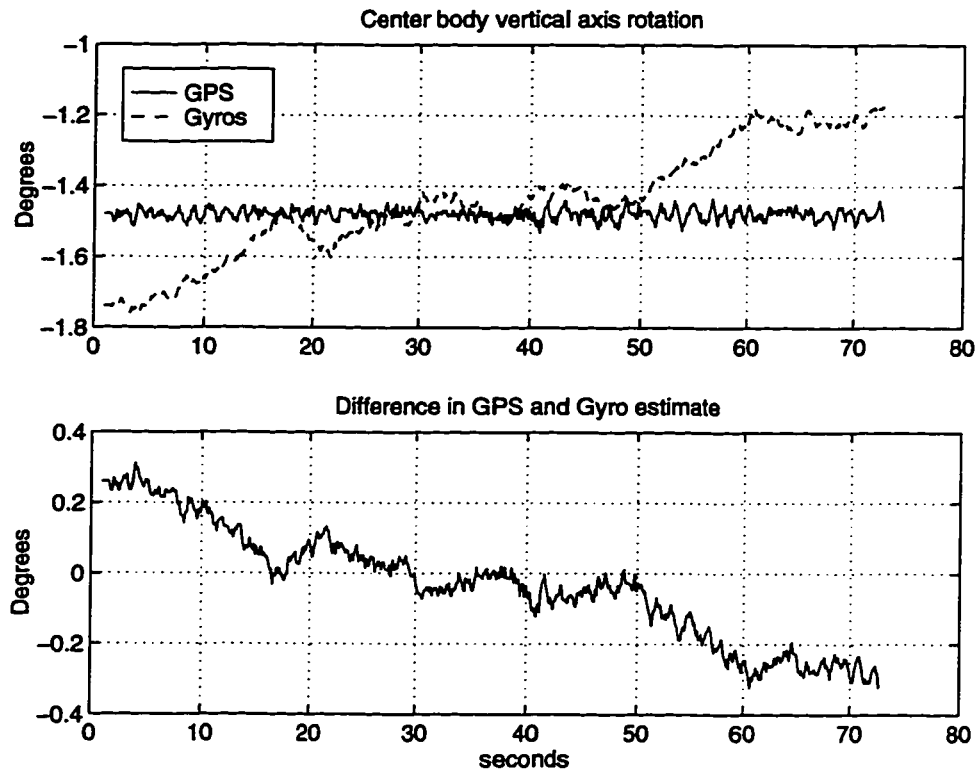


Figure 7.5: Static Estimator Comparison

This plot shows the GPS and rate gyroscope-based estimates of the CSV angle during a static test. A laser optical survey predicted the angle to be -1.4° . The bottom plot shows the difference of the two independent estimates.

in the previous section. The structure was initially rotated (manually) as a whole in the horizontal plane to illustrate state estimation during a large scale platform slew. Then (after about 140 seconds), the structure was randomly excited to illustrate estimation during elastic vibration. Table 7.1 summarizes the estimator test procedure. As in the static test, the CSV angle will be used to evaluate estimator performance.

Fig. 7.6 plots estimates of the CSV rotation angle computed in real-time during the maneuvers described in Table 7.1. GPS-based and gyro-based estimates are plotted. It is evident from the plot that the two independent sensors qualitatively agree, but a noticeable drift over time is present. This drift is consistent with the known behavior of rate gyro sensors.

Interval (seconds)	Description
0–50	Near static. The structure has slight vibrations at a small (about 5 degree) rigid-body offset
50–100	Slew maneuver in the negative direction for a total of nearly 17°. Some small vibrations present.
100–140	The structure is slewed back to near 0° rigid-body angle, and stopped.
140–225	An impulsive disturbance is introduced to the system that creates significant internal elastic vibrations.

Table 7.1: Estimator Test Experiment Procedure

This table describes the test procedure used to create the plots shown in Fig. 7.6.

The difference between the GPS and gyroscope-based estimates are shown in Fig. 7.7. The top plot illustrates a linear trend in the difference that is attributable to drift in the gyroscopes. The second plot shows the difference with the linear trend removed. For analysis of GPS estimates, it is fair to remove this trend that is known to be contributed by the gyros alone (as shown in the static test, common clock differential carrier phase measurements do not drift over time). The second plot shows that the difference is always less than one degree and has an RMS value of 0.3 degrees. These results show that the estimates based on the independent sensors agree during both the slew maneuver and during elastic vibration.

7.3.3 Linearization About the Rigid-Body Configuration

As discussed in Section 6.1, the model used in this estimator is linearized about the “unstressed” or rigid-body configuration of the system. Given inevitable model errors, it is important that the measurements provide sufficient observability of the rigid-body orientation so that this linearization is valid. Inertial sensors alone are not well suited for this task due to their drift characteristics. The dynamic experiment of this section provides insight into this issue.

In Fig. 7.7, errors that are correlated with the rigid-body slew can be observed. Specifically, the GPS estimates slightly lag the gyro estimates. This occurs because the GPS

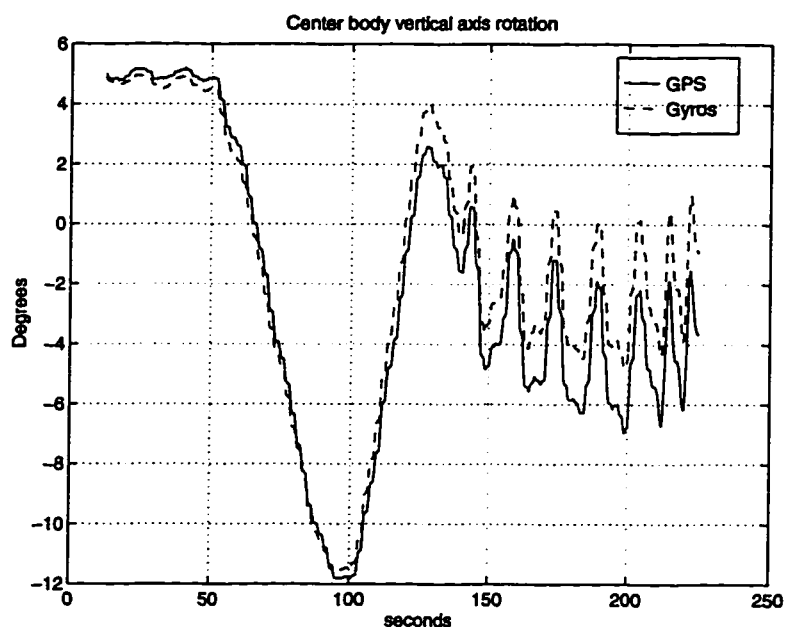


Figure 7.6: Comparison of GPS and Gyro Based Estimates

This plot shows a comparison of GPS and rate gyroscope based estimates of the CSV angle shown in Fig. 7.4 during the maneuver described in Table 7.1.

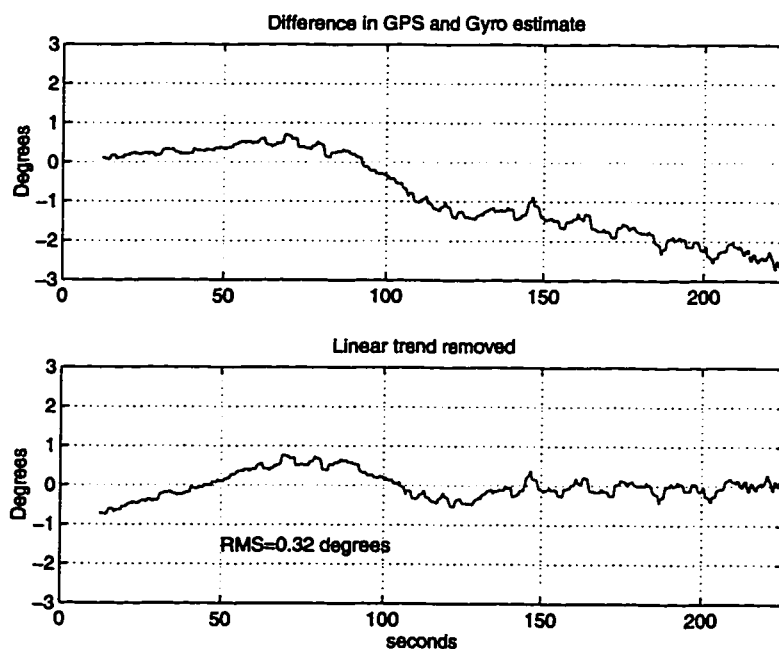


Figure 7.7: GPS and Gyro Estimate Difference

This plot shows the difference between the two lines in Fig. 7.6. The second plot shows the result with the best fit linear trend removed.

estimates use an unforced model for this test. Forces imparted on the structure by the researcher to induce the desired motion were not included in the estimator. The forces could be included, but for now, their absence is a convenient known source of model error (such forces are included in the control experiments of the next chapter). The second plot illustrates the ability of the estimator to retain a sufficiently accurate angle estimate (under 1° error with respect to gyroscope estimate) to ensure linearization integrity.

7.4 Summary

This chapter describes the real-time state estimator developed for this research. The estimator uses the models of dynamics and measurements from Chapter 6 and uses data from the GPS sensors alone. An algorithm overview is shown and the estimator equations are presented. Some practical details of real-time processing with matrices are also discussed. The estimator provides the state estimates that are used by the control algorithms of the next chapter (Chapter 8).

A static experiment verifies rigid-body pointing accuracy of 0.1° as measured with respect to a laser survey. Then, an experiment is presented to evaluate the success of the estimator during system motion. First, the results of a bias initialization using the dynamic algorithm of Section 3.4 are shown. Then, real-time estimation during subsequent system motion is evaluated by comparing the results of independent GPS and rate gyroscope based estimates. The experiment tests the estimator during both rigid-body rotation and elastic vibration. Angular agreement of 0.3° between GPS and gyroscopes is shown after gyro drift is removed.

These results are significant in that they demonstrate a sub-degree, sub-centimeter sensor of general structural deformations with zero drift characteristics (as seen in the static test). This performance is available wherever the GPS signal environment exists, either from the GPS satellites or from pseudolite transmitters.

CHAPTER 8

Experiments in Real-Time Control

One of the most compelling tests of the performance of a sensor is its use in a feedback control loop. This chapter shows the real-time control experiments that verify the value of GPS as a structural deformation sensor for control. The control objectives are:

- Successfully damp elastic vibrations in the test structure with a real-time control system.
- Demonstrate an automatic rigid-body orientation slew maneuver with simultaneous structural vibration control.

While it is possible to use the information from the on-board rate gyroscopes in the controller, this is not done in the experiments shown here. GPS information is used alone to highlight its utility as a stand-alone sensor for flexible structures. Integration of other sensors could be a valuable technique for some applications (see [Montgomery *et al.*, 1994] for a discussion).

8.1 Controller Design

The controller used for the data presented in this chapter is a full-state regulator that minimizes a quadratic function of weighted states and control outputs (known as a linear quadratic regulator, or LQR). The weights were tuned by processing simulated data. Further control design may improve real-time performance and is a topic for further investigation.

Given the model equations from Eq. 6.1, the standard LQR formulation is as follows.

Given:

$$x_{k+1} \stackrel{(6.1)}{=} Ax_k + Bu_k \quad (8.1)$$

Find the constant gain full state feedback controller:

$$u_k = -Kx_k \quad (8.2)$$

to minimize the cost function

$$J = \sum_{j=0}^{\infty} x_j^T Q_x x_j + u_j^T Q_u u_j \quad (8.3)$$

The well-known steady-state solution to this LQR problem is,

$$K = (Q_u + B^T S B)^{-1} B^T S A \quad (8.4)$$

where the positive definite symmetric matrix S solves the steady-state Riccati equation,

$$0 = S - A^T S A + A^T S B (Q_u + B^T S B)^{-1} B^T S A - Q_x \quad (8.5)$$

These matrix equations can usually be solved using an eigenvector decomposition of the Hamiltonian matrix for this system. For a discussion of this method, see [Franklin *et al.*, 1990]. For this research, the solution was found using the DLQR function in the MATLAB® matrix language.

The weights on the state errors and control inputs used for the experiments shown in this chapter are as follows. Let Q_x^* be defined as a diagonal matrix:

$$Q_x^* = 5000 \times \text{diag}(1, 1, 1, 1, 1, 1, 1, 1, 0.01); \quad (8.6)$$

then,

$$Q_x = \begin{bmatrix} Q_x^* & 0 \\ 0 & 0.01 Q_x^* \end{bmatrix} \quad (8.7)$$

This weights the twist and bending modes equally and the rigid-body mode one hundred times lower. All of the mode rate states are weighted the same, but lower by a factor of 100. This penalizes the “speed” of the motions but puts an emphasis on the position error.

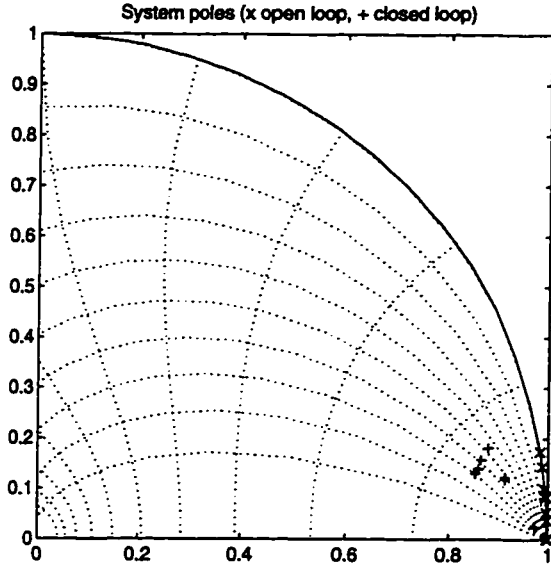


Figure 8.1: Pole Locations

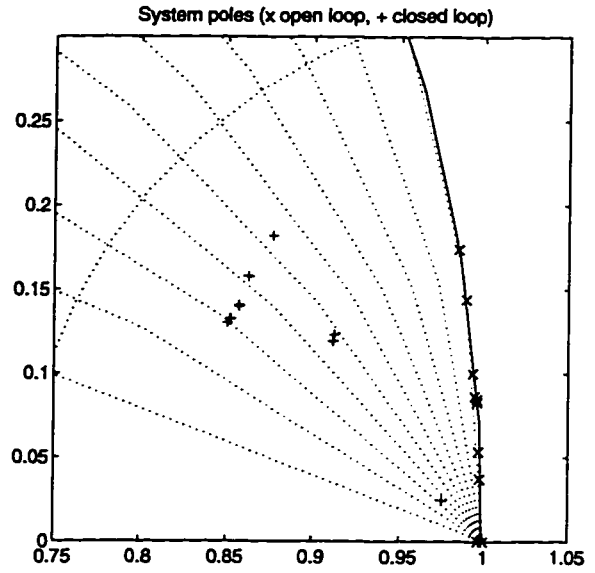


Figure 8.2: Pole Locations (zoomed)

The control inputs are weighted equally to unity:

$$Q_u = I \quad (8.8)$$

Analysis of the system using these weights yields open and closed-loop poles shown in the z-plane in Fig. 8.1. The open-loop poles are shown as \times and the closed-loop poles as $+$. The open-loop poles are very lightly damped (very near the unit circle) and are well under the Nyquist limit (close to $z = 1$). Fig. 8.2 shows that the closed-loop poles are indeed stable and damped. Better response times would require loop gains that would produce control commands out of range of the gas jet actuators.

From Section 5.2 of [Franklin *et al.*, 1990], the settling time, t_s , is a function of the radius of the pole location, r_0 , according to the formula,

$$t_s = \frac{-4.6}{\ln(r_0)} T \quad (8.9)$$

where T is the sampling period (0.1 sec). All of the closed-loop poles in this analysis are around 0.9, corresponding to settling in 44 samples. At 10Hz, this predicts

$$t_s \approx 5 \text{ seconds} \quad (8.10)$$

The single closed-loop pole that is much closer to $z = 1$ than the other poles is the closed-loop rigid-body pole. This mode was given less control gain than the vibration modes to reduce overshoot in the slew maneuvers. The settling time of the rigid-body mode is 30 seconds. The open-loop pole settling times are between 4 and 20 minutes, by comparison.

Two simulations were performed to test the closed-loop response of the system with the full state feedback controller shown above. First, vibration damping was tested by simulating the response of the open and closed-loop system given an initial state offset. The initial condition chosen was $q_3 = 3^\circ$, $q_4 = 10$ cm, and $q_5 = 15^\circ$ (q 's are defined in Fig. 6.1). Fig. 8.3(A) shows three time response curves for each of the three generalized coordinates:

1. The solid line is the open-loop (free response) curve. No damping is present over the time scale of the plot.
2. The dashed line is the closed-loop curve. Settling times are approximately 5 seconds for the coordinates shown.
3. The dot-dashed line shows the closed-loop response curve when all negative control commands are discarded (set to zero). See Section 8.2 for a discussion of this control technique.

The second simulation tested the system response to a rigid-body slew command of 30° . Fig. 8.3(B) shows the same three curves used for the vibration damping simulation of Fig. 8.3(A). The open-loop (solid) curve is a straight line at 30° indicating the static rigid-body angle in the absence of control. The closed-loop curves show slew response times of 30-40 seconds with only a single overshoot of a couple of degrees. These simulations provide confidence in being able to implement the controller successfully on the real experimental system. However, a final step is necessary. A technique is needed to transform the control commands computed from Eq. 8.2 to signals that are realizable with on/off thrusters. The following section describes such a technique.

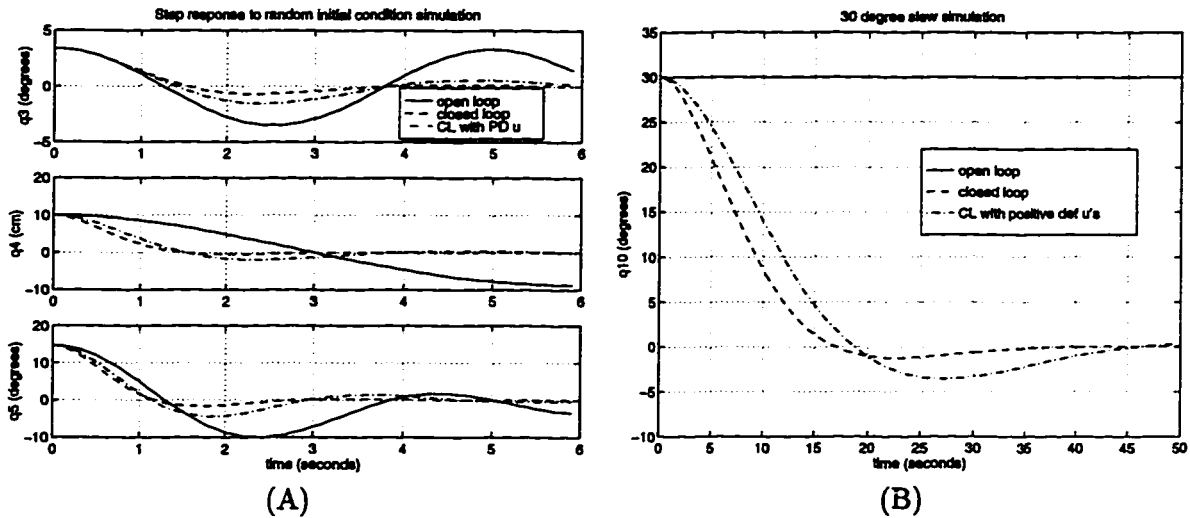


Figure 8.3: Controller Simulations

(A) shows the response to an initial condition and (B) shows a 30° commanded slew maneuver. The solid lines are the open-loop response and the dashed lines are closed-loop. The dot-dash lines are the response when all negative control commands are discarded (set to zero). See Section 8.2 for a discussion of this control technique.

8.2 Thruster Pulse Modulation

After the state is estimated, the control command is given by the vector, u , from Eq. 8.2. The elements of u can be any floating point value. However, the gas jet actuators are binary valued, either “on” or “off.” Intermediate commands can be realized by pulsing the thrusters, with a few important limitations:

1. Actuator saturation. The thrust from a constantly open jet is the maximum available force.
2. Only positive commands can be realized. In some systems, jets can be mounted in directly opposing pairs. However, this technique may require many more actuators than necessary for a particular system. The flexible structure system does not use directly opposing pairs.
3. Thrusting is limited by the maximum cycle rate. In particular, the minimum force is limited by the minimum single pulse duration.

For the control experiments in this chapter, the thrusters were pulsed according to a pulse-width, pulse-frequency (PWPF) modulation algorithm. A PWPF algorithm attempts

to approximate a continuous forcing command by pulsing an on/off actuator. The frequency and width of the pulse can be varied to change the continuous wave equivalent force. For the experiments in this section, a high-priority thread (see Fig. 5.1) is created to execute at 100Hz, the maximum frequency of the thrusters. This thread contains an independent integer counter for each thruster, c_i . The state of each thruster is decided every thruster cycle by comparing c_i to c_i^{ON} and c_i^{TOT} , integers provided each measurement cycle by the controller thread. If $c_i \leq c_i^{ON}$, the thruster valve is opened. Also, if $c_i > c_i^{TOT}$, c_i is reset to zero, restarting the pulse cycle of thruster, i . Fig. 8.4 illustrates this logic.

The transformation from u to integers c_i^{ON} and c_i^{TOT} is the last step. First, u is scaled to units of the maximum thruster force, T_{max} . Then, to avoid saturation, if any element of u exceeds 1.0, the whole vector u is scaled such that the maximum element equals 1.0. This maintains the “shape” of the thrust vector in the event of saturation. However, the scaled thrust vector can contain negative values that are not realizable with non-opposing on/off thrusters (the thrusters were not mounted in opposing pairs for reasons discussed in Section 4.3). Thus, a method of handling negative force commands is needed.

Because each rigid section has enough thrusters to generate any force or torque that might be requested by the controller, it could be possible to re-map the thruster commands so that the equivalent torque and force is produced using only positive thrusts. However, as a first attempt, the closed-loop system was simulated with all negative thrust commands set to zero. These simulations produced the dot-dashed lines in Fig. 8.3. The response of the system is stable with an apparent gain reduction using the negative truncation method. It is believed that the success of this simple technique depends largely on the symmetry of the thruster configuration on each rigid section of the test structure, and more sophisticated techniques might be required to ensure success with general thruster orientations. However, due to its simplicity and effectiveness (demonstrated in simulation in Fig. 8.3), the negative truncation technique was used for the real-time control experiments shown in the remainder of this chapter.

Now, the command vector u contains a floating point number between 0.0 and 1.0, representing the percentage of full thrust required for each thruster. To convert to c_i^{ON} and

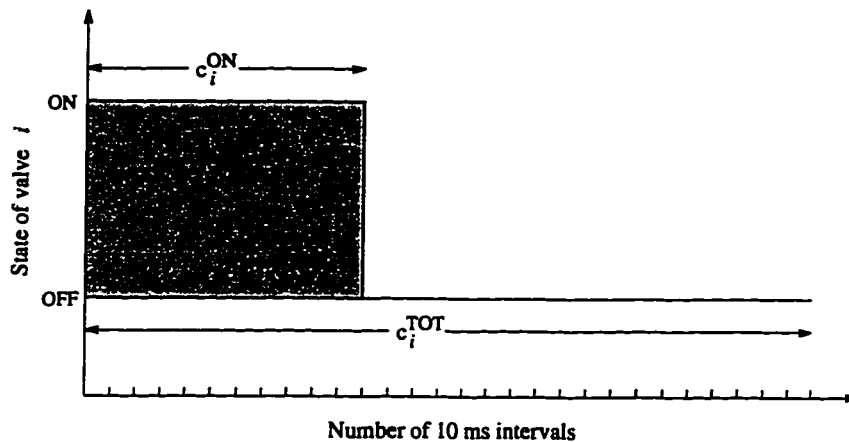


Figure 8.4: A Thruster Cycle

A thruster pulse is illustrated in this figure that is on for c_i^{ON} counts and off for $c_i^{TOT} - c_i^{ON}$ counts.

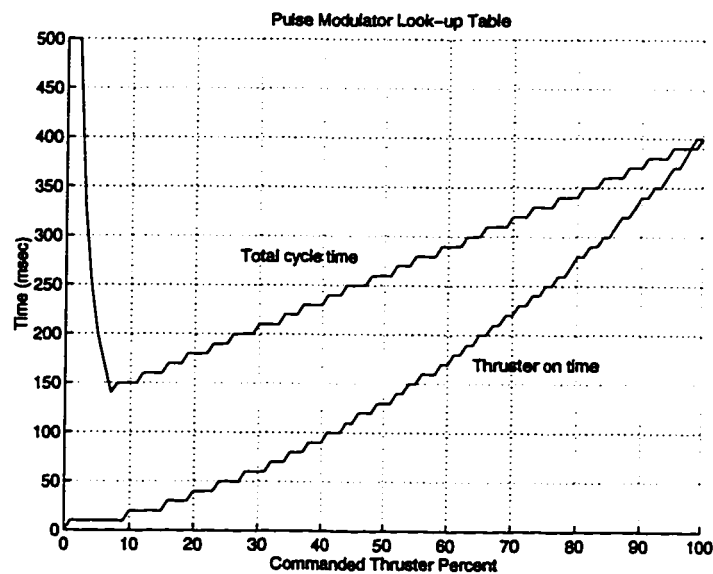


Figure 8.5: PWPF Lookup Table

The "on-time" and "cycle-time" for a thruster is found from this table, given a desired percentage of max thrust.

c_i^{TOT} counts, the lookup table shown in Fig. 8.5 was used. Thruster cycle periods in the 150–500 ms range were chosen, considering a tradeoff between thrust accuracy and control command bandwidth. Longer cycles allow better precision with 10ms quantized pulses, but shorter cycles prevent the errors due to control commands that change faster than the cycle period. As an example of lookup table use, if 70% of a thruster is required, the thruster is turned on for the first 220ms ($c_i^{ON} = 22$ counts) of a 320ms ($c_i^{TOT} = 32$ counts) cycle.

This completes the transformation of controller commands to thruster pulses. A summary of this modulator is shown in Table 8.1.

CONTROL MODULATOR (10 Hz)	THRUSTER CONTROL (100 Hz)
u – vector of control commands T_{max} – maximum thruster force N – number of actuators f – look up table (Fig. 8.5)	m – bitwise thruster state variable (mask) c_i – counter for thruster i c_i^{ON} – counts thruster is on c_i^{TOT} – counts for full pulse cycle
<ol style="list-style-type: none"> 1. $u = -Kx$ 2. $u := u/T_{max}$ 3. $u_{max} := \max(u)$ 4. if, $u_{max} > 1.0$, $u := \frac{u}{u_{max}}$ 5. for $i = 1, \dots, N$ <ol style="list-style-type: none"> $c_i^{ON} = f_{ON}[100u(i)]/10$ $c_i^{TOT} = f_{TOT}[100u(i)]/10$ 	<ol style="list-style-type: none"> 1. $m := 0$ 2. increment c_i by 1 3. if $c_i \leq c_i^{ON}$, set bit i to 1 (fire) in m 4. if $c_i > c_i^{TOT}$, $c_i = 0$ 5. Send m to thruster hardware
(a)	(b)

Table 8.1: Thruster Modulation Summary

This table summarizes the details of the PWPF thruster modulation algorithm used for the experiments in this chapter. Thread (a) computes the two integers (c_i^{ON} , and c_i^{TOT}) from the controller commands, and thread (b) turns the thrusters on and off, based on these values and a running counter for each thruster.

8.3 Vibration Suppression

The first closed-loop control experiment illustrates active vibration damping using only GPS measurements for motion information. As in Section 7.3.2, it is convenient to choose certain system motions for study. Fig. 8.6 shows angles of rotation of each of the three rigid sections about the longitudinal twist axis. Consistent with Fig. 6.1, the angles are denoted q_2 , q_5 , and q_8 in the figure. For convenience, these angles will henceforth be referred to as the LT (longitudinal twist) angles.

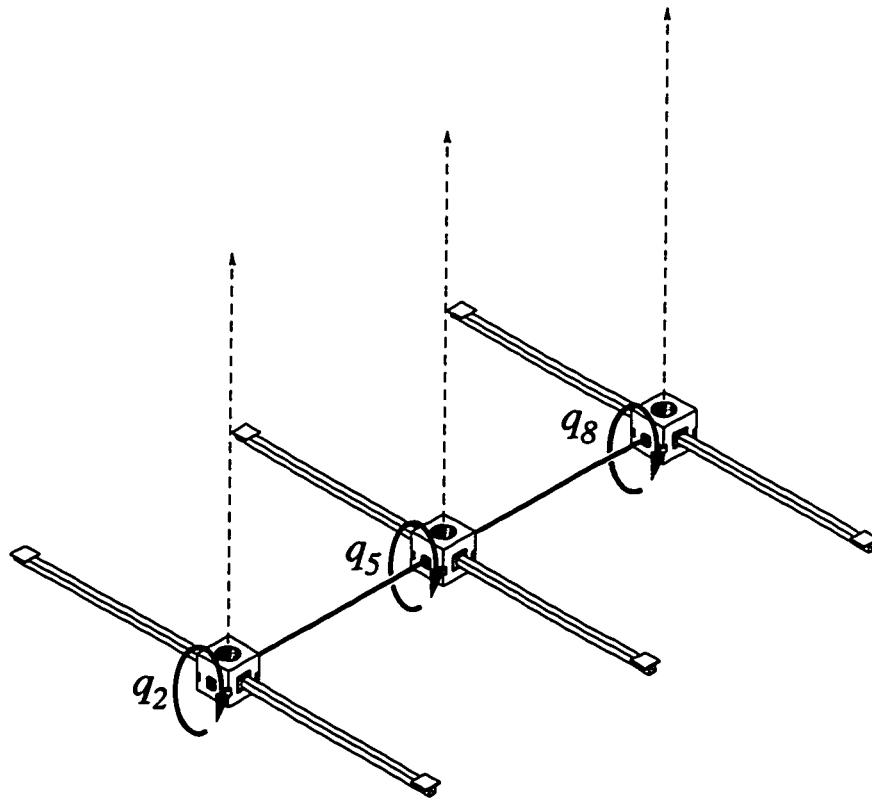


Figure 8.6: Motion Studied for Vibration Control Evaluation

The LT angles are the rotation of the rigid bodies about a longitudinal horizontal axis (indicated with the arrows). These parameters are used to evaluate control performance.

With the control loop open, the structure was perturbed manually such that it vibrated randomly with relative antenna deflections on the order of 10 to 20 centimeters. Due to

the low system damping, vibrations of this type typically persist for 5 to 10 minutes after excitation. Fig. 8.7(A) shows the LT angles for the vibration suppression test, the first 25 seconds of which show the free motion (open-loop). At about 25 seconds, the control loop is closed, and the thrusters begin firing. Vibration damping is achieved with a settling time of approximately 5 seconds, and the LT angles are controlled to within 0.15 degrees as measured by GPS. This performance is consistent with the expected settling times predicted in the simulations of Section 8.1.

As a measure of the open-loop and closed-loop estimator accuracy, Fig. 8.7(B) shows the difference between the GPS and gyroscope-based state estimates. Agreement to better than 1° of rotation angle between the independent sensors is maintained throughout the test. As an additional test of system performance, Fig. 8.7(C) shows two raw integrated gyro measurements. In contrast with the estimator outputs shown in Fig. 8.7(A), Fig. 8.7(C) shows unfiltered structure motion measurements before and after loop closure. This plot verifies the rapid energy damping achieved after loop closure.

8.4 Disturbance Rejection

Response to a Pulse Input

The next test of the GPS based feedback controller is the system response to a pulse disturbance. The open and closed-loop system responses are compared to illustrate the benefit of the active vibration control. For this test, a pulse disturbance was chosen that imparts zero total angular momentum to the entire structure, preventing undesirable large rigid-body horizontal axis rotations for the uncontrolled (open-loop) example. The zero angular momentum pulse chosen was a one second firing of the four thrusters shown in Fig. 8.8. The pulse tends to positively rotate the center section (q_5 increasing) and negatively rotate the end section (q_8 decreasing).

Fig. 8.9 illustrates the open and closed-loop time responses of the LT angles after the pulse was delivered. The pulse was delivered at approximately five (5) seconds on the plot. For the open-loop test, the pulse excited the LT angles to steady harmonic oscillations

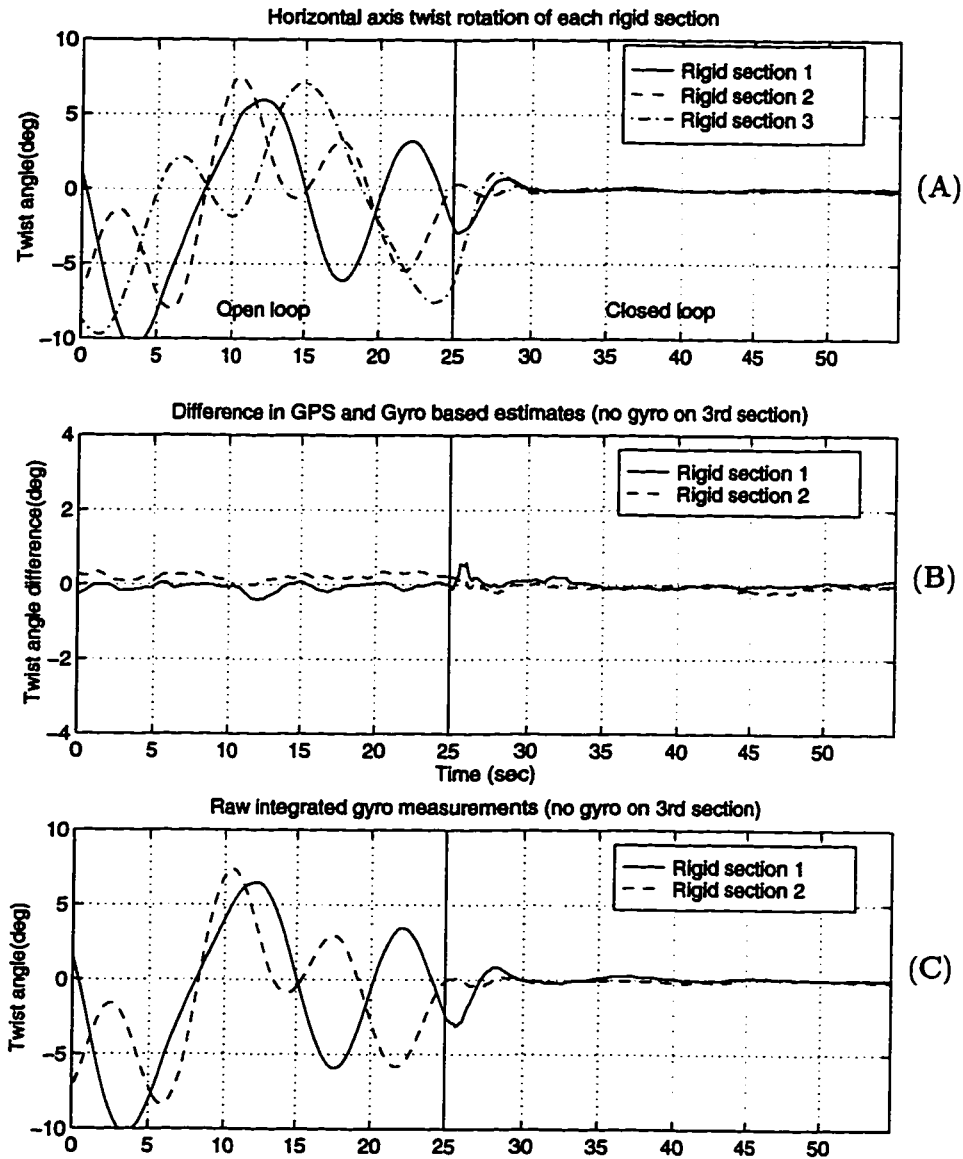


Figure 8.7: Elastic Vibration Control

This figure shows plots during a test of vibration damping using the regulator of Section 8.1. The control loop is closed at approximately 15.5 seconds.

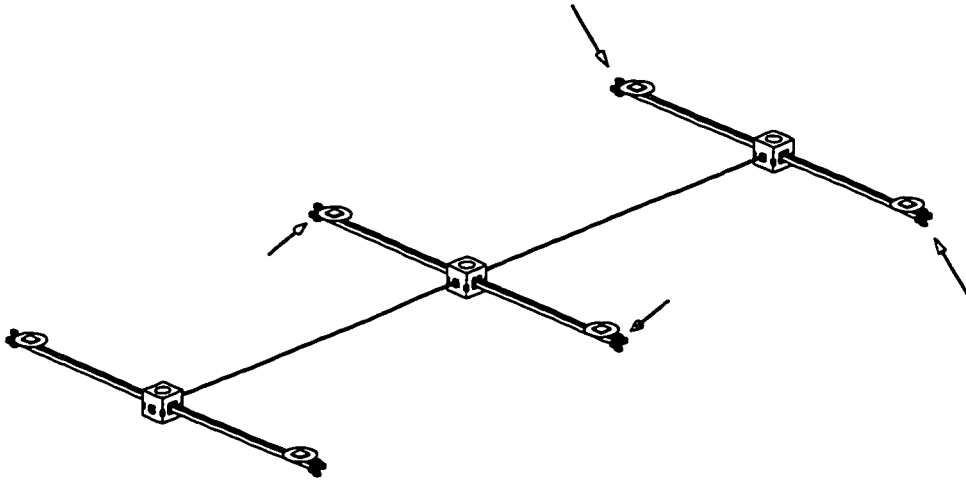


Figure 8.8: Pulse Thrusters

This figure shows the thrusters used to generate a zero angular momentum pulse for the pulse disturbance rejection experiment.

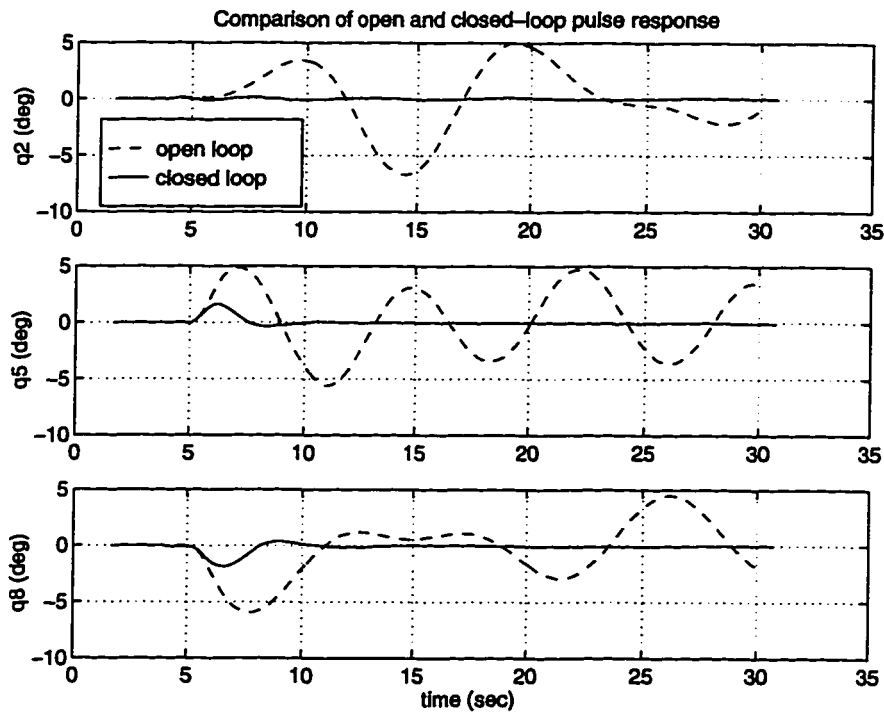


Figure 8.9: Pulse Response

This figure compares the open and closed-loop responses to a one second pulse at the thrusters shown in Fig. 8.8. In closed-loop, the controller settles system motion approximately three seconds after the pulse.

that span approximately 10° in magnitude peak to peak, and the motion persisted with no perceptible damping for the remaining 25 seconds of the test. The plots show that q_5 immediately moved in the positive direction and q_8 in the negative direction after the pulse, as expected given the torques induced by this pulse. While q_5 and q_8 responded immediately, the motion of q_2 lagged by approximately 2 seconds. This is expected because, while the thruster pulse effects q_5 and q_8 directly, q_2 is only affected indirectly through the elastic beam.

When the same pulse was applied to the system with the control loop closed, the system returned to the initial configuration within 3 seconds of the end of the pulse. Again, q_5 and q_8 responded immediately but peaked at one third the magnitude of the first open-loop oscillation peak. Motion of q_2 is not perceptible on the same scale due to the control action. This illustrates a powerful benefit of the full-state MIMO¹ controller design. Deviation of q_2 from 0° is not necessary for regulation of the angle because the controller takes the motion of the entire system into account to compute feedback commands.

Response to a Random Input

The next disturbance rejection test is a comparison of the open and closed-loop output spectra given a random noise input to the system. Like the pulse response test, a zero angular momentum disturbance was chosen for practical reasons. Also, for this test, a zero linear momentum disturbance was chosen so that a total system translational momentum would not build over time. In particular, the four vertically oriented thrusters on section C_1 (illustrated in Fig. 8.10) were pulsed randomly and independently according to 10 Hz random binary sequences. Estimates of q_2 , q_5 , and q_8 , based on the GPS measurements, were computed and stored during open and closed-loop system motion. Fig. 8.11 shows three plots of computed spectra, one for each of the LT angles (q_2 , q_5 , and q_8). The open and closed-loop spectra are shown for each angle for comparison.

The output spectrum of each of the LT angles is greatly reduced by the active controller. q_2 is reduced by approximately 1 order of magnitude, and both q_5 and q_8 are reduced by

¹multiple input, multiple output

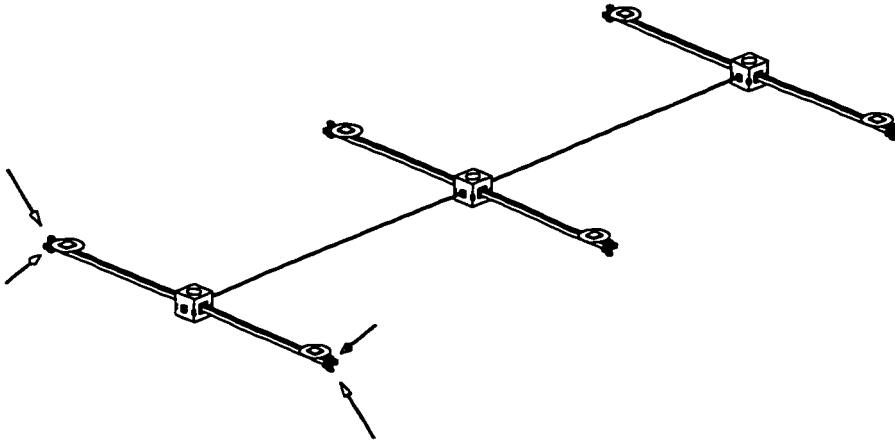


Figure 8.10: Random Noise Thrusters

This figure shows the thrusters used to generate pseudo-random noise for the noise disturbance rejection experiment.

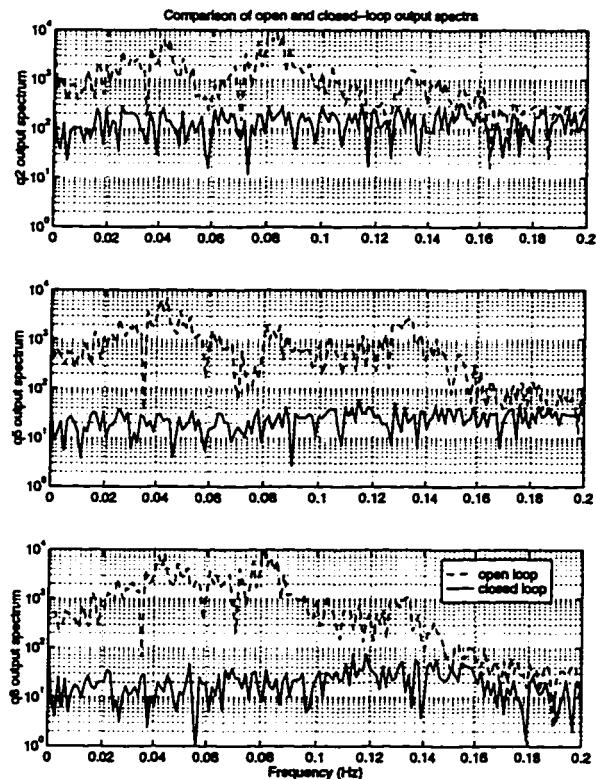


Figure 8.11: Output Spectra

This figure shows the output spectra of the GPS estimates of the LT angles given random pulse disturbance inputs. The closed-loop spectra show better than an order of magnitude of motion suppression over the primary system bandwidth.

approximately 2 orders of magnitude for the 0–0.15 Hz frequency band. Like the pulse respond test, this test shows that the controller is more effective on rigid-sections that are not being excited directly (with thrusters physically on the section).

8.5 Slew Maneuver Control

The next experiment was a test of the feedback system's ability to perform a slew maneuver. In this experiment, the controller attempted to perform a rigid-body rotation of the structure while minimizing internal vibrations that might be excited during the maneuver. This is an ideal test of the overall system performance because it tests ability of:

- the GPS system to sense overall system orientation.
- the controller to successfully execute a large scale platform orientation maneuver.
- the GPS to sense, and the controller to suppress, internal elastic vibrations of the structure during the slew maneuver.

The structure was rotated 16° in the horizontal plane and was left at rest. At time zero, a command for 0° rigid-body was issued to the control system. The controller completed the rotation maneuver within thirty seconds after the control initiation. While the maneuver duration may seem long, it is actually quite fast given the limited thruster force and large rotation inertia associated with this motion. Also, the control time associated with this maneuver is consistent with the performance predicted by the simulations of Section 8.1.

Fig. 8.13 shows the time response plots of the rigid-body rotation angle (see Fig. 8.12). Fig. 8.13(A) is the estimated slew angle, which settles to within a half of a degree as measured by GPS. Fig. 8.13(B) shows the relative vertical axis rotations of each of the rigid sections of the structure (as in Fig. 7.4). These plots indicate the ability of the control system to simultaneously regulate internal vibrations (to within a degree) during a slew maneuver.

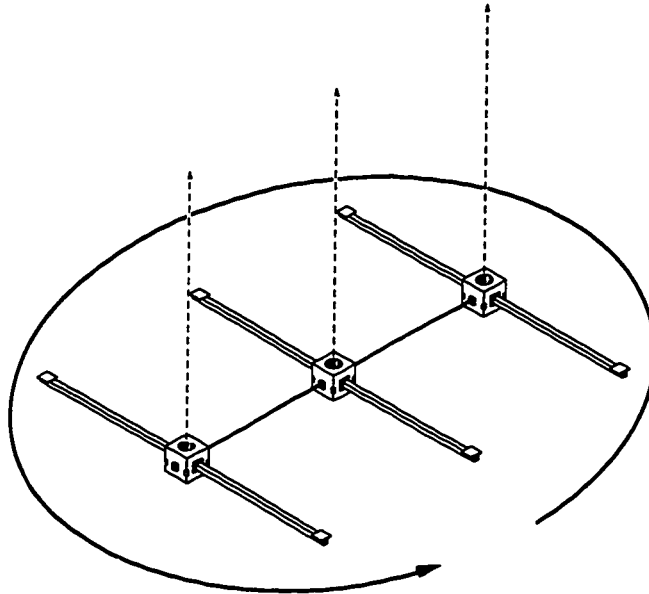


Figure 8.12: Motion Studied for Slew Control Evaluation

The rotation of the entire structure about a lab fixed vertical axis (indicated with the arrow) is plotted in Fig. 8.13

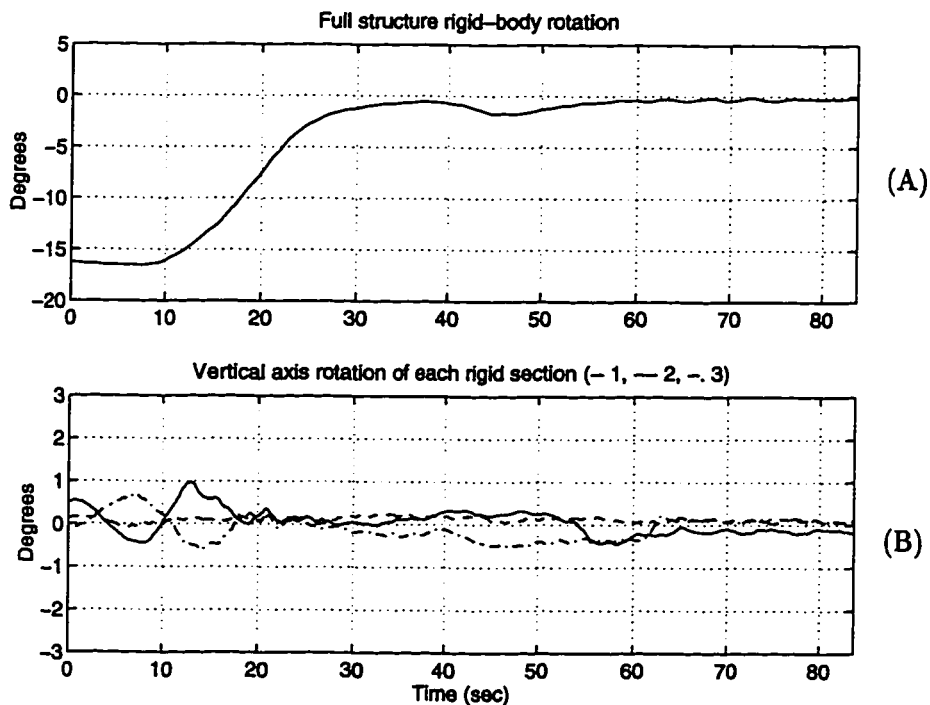


Figure 8.13: Slew Maneuver Control

This figure shows plots during a test of control of a rigid-body slew. The command for 0° rigid-body angle is issued at 9 seconds in the plot.

8.6 Summary

The ultimate goal of this research was to show the use of GPS as a sensor for elastic structure vibration and orientation control. This chapter presents the details of the controller design and describes the pulse modulator algorithm used.

A constant gain controller based on a simple linear dynamic model was able to control both structural orientation and elastic vibrations simultaneously using pulsed thrusters for actuation. Tests show vibration settling times on the order of 5 seconds to sub-degree positioning accuracy. Experiments presented in this chapter also demonstrate the ability of the GPS based controller to reject a pulse disturbance in 3 seconds and to reduce vibration magnitudes due to random excitation by 1 to 2 orders of magnitude. The same controller was used to perform a 30 second, 16° rigid-body orientation slew maneuver.

The results shown in this chapter demonstrate the use of GPS for control of a system with complicated dynamics depending on many parameters (the experiments use 36 measurements and 18 states). This represents a next step in sophistication of distributed antenna GPS sensing systems.

CHAPTER 9

Conclusions

The Global Positioning System now can provide all the information needed to estimate the orientation and deformation of a flexible space platform. In general, the information in the GPS carrier can be used for any structure having motions in the sensitivity and bandwidth of GPS sensors. In previous applications of GPS differential carrier phase, the primary technical challenge has been cycle (or bias) ambiguity resolution. The kinematic cycle resolution algorithms developed for such applications fail with the addition of significant platform flexibility. This work directly addresses the problem of cycle resolution on platforms with relative antenna motions due to flexibility that are on the same order of magnitude as those due to overall platform attitude changes.

Algorithms for sensor initialization and real-time measurement processing were developed and demonstrated with laboratory experiments. For these experiments, an eight meter long, 180 kilogram test structure was built that emulates the low frequency, low damping motion characteristic of large flexible orbiting platforms. A GPS signal environment was recreated for these indoor experiments using six custom built pseudolite transmitters mounted on the walls and ceiling of the laboratory. Results of the experiments shown in this dissertation demonstrate simultaneous vibration and rigid-body orientation control of the test structure at sub-centimeter, sub-degree accuracies.

9.1 Summary of Results and Contributions

The focus of this research has been the development of a distributed antenna GPS sensing system for flexible structure orientation and deformation sensing and control. Toward this goal, contributions have been made in the following specific areas:

9.1.1 Generalized Flexibility Sensing

This work shows the first demonstration of general structural flexibility sensing and control using only GPS measurements. “General” specifies systems with large flexibility and many modes of vibration. This research is an extension of previous work on attitude determination of aircraft that included one wing flex state [Cohen, 1992]. A large flexible space platform was the prototype application of this new technology. However, there are also many potential terrestrial applications, such as suspension bridges, skyscrapers, oil rigs, radio towers, etc. The GPS sensor could provide valuable information for non-destructive evaluation of structural integrity and, in the presence of actuators, for real-time control.

9.1.2 Bias (Cycle) Ambiguity Resolution with Flexibility

Previous researchers have shown kinematic algorithms for finding bias ambiguities using data collected during platform motion, assuming fixed transmitters. Unfortunately, platform flexibility belongs to a class of motion that is not observable using these kinematic techniques. Hence, flexibility was ignored or assumed constant during the bias initialization process previous to this work. This dissertation presents the development and verification of an algorithm that resolves DCP bias ambiguities, taking platform flexibility into account. The new technique combines measurements taken during structural motion with a platform structural dynamic model.

9.1.3 Algorithms for Real-Time State Estimation

Measurement processing algorithms were developed for real-time estimation of the rigid-body and deformation states of the experimental structure. These algorithms were written

with an emphasis on flexibility and generality so the code could be transferred easily to outdoor and space applications. The recursive filtering is based on the Extended Kalman Filter non-linear estimator.

In laboratory tests, the GPS sensor showed 0.3° RMS angular measurement accuracies, as compared to onboard rate gyroscopes. Also, static testing verified that the GPS sensor provides drift free estimates, an advantage over inertial sensors. Applications using larger antenna separations can expect even better performance. This performance exceeds the requirements for achievable large scale pointing control and vibration suppression on the Space Station.

9.1.4 Real-Time Control Demonstration

Real-time control experiments were performed that show simultaneous estimation and control of deformation and orientation states of a flexible platform. State estimates from the real-time estimator (using GPS carrier phase measurements only) were fed into a linear quadratic regulator (LQR) based controller. An array of 24 on/off cold gas thrusters were used for control actuation. Closed-loop control accuracies were simultaneously demonstrated at the sub-centimeter and sub-degree levels for translation and rotation respectively.

The control design culminated in an experiment that tested the ability of the system to perform a rigid-body slew maneuver with simultaneous internal vibration suppression. The controller was able to rotate the entire structure from one static configuration, through 35° of attitude, to another static configuration in about 30 seconds, while maintaining internal deformations to the sub-degree level throughout the maneuver. To the human observer of this test, the entire structure appeared to the eye to be rigid, despite its large open-loop flexibility.

9.1.5 Space Platform Ground Test

In addition to the GPS sensing results shown in this dissertation, a novel, low-cost environment for ground-based testing of space platform structural vibration sensing and control was developed. While the experimental structure was not intended to model an actual space

platform exactly, the system exhibits the required frequencies and translation magnitudes for flexibility sensing studies in three dimensions.

9.2 Suggestions for Further Work

The following are areas of suggested further research:

1. *Recursive dynamic bias estimator:*

While the dynamic bias estimator in Chapter 3 reliably computes optimal bias estimates, the batch formulation is not the most efficient approach available. In practice, the time required to perform the batch solution can become excessive as the number of states variables describing the system grows. Recursive techniques exist that will converge to the same solution much faster and require less storage. One such technique is the non-linear iterated information smoother [Bryson and Ho, 1975; Idan, 1990]. As described in [Pervan, 1996], the process noise weighting corresponding to bias states can be set to zero in the filter, reflecting their constancy in time. Due the non-linearity of the measurement equations, convergence of this recursive estimator depends highly on the accuracy of the initial state trajectory guess. Thus, techniques of accurately guessing the initial state could be crucial to the success of this method.

2. *Line bias calibration:*

Eq. 2.4 shows that the DCP bias is a combination of an integer component and a fractional component. Usually, the fractional component (known as the *line bias*) is a function only of the hardware setup. If a line bias calibration is performed for a particular hardware setup, subsequent bias estimates with the line bias removed should be integer values. The proximity of the bias estimates to integers can be an important integrity check. Also, bias estimates can be rounded to the nearest integer if desired.

Because this thesis concentrates on the mathematics of the dynamic bias estimator, line biases were not calibrated for the experimental work here. However, such a

calibration could be an important part of a real, operational system.

3. *Measurement loss and acquisition:*

GPS signals received in the lab environment with fixed pseudolites are not routinely lost and re-acquired by the receiver. But, in reality, GPS satellites constantly rise and set, and antennas may be routinely rotated toward and away from signals. Thus, it is important for software algorithms to handle the loss and re-acquisition of signals effectively and seamlessly. Particularly important is the reliable identification of the cycle ambiguity of a new measurement using the redundancy of current measurements.

4. *System Identification:*

Given the distributed nature of DCP structural sensing, carrier measurements contain a wealth of information about many of the modes present in an elastic structure. This makes such measurements valuable for on-line system identification. Since both the dynamic bias estimator and the recursive estimator depend on a model of platform dynamics, the overall system could benefit from model accuracy improvements from measurements. The application of the latest system identification algorithms to distributed GPS would be an interesting and valuable area for future research.

9.3 General Distributed Antenna GPS Carrier Sensing

This thesis shows the use of a distributed array of antennas measuring the GPS carrier to estimate several states of the system on which the antennas are mounted. Looking into the future a bit, it is possible to see some powerful motivations for extending this technology to even more antennas and to a more general architecture. For example, the Space Station could use the centimeter relative ranging information in the GPS carrier for a wide range of different (but perhaps inter-related) tasks. Some examples include:

- Manipulator arm endpoint position and orientation
- Free flying robot and/or astronaut guidance and navigation
- Photovoltaic solar array elastic vibration and pointing control
- Overall space platform elastic deformation sensing and control
- On orbit model identification of many sub-systems

Some practical and technical details would need to be studied for these tasks, but none are out of reach given some modest extensions to the type of sensor shown in this work.

9.4 Closing

The presence of GPS signals that contain centimeter level position information, that are present around the globe and in space, and that are available to all users who can track the signal, is having a revolutionary effect on the engineering world. This thesis describes but one of the new applications for this information. To some, it is surprising that centimeter level structural vibration control is possible using information from satellites that are 20,000 kilometers away. But, with the rapid expansion of applications technology over recent years, and with more GPS-like satellites with better ranging information on the horizon, this is still the beginning.

APPENDICES

APPENDIX A

General Carrier Phase Analysis

The phase of a carrier wave, in radians, at the phase center of a reception antenna may be written as follows¹,

$$\phi_{ant} = \omega t + \phi_o + \frac{2\pi}{\lambda}d + \phi_{med} + \phi_{pat} + \phi_{pol} + \frac{1}{2}\nu \quad (\text{A.1})$$

where,

- ω, λ - frequency and wavelength of incoming wave
- ϕ_o - phase at the transmitter at $t = 0$
- d - radial distance from the antenna to the transmitter
- ϕ_{med} - phase component due to distortion and delay in the propagation medium
- ϕ_{pat} - phase component due to reception antenna phase pattern
- ϕ_{pol} - phase component due to signal phase polarization
- ν - random noise

Fig. A.1 is a diagram of a single phase measurement “channel”. ϕ_{med} is the variation in phase due to the sum total of effects of a non-ideal (non-free space) medium in which the wave travels. For example, for terrestrial users, the earth’s ionosphere and troposphere distort and delay the signal significantly. ϕ_{pat} is the phase component due to a non-ideal receiving antenna (i.e. one that does not have a point located phase center — essentially all real antennas). ϕ_{pol} is the component due to the polarization of the incoming signal, and

¹The scaling of ν by 1/2 in Eq. A.1 is only for later notational convenience.

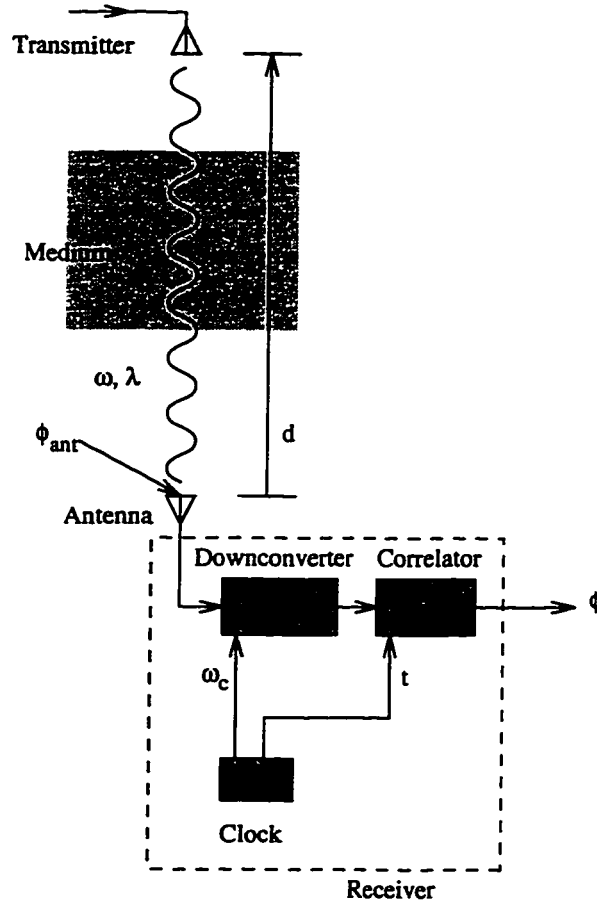


Figure A.1: General Phase Reception Diagram

the orientation of the receive antenna. For example, the measured phase at a patch antenna receiving the right-hand circularly polarized GPS carrier can change as the receive antenna is rotated in any direction about its phase center. This phase component is a function of the angle of incidence of the incoming wave as measured in the antenna frame (azimuth and elevation).

The actual phase measured by the receiver contains a few more important terms such that the overall observable phase, ϕ , is,

$$\phi = \phi_{ant} - \omega_c t + 2\pi N + \phi_{line} \quad (\text{A.2})$$

where,

ω_c - receiver clock downconverter frequency

N - integer ambiguity

ϕ_{line} - line bias

Typical receivers downconvert the incoming signal before correlation (tracking) to an intermediate frequency, introducing $-\omega_c t$ to the measured phase. N represents the integer number of carrier cycles between the transmitting antenna and the receiving antenna at the time of signal acquisition. This is a constant as long as the receiver maintains lock on the signal. So-called “cycle slips” are changes in the value of N after acquisition that are usually attributable to SNR (signal to noise) levels that are near the threshold of that required for tracking or temporarily below the threshold. Finally, ϕ_{line} is the component of phase added to the wave during the signal’s travel from the antenna phase center to the “point of correlation” in the receiver. This is mostly a function of antenna cable length and should be constant for a particular hardware configuration (hence its usual designation as the “line bias”). However, sometimes temperature changes in the hardware can cause drifts in ϕ_{line} .

The total measured phase is now,

$$\phi_{(A.1,A.2)} = (\omega - \omega_c)t + \phi_o + \frac{2\pi}{\lambda}d + \phi_{med} + \phi_{pat} + \phi_{pol} + \phi_{line} + 2\pi N + \frac{1}{2}\nu \quad (A.3)$$

While it is possible to use this GPS carrier observable, ϕ , for (satellite to antenna) range information, d , errors associated with the satellite and its transmission path (satellite clock errors, satellite ephemeris error, ϕ_{med}) degrade the ability to determine antenna position far beyond the fundamental precision of a carrier tracking loop (which is about 3% of the carrier wavelength, or 5mm for the GPS L1 carrier). However, it is possible to retain the high precision capability of carrier tracking by measuring the relative range between antennas. Relative range may be sufficient for a particular application, or, if the absolute position of one antenna is known, then the absolute position of the other antenna may be derived from the relative solution. By subtracting the carrier phase from a single signal source (satellite) at two antennas, errors that are common to both antennas, such as satellite clock

and ephemeris, and ϕ_{med} and ϕ_o are removed.² However, another uncertainty is introduced because of the offset between clocks for each antenna/receiver.

Let subscripts indicate a particular antenna/receiver unit, and let

$$\Delta(\cdot) = (\cdot)_2 - (\cdot)_1. \quad (A.4)$$

If we assume perfect phase lock in both receivers, and ω, λ the same for each antenna, with t_i the time of phase measurement for antenna i ,

$$\Delta\phi_{(A.3, A.4)} = [(\omega - \omega_{c2})t_2 - (\omega - \omega_{c1})t_1] + \frac{2\pi}{\lambda}\Delta d + \Delta\phi_{pat} + \Delta\phi_{pol} + \Delta\phi_{line} + 2\pi\Delta N + \nu \quad (A.5)$$

The noise term ν is assumed to be uncorrelated between antennas and to be of equal magnitude. Thus, differencing doubles the effective noise magnitude. Neglecting second order terms, and letting $t_1 = t$ and $\omega_{c1} = \omega_c$,

$$\Delta\phi_{(A.5)} = [(\omega - \omega_c)\Delta t - \Delta\omega_c t] + \frac{2\pi}{\lambda}\Delta d + \Delta\phi_{pat} + \Delta\phi_{pol} + \Delta\phi_{line} + 2\pi\Delta N + \nu \quad (A.6)$$

The term in brackets is the contribution to the phase that is due to differences in timing between antenna measurements. To use the phase measurement for relative ranging, this term must be eliminated. There are two main methods that have been used to eliminate these timing errors, the common clock and double differencing methods.

Common clock reference

Some architectures provide a single clock signal for processing each antenna measurement. If the clock provides sufficient synchronicity between antennas, Δt and $\Delta\omega_c$ in Eq. A.6 can be negligible. One such architecture is the antenna multiplexing receiver design, for example [Cohen, 1992]. In this case, Eq. A.6 reduces to

$$\Delta\phi_{(A.6)} = \frac{2\pi}{\lambda}\Delta d + \Delta\phi_{pat} + \Delta\phi_{pol} + \Delta\phi_{line} + 2\pi\Delta N + \nu \quad (A.7)$$

²The extent to which the errors are eliminated are a function of the separation distance between antennas.

However, if the antennas need to be separated spatially, it may be very difficult to provide the common clock signal with sufficient precision to make the timing errors negligible.

Double differencing

Signals from two satellites can be visible simultaneously at two antennas that are spatially separated and connected to independent receivers. If the receivers have multiple signal tracking channels that are locally synchronized (which is almost always the case), then Δt and $\Delta\omega_c$ are the same for simultaneous satellite measurements. Moreover, $\Delta\phi_{line}$ should be the same also. Applying a second difference between satellite signals, we obtain

$$\Delta^2\phi \stackrel{(A.6)}{=} \frac{2\pi}{\lambda}\Delta^2d + \Delta^2\phi_{pat} + \Delta^2\phi_{pol} + 2\pi\Delta^2N + 2\nu \quad (A.8)$$

where Δ^2 denotes the (satellite) difference of (antenna) differences. This method always requires two common satellites in view of each antenna pair and increases measurement noise.

Still, relative ranging using carrier phase measurements requires resolution of the integer ambiguity, N . Techniques for ambiguity resolution exist, and some examples are explained in detail in Chapter 3.

It may be important to resolve the phase term due to antenna phase patterns, ϕ_{pat} . These terms are extremely dependent on antenna design and manufacturer and can contribute as much as 30° to the measured phase [Schulper *et al.*, 1994]. However, if the antennas used are identical and a signal arrives at almost the same azimuth and elevation at each antenna, ϕ_{pat} may be negligible. Finally, the phase polarization effect, ϕ_{pol} , may be important for some applications. For further discussion of this topic, see [Lawrence *et al.*, 1995; Lightsey and Parkinson, 1996].

APPENDIX B

Kinematic Estimator Observability Proof

Theorem: Given,

$$\tilde{H} = \left[\begin{array}{ccc|c} H^{(1)} & & 0 & I \\ & H^{(2)} & & I \\ & & \ddots & \vdots \\ 0 & & & H^{(N)} \\ & & & I \end{array} \right] \quad (\text{B.1})$$

\tilde{H} is not full column rank if any column of $H^{(i)}$ is constant for all i .

Proof: \tilde{H} is not full column rank if all its columns are not linearly independent [Kailath, 1980], equivalently, if we can find any $\tilde{v} \neq 0$ such that

$$\tilde{H}\tilde{v} = 0 \quad (\text{B.2})$$

Let $h_k^{(i)}$ equal the k^{th} column of $H^{(i)}$. Define v_k as a vector whose length equals the number of columns of $H^{(i)}$ and whose elements are all zero except for the k^{th} element, which is 1.

$$v_k = \begin{bmatrix} 0 \\ \vdots \\ 1 \\ \vdots \\ 0 \end{bmatrix} \leftarrow k_{th} \text{ element} \quad (\text{B.3})$$

Suppose,

$$\tilde{v} = \begin{bmatrix} v_k \\ v_k \\ \vdots \\ v_k \\ v_I \end{bmatrix} \quad (\text{B.4})$$

with v_I arbitrary. Then,

$$\begin{aligned} \tilde{H}\tilde{v} &= \begin{bmatrix} H^{(1)}v_k + v_I \\ H^{(2)}v_k + v_I \\ \vdots \\ H^{(N)}v_k + v_I \end{bmatrix} \\ &= \begin{bmatrix} h_k^{(1)} + v_I \\ h_k^{(2)} + v_I \\ \vdots \\ h_k^{(N)} + v_I \end{bmatrix} \end{aligned} \quad (\text{B.5})$$

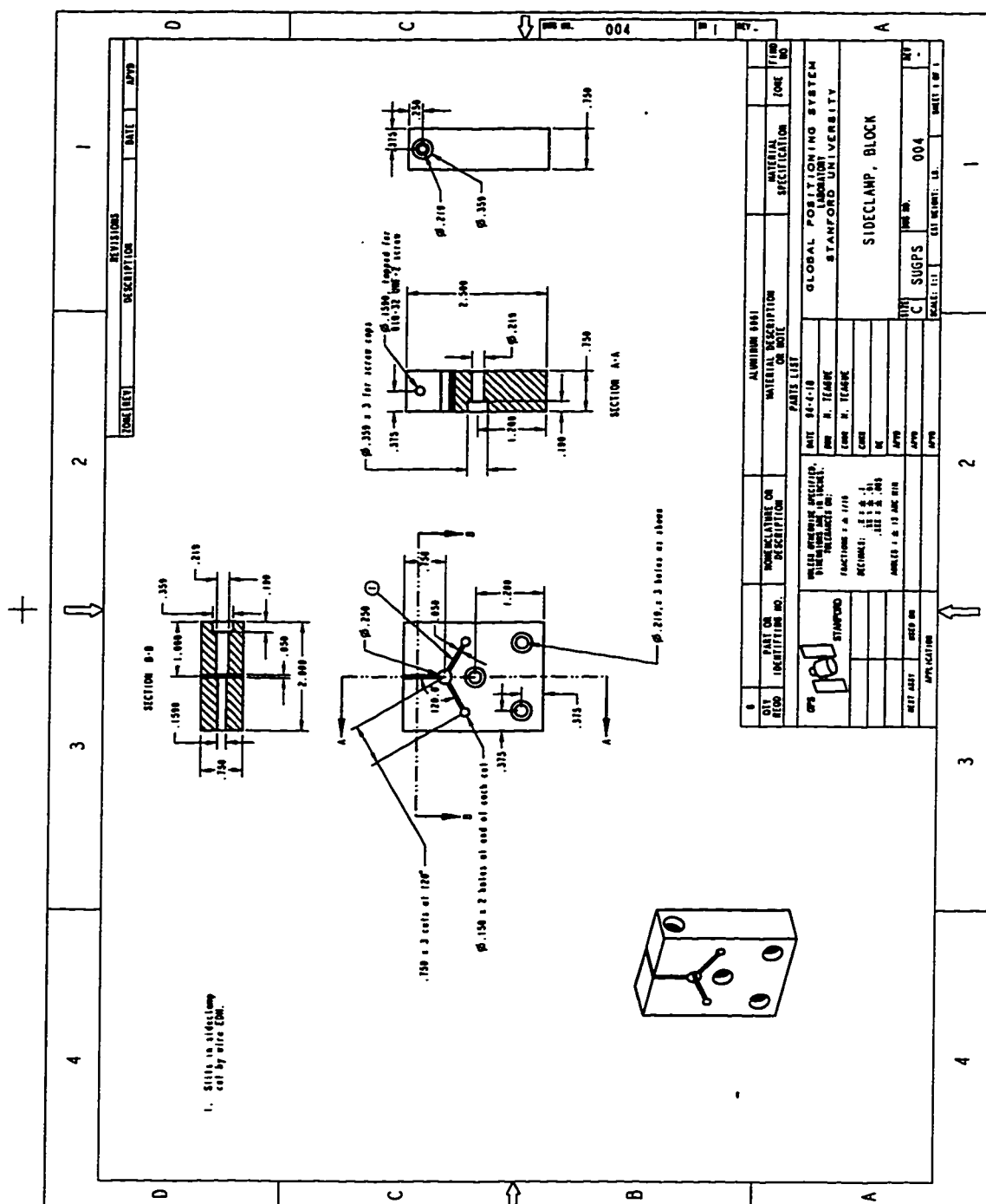
Thus, if $h_k^{(i)}$ is constant for all i , we can set the arbitrary $v_I = -h_k^{(i)}$, and then

$$\tilde{H}\tilde{v} = 0$$

DONE.

APPENDIX C

CAD Drawings



NO MACHINING REQUIRED

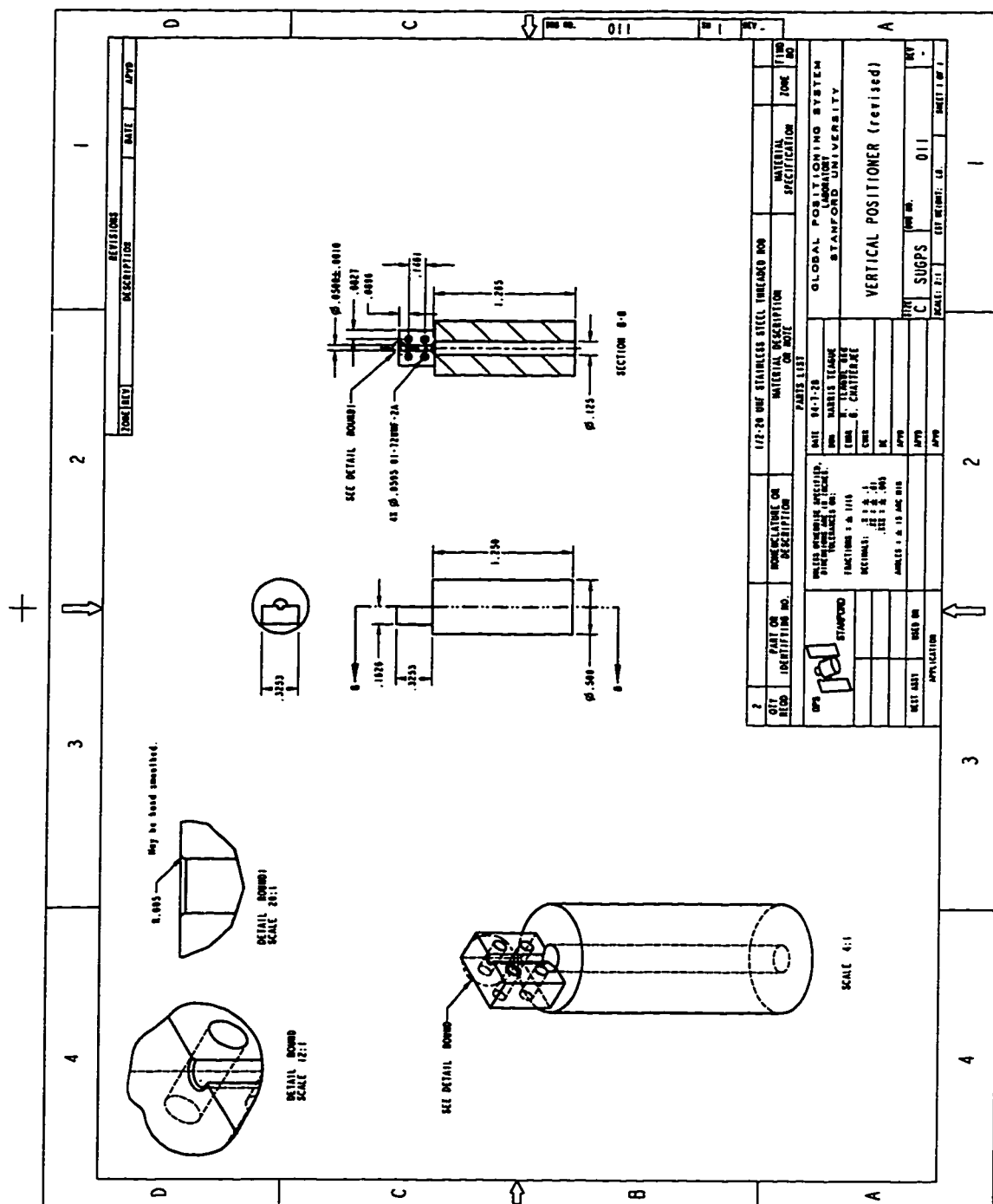
SECTION A-A

SECTION B-B

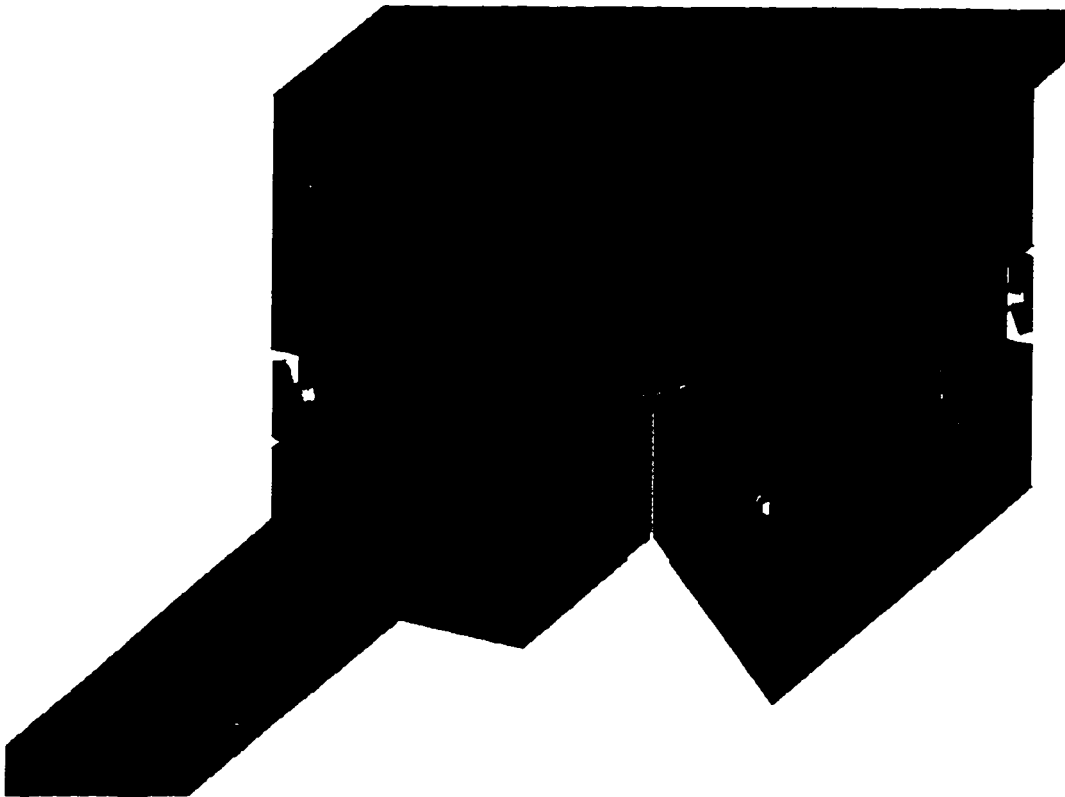
DETAIL VIEW

Dimensions:

- Top View (SECTION A-A):
 - Overall Diameter: $\phi 1.500$
 - Inner Hole Diameter: $\phi .313$
 - Outer Hole Diameter: $\phi .313$
 - Inner Hole Depth: $.120$
 - Outer Hole Depth: $.180$
 - Overall Height: $.250$
- Side View (SECTION B-B):
 - Overall Width: $\phi 1.500$
 - Inner Hole Diameter: $\phi .313$
 - Outer Hole Diameter: $\phi .313$
 - Inner Hole Depth: $.120$
 - Outer Hole Depth: $.180$
 - Overall Height: $.250$



[illegible]



This figure shows a three dimensional shaded rendering of one of the block elements. A section is cut away to show the balance mechanism.

APPENDIX D

MSC/NASTRAN Input File

```
$ Normal Modes Analysis
$ 3/9/96
SOL 106
TIME 10
CEND
TITLE = SAMPLE NASTRAN MODAL ANALYSIS
SUBTITLE = TEAGUE ANALYSIS MODEL 1
LABEL = WITH SUSPENSION SYSTEM
ECHO = UNSORT
$
METHOD = 1
nlparm=99
SPC = 1
DISP = ALL
load = 1
$
OUTPUT(PLOT)
$ USE THE FOLLOWING TO PLOT ON 10.5" X 7.5" AREA
$ (THE PLOT WILL AUTOMATICALLY ROTATE TO USE THE PAPER)
PAPER SIZE 28.571 X 21.429
SET 1 = ALL
VIEW 50.,30.,0.
FIND SCALE,ORIGIN 3,SET 1
PLOT SET 1, ORIGIN 3, LABEL GRID POINTS
FIND SCALE,ORIGIN 4,SET 1
PLOT MODAL DEFORMATION 0,1 thru 20,ORIGIN 4,SET 1,LABEL GRID POINTS
$
BEGIN BULK
param,nmloop,1
param,lgdisp,1
```



```

nlparm,99,1,,iter,1
$
$EIGRL,SID,V1,V2,ND,MSGVLV,MAXSET,SHFSCL,NORM
EIGRL,1,,,20,0,,,MAX
PARAM,COUPMASS,1
PARAM,WTMASS,1.0194-1
$ LATER, TURN OFF NOTICE OF AUTO SPC ACTIONS
$PARAM,PRGPST,NO
PARAM,AUTOSPC,YES
$ TURN ON PATRAN 3 OUTPUT TO UNIT 12
PARAM,POST,-1
PARAM,PATVER,3.0
$
$
$ ***** Grid point definitions *****
GRID      ,      1,      ,      0,      0,      0
GRID      ,      2,      , 0.1270,      0,      0
GRID      ,      3,      , 0.5842,      0,      0
GRID      ,      4,      , 1.0414,      0,      0
GRID      ,      5,      , 1.4986,      0,      0
GRID      ,      6,      , 1.9558,      0,      0
GRID      ,      7,      , 2.4130,      0,      0
GRID      ,      8,      , 2.8702,      0,      0
GRID      ,      9,      , 3.3274,      0,      0
GRID      ,     10,      , 3.7846,      0,      0
GRID      ,     11,      , 3.9116,      0,      0
GRID      ,     12,      , -0.1270,      0,      0
GRID      ,     13,      , -0.5842,      0,      0
GRID      ,     14,      , -1.0414,      0,      0
GRID      ,     15,      , -1.4986,      0,      0
GRID      ,     16,      , -1.9558,      0,      0
GRID      ,     17,      , -2.4130,      0,      0
GRID      ,     18,      , -2.8702,      0,      0
GRID      ,     19,      , -3.3274,      0,      0
GRID      ,     20,      , -3.7846,      0,      0
GRID      ,     21,      , -3.9116,      0,      0
$
GRID      ,    100,      ,      0, 0.1270,      0
GRID      ,    101,      ,      0, 1.8570,      0
GRID      ,    102,      ,      0, -0.1270,      0
GRID      ,    103,      ,      0, -1.8570,      0
GRID      ,    104,      , 3.9116, 0.1270,      0
GRID      ,    105,      , 3.9116, 1.8570,      0

```

```

GRID      ,      106,      ,      3.9116, -0.1270,      0
GRID      ,      107,      ,      3.9116, -1.8570,      0
GRID      ,      108,      ,     -3.9116,  0.1270,      0
GRID      ,      109,      ,     -3.9116,  1.8570,      0
GRID      ,      110,      ,     -3.9116, -0.1270,      0
GRID      ,      111,      ,     -3.9116, -1.8570,      0
$
GRID      ,      200,      ,          0,      0,  0.003
GRID      ,      201,      ,          0,      0, 13.720
GRID      ,      202,      ,      3.9116,      0,  0.003
GRID      ,      203,      ,      3.9116,      0, 13.720
GRID      ,      204,      ,     -3.9116,      0,  0.003
GRID      ,      205,      ,     -3.9116,      0, 13.720
$
GRID      ,      999,      ,    0.2, 0., 1.0 , ,123456
$
$ ***** Finite element definitions *****
RBE2      ,          1,          1, 123456,          2, 12, 100, 102, 200
RBE2      ,          2,          11, 123456,          10, 104, 106, 202
RBE2      ,          3,          21, 123456,          20, 108, 110, 204
CBEAM     ,          4,  1,    100,    101, 999
CBEAM     ,          5,  1,    102,    103, 999
CBEAM     ,          6,  1,    104,    105, 999
CBEAM     ,          7,  1,    106,    107, 999
CBEAM     ,          8,  1,    108,    109, 999
CBEAM     ,         10,  1,    110,    111, 999
PLOTTEL,51,1,2
PLOTTEL,52,1,100
PLOTTEL,53,100,101
PLOTTEL,54,1,102
PLOTTEL,55,1,103
PLOTTEL,56,10,11
PLOTTEL,57,11,104
PLOTTEL,58,104,105
PLOTTEL,59,11,106
PLOTTEL,60,106,107
$
CBEAM     ,      100,          1,          2,          3,          999
CBEAM     ,      101,          1,          3,          4,          999
CBEAM     ,      102,          1,          4,          5,          999
CBEAM     ,      103,          1,          5,          6,          999
CBEAM     ,      104,          1,          6,          7,          999
CBEAM     ,      105,          1,          7,          8,          999

```

```

CBEAM , 106, 1, 8, 9, 999
CBEAM , 107, 1, 9, 10, 999
CBEAM , 108, 1, 12, 13, 999
CBEAM , 109, 1, 13, 14, 999
CBEAM , 110, 1, 14, 15, 999
CBEAM , 111, 1, 15, 16, 999
CBEAM , 112, 1, 16, 17, 999
CBEAM , 113, 1, 17, 18, 999
CBEAM , 114, 1, 18, 19, 999
CBEAM , 115, 1, 19, 20, 999
CONM2, 201, 1,, 60.9, 0.0, 0.0, 0.0,, +con201a
+con201a, 42.500, 0.0, 0.478, 0.0, 0.0, 42.500
CONM2, 202, 11,, 60.9, 0.0, 0.0, 0.0,, +con202a
+con202a, 42.500, 0.0, 0.478, 0.0, 0.0, 42.500
CONM2, 203, 21,, 60.9, 0.0, 0.0, 0.0,, +con203a
+con203a, 42.500, 0.0, 0.478, 0.0, 0.0, 42.500
$suspension threads
CROD,301,2,200,201
CROD,302,2,202,203
CROD,303,2,204,205
param,kdiag,1.0
$
PBEAM , 1, 1,3.5470-5,7.151-10,7.151-10,,1.4302-9
$ for thread pbar, k = EA/L = 1327.8 N/m => A = kL/E (I1, I2, J don't matter)
PROD , 2, 1,2.6358-7
$
MAT1 , 1, 69.10+9, , 0.3333, 2.718+3
$
GRAV , 1, , 9.81, 0.0, 0.0, -1.0
SPC1 , 1, 123456, 201
SPC1 , 1, 123456, 203
SPC1 , 1, 123456, 205
$
$SPC1 , 1, 123456, 1
$FORCE , 1, 11, , 1., 0., 1., 0.
$
ENDDATA

```

APPENDIX E

Transmitter Phase Center Position Survey

A procedure for static estimation of pseudolite transmitter phase centers using carrier signals from the transmitters themselves is as follows. Place one antenna at a reference location M (master antenna) where all signals can be tracked at M . Be prepared to place a second antenna S (slave antenna) at several locations that are known very accurately with respect to the location of M .

Phase measurements can be written:

$$\phi_{ij} = |p_j| - |p_j - q_i| + \beta_j \quad (\text{E.1})$$

$i = 1, \dots, n$ survey point index

$j = 1, \dots, m$ transmitter index

where,

ϕ_{ij} - The differential carrier phase measured from transmitter j with the slave antenna at survey point i

p_j - The position vector from the master antenna to the j th transmitter

q_i - The position vector from the master antenna to the i th slave antenna survey point

β_j - The bias ambiguity associated with the j th transmitter

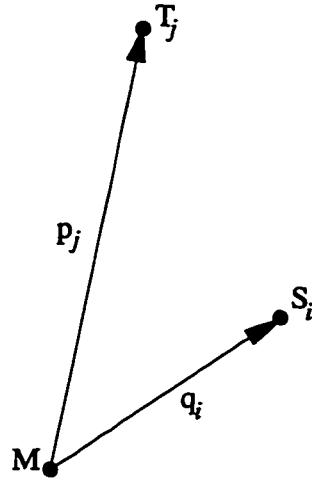


Figure E.1: Simple System Diagram

Define the state vector as:

$$x = \begin{bmatrix} p_1 \\ p_2 \\ \vdots \\ p_m \\ \beta \end{bmatrix} \quad (\text{E.2})$$

where p_j is a 3x1 column vector containing the three Cartesian coordinates of the vector, and :

$$\beta = \begin{bmatrix} \beta_1 \\ \beta_2 \\ \vdots \\ \beta_m \end{bmatrix} \quad (\text{E.3})$$

Take phase measurements at all of the n survey points. The bias is assumed to be a constant for each transmitter during data collection, so care must be taken not to allow any cycle slips during the data collection process. There are mn measurements and $4m$

unknowns in the state vector. To have more measurements than unknowns,

$$mn \geq 4m \quad (\text{E.4})$$

$$n \geq 4 \quad (\text{E.5})$$

However, for the purpose of averaging errors, more survey points is better. Also, the geometric spread of the survey points has a direct impact on the resulting state error covariance.

It is convenient to stack the measurements as follows. Stack the measurements for all survey points for transmitter j as:

$$\phi_j = \begin{bmatrix} \phi_{1j} \\ \vdots \\ \phi_{nj} \end{bmatrix} \quad (\text{E.6})$$

Further, we can stack the transmitter measurements into the final vector containing all measurements as:

$$\Phi = \begin{bmatrix} \phi_1 \\ \vdots \\ \phi_m \end{bmatrix} \quad (\text{E.7})$$

These equations are non-linear and are therefore suitable for solution by gradient search. If the state is written as a nominal value, \hat{x} , plus a perturbation, δx ,

$$x = \hat{x} + \delta x. \quad (\text{E.8})$$

Then, the the measurement can be written

$$\Phi(x) \cong \Phi(\hat{x}) + H(\hat{x})\delta x \quad (\text{E.9})$$

with

$$H(\hat{x}) = \left. \frac{\partial \Phi}{\partial x} \right|_{x=\hat{x}} \quad (\text{E.10})$$

The solution may be found (pending convergence) by iterating the equation

$$\delta x = (H^T W H)^{-1} H^T W [\Phi - \Phi(\hat{x})] \quad (\text{E.11})$$

to convergence. W is a diagonal weighting matrix. A good choice of weights is the corresponding signal-to-noise ratios for each measurement.

H must be updated each iteration to reflect the new state estimate.

$$\frac{\partial \Phi}{\partial x} = \begin{bmatrix} \frac{\partial \Phi}{\partial p_1} & \cdots & \frac{\partial \Phi}{\partial p_m} & \frac{\partial \Phi}{\partial \beta} \end{bmatrix} \quad (\text{E.12})$$

$$= \begin{bmatrix} \frac{\partial \phi_1}{\partial p_1} & 0 & \cdots & 0 & \frac{\partial \phi_1}{\partial \beta} \\ 0 & \frac{\partial \phi_2}{\partial p_2} & & 0 & \frac{\partial \phi_2}{\partial \beta} \\ \vdots & & \ddots & \vdots & \vdots \\ 0 & 0 & \cdots & \frac{\partial \phi_m}{\partial p_m} & \frac{\partial \phi_m}{\partial \beta} \end{bmatrix} \quad (\text{E.13})$$

where,

$$\frac{\partial \phi_j}{\partial p_j} = \begin{bmatrix} \frac{p_j^T}{|p_j|} - \frac{p_j^T - q_1^T}{|p_j - q_1|} \\ \frac{p_j^T}{|p_j|} - \frac{p_j^T - q_2^T}{|p_j - q_2|} \\ \vdots \\ \frac{p_j^T}{|p_j|} - \frac{p_j^T - q_n^T}{|p_j - q_n|} \end{bmatrix} \quad (\text{E.14})$$

using the vector differential property,

$$\frac{\partial |v|}{\partial v} = \frac{v^T}{|v|}. \quad (\text{E.15})$$

Bibliography

- [Anderle, 1979] Anderle, R. J. (1979). Accuracy of Geodetic Solutions Based on Doppler Measurements of the Navstar Global Positioning System Satellites. *Bulletin Géodésique*, 53(2):109—116.
- [Bauer, 1996] Bauer, F. (1996). Space-Based GPS 1996 Mission Overview. In *Proceedings of the Institute of Navigation GPS-96 Conference*, Kansas City MO.
- [Bossler *et al.*, 1980] Bossler, J. D., Goad, B. C., and Bender, P. L. (1980). Using the Global Positioning System (GPS) for Geodetic Positioning. *Bulletin Géodésique*, 54(4):553—563.
- [Bryson and Ho, 1975] Bryson, A. and Ho, Y.-C. (1975). *Applied Optimal Control*. Hemisphere Publishing Corporation.
- [Bryson, 1993] Bryson, A. E. (1993). Class Notes, Optimal Estimation with Uncertainty. Stanford University.
- [Carlson, 1986] Carlson, A. B. (1986). *Communication Systems*. McGraw-Hill.
- [Cobb *et al.*, 1994] Cobb, H. S., Cohen, C. E., and Parkinson, B. W. (1994). Theory and Design of Pseudolites. In *Proceedings of the Institute of Navigation, National Technical Meeting*, San Diego CA.
- [Cohen, 1992] Cohen, C. E. (1992). *Attitude Determination Using GPS*. PhD thesis, Stanford University, Department of Aeronautics and Astronautics, Stanford, CA 94305.
- [Cohen, 1996] Cohen, C. E. (1996). *Global Positioning System: Theory and Applications*, volume 164 of *Progress in Astronautics and Aeronautics*, chapter Attitude Determination, pages 519—538. American Institute of Aeronautics and Astronautics.
- [Cohen *et al.*, 1995] Cohen, C. E., Cobb, H. S., Lawrence, D. G., Pervan, B. S., Powell, J. D., Parkinson, B. W., Aubrey, G. J., Loewe, W., Ormiston, D., McNally, B. D., Kaufmann, D. N., Wulschleger, V., and Jr., R. J. S. (1995). Autoland a 737 Using GPS Integrity Beacons. *NAVIGATION: Journal of the Institute of Navigation*, 42(3).
- [Cohen *et al.*, 1993] Cohen, C. E., Lightsey, E. G., Parkinson, B. W., and Feess, W. A. (1993). Space Flight Tests of Attitude Determination Using GPS. In *Proceedings of the Institute of Navigation GPS-93 Conference*, Salt Lake City UT.

- [Cohen *et al.*, 1994a] Cohen, C. E., Lightsey, E. G., Parkinson, B. W., and Feess, W. A. (1994a). Space Flight Tests of Attitude Determination Using GPS. *International Journal of Satellite Communications*, 12:427–433.
- [Cohen *et al.*, 1994b] Cohen, C. E., McNally, B. D., and Parkinson, B. W. (1994b). Flight Tests of Attitude Determination Using GPS Compared Against an Inertial Navigation Unit. *NAVIGATION: Journal of the Institute of Navigation*, 41(1).
- [Cohen and Parkinson, 1992] Cohen, C. E. and Parkinson, B. W. (1992). Aircraft Applications of GPS-based Attitude Determination: Test Flights on a Piper Dakota. In *Proceedings of the Institute of Navigation GPS-92 Conference*, Albuquerque NM.
- [Conway, 1995] Conway, A. R. (1995). *Autonomous Control of a Model Helicopter Using Carrier Phase GPS*. PhD thesis, Stanford University, Department of Electrical Engineering, Stanford, CA 94305.
- [Counselman III and Shapiro, 1979] Counselman III, C. C. and Shapiro, I. I. (1979). Miniature Interferometer Terminals for Earth Surveying. *Bulletin Géodésique*, 53(2):139–163.
- [Dentinger and Cohen, 1993] Dentinger, M. P. and Cohen, C. E. (1993). Differential Phase Measurement through Antenna Multiplexing. U.S. Patent 5268695.
- [Franklin *et al.*, 1990] Franklin, G. F., Powell, J. D., and Workman, M. (1990). *Digital Control of Dynamic Systems*. Series in Electrical and Computer Engineering: Control Engineering. Addison-Wesley, Reading, MA, second edition.
- [Gallmeister, 1995] Gallmeister, B. (1995). *POSIX.4, Programming for the Real World*. O'Reilly and Associates.
- [Gelb, 1974] Gelb, A. (1974). *Applied Optimal Estimation*. MIT Press, Cambridge, MA.
- [Goad, 1985] Goad, C. C., editor (1985). *Proceedings of the First International Symposium on Precise Positioning with GPS Conference*. International Union of Geodesy and Geophysics, International Association of Geodesy, US Department of Defence, US Department of Commerce.
- [Goad and Remondi, 1979] Goad, C. C. and Remondi, B. W. (1979). Initial Relative Positioning Results Using The Global Positioning System. *Bulletin Géodésique*, 58(2):193–210.
- [Greenspan *et al.*, 1982] Greenspan, R. L., Ng, A. Y., Przyjems, J. M., and Veale, J. D. (1982). Accuracy of Relative Positioning by Interferometry with Reconstructed Carrier GPS: Experimental Results. In *3rd International Geodetic Symposium on Satellite Doppler Positioning*, Las Cruces, NM.
- [Hassibi and Boyd, 1995] Hassibi, A. and Boyd, S. (1995). Integer Parameter Estimation in Linear Models with GPS Applications. Technical report, Information Systems Laboratory, Stanford University.

- [Hatch, 1982] Hatch, R. (1982). The Synergism of GPS Code and Carrier Measurements. In *International Geodetic Symposium on Satellite Doppler Positioning*, Las Cruces, NM.
- [Hwang, 1991] Hwang, P. Y. C. (1991). Kinematic GPS for Differential Positioning: Resolving Integers Ambiguities on the Fly. *NAVIGATION: Journal of the Institute of Navigation*, 38(1).
- [Idan, 1990] Idan, M. (1990). *An Identification Algorithm Based on Smoothing*. PhD thesis, Stanford University, Department of Aeronautics and Astronautics, Stanford, CA 94305. Also published as SUDAAR 523.
- [Kailath, 1980] Kailath, T. (1980). *Linear Systems*. Prentice-Hall Information and System Sciences Series. Prentice-Hall, Englewood Cliffs, NJ.
- [Kane and Levinson, 1980] Kane, T. R. and Levinson, D. A. (1980). Large Motions of Unrestrained Space Trusses. *Journal of the Astronautical Sciences*, XXVIII(1):49—88.
- [Kruczynski et al., 1989] Kruczynski, L. R., Li, P. C., Evans, A. G., and Hermann, B. R. (1989). Using GPS to Determine Vehicle Attitude: USS Yortown Test Results. In *Proceedings of the International Technical Meeting of the Satellite Division of the Institute of Navigation*, Colorado Springs, CO.
- [Lawrence et al., 1995] Lawrence, D., Cobb, H. S., Cohen, C., Christie, J., Powell, J. D., and Parkinson, B. (1995). Maintaining GPS Positioning in Steep Turns Using Two Antennas. In *Proceedings of the Institute of Navigation GPS-95 Conference*, Palm Springs CA.
- [Lawrence, 1996] Lawrence, D. G. (1996). *Aircraft Landing Using GPS*. PhD thesis, Stanford University, Department of Aeronautics and Astronautics, Stanford, CA 94305.
- [Lightsey and Parkinson, 1996] Lightsey, E. G. and Parkinson, B. W. (1996). GPS Based Attitude Determination On Nonaligned Antenna Arrays. In *Proceedings of the Institute of Navigation GPS-96*, Kansas City, MO.
- [LynxOS, 1995] LynxOS (1995). *LynxOS 2.4.0 Users Manuals*. Lynx Real-Time Systems, 2239 Samaritan Drive, San Jose, CA 95124.
- [MacDoran, 1979] MacDoran, P. F. (1979). Satellite Emission Radio Interferometric Earth Surveying: SERIES – GPS Geodetic System. *Bulletin Géodésique*, 53(2):117—138.
- [MacDoran et al., 1984] MacDoran, P. F., Miller, R. B., Buennagel, L. A., Fliegel, H. F., and Tanida, L. (1984). Codeless GPS Systems for Positioning of Offshore Platforms and 3D Seismic Surveys. *NAVIGATION: Journal of the Institute of Navigation*, 31(2):57—69.
- [Montgomery et al., 1994] Montgomery, P. Y., Uematsu, H., and Parkinson, B. W. (1994). Analysis of Angular Velocity Determination Using GPS. In *Proceedings of the Institute of Navigation GPS-94 Conference*, Salt Lake City UT.

- [Parkinson and Gilbert, 1983] Parkinson, B. W. and Gilbert, S. W. (1983). NAVSTAR: Global Positioning System – Ten Years Later. *IEEE Journal*, 71(10):1177–1186.
- [Parkinson *et al.*, 1996] Parkinson, B. W., Spilker, J. J., Axelrad, P., and Enge, P. (1996). *GPS: Theory and Applications*. American Institute of Aeronautics and Astronautics, Washington, DC.
- [Pervan, 1996] Pervan, B. S. (1996). *Navigation Integrity for Aircraft Precision Landing Using the Global Positioning System*. PhD thesis, Stanford University, Department of Aeronautics and Astronautics, Stanford, CA 94305.
- [Schulper *et al.*, 1994] Schulper, B. R., Allhouse, R. L., and Clark, T. A. (1994). Signal Characteristics of GPS User Antennas. *NAVIGATION: Journal of the Institute of Navigation*, 41(3):227–295.
- [Teague *et al.*, 1996a] Teague, E. H., How, J. P., Lawson, L. G., Boerjes, M., and Parkinson, B. W. (1996a). Techniques for Real-Time Control of Flexible Structures Using GPS. In *Proceedings of the AAS Guidance and Control Conference*, Breckenridge CO.
- [Teague *et al.*, 1995] Teague, E. H., How, J. P., Lawson, L. G., and Parkinson, B. W. (1995). GPS as a Structural Deformation Sensor. In *Proceedings of the AIAA Guidance, Navigation and Control Conference*, Baltimore MD.
- [Teague *et al.*, 1996b] Teague, E. H., How, J. P., and Parkinson, B. W. (1996b). Carrier Differential GPS for Real-Time Control of Large Flexible Structures. In *Proceedings of the Institute of Navigation GPS-96*, Kansas City, MO.
- [Teague and Parkinson, 1993] Teague, E. H. and Parkinson, B. W. (1993). *Translation, Rotation, And Vibration Control of Large Space Structures Using Self-Differential GPS (SDGPS)*, volume 81 of *Guidance and Control*, pages 93–101. American Astronautical Society.
- [Van Graas and Braasch, 1991] Van Graas, F. and Braasch, M. (1991). GPS Interferometric Attitude and Heading Determination: Initial Flight Test Results. *NAVIGATION: Journal of the Institute of Navigation*, 38(4):359–378.
- [Wall and Schwartz, 1991] Wall, L. and Schwartz, R. L. (1991). *Programming PERL*. O'Reilly and Associates.
- [Zimmerman, 1996] Zimmerman, K. R. (1996). *Experiments in the Use of the Global Positioning System for Space Vehicle Rendezvous*. PhD thesis, Stanford University, Stanford, CA 94305.
- [Zimmerman and Cannon Jr., 1995] Zimmerman, K. R. and Cannon Jr., R. H. (1995). Experimental Demonstration of GPS for Rendezvous Between Two Prototype Space Vehicles. In *Proceedings of the Institute of Navigation GPS-95 Conference*, Palm Springs CA.